A Contribution to the Estimation of Kinematic Quantities from Linear Motion Blurred Images

Jimy Alexander Cortés Osorio

Universidad Nacional de Colombia
Manizales, caldas

April ,2020

A Contribution to the Estimation of Kinematic Quantities from Linear Motion Blurred Images

Jimy Alexander Cortés Osorio

Advisors:

PhD Juan Bernardo Gómez Mendoza

PhD Juan Carlos Riaño Rojas

Reseach Group:

Computación Aplicada Suave y Dura SHAC

(Soft and Hard Applied Computing)

Universidad Nacional de Colombia
Manizales, Caldas

April, 2020

Una Contribución a la Estimación de Cantidades Cinemáticas a partir de Imágenes Desenfocadas por Movimiento Lineal

Jimy Alexander Cortés Osorio

Consejeros:

PhD Juan Bernardo Gómez Mendoza

PhD Juan Carlos Riaño Rojas

Grupo de Investigación:

Computación Aplicada Suave y Dura SHAC

(Soft and Hard Applied Computing)

Universidad Nacional de Colombia
Manizales, Caldas

Abril, 2020

Abstract

This thesis introduces a new approach for estimating kinematic quantities, namely the angle the relative speed, and the acceleration from an actual single motion blur image using the Discrete Cosine Transform (DCT). Motion blur is a common phenomenon present in images. It is produced by the relative movement between the camera and the objects in the scene during camera sensor exposure to light. It usually happens to image recording systems mounted in vehicles, hand-held cameras, drones, satellites, and mobile robots. Our software-based technique focuses on cases where the camera moves at a constant linear velocity while the background remains unchanged. Syntactic and actual image were used to carry out the experiments. The Mean Absolute Error (MAE) of DCT Radon method for direction estimation was 4.66° degrees. Additionally, the Mean Relative Error for speed estimation of the DCT Peudo Cepstrum was 5.15%. Our alternative DCT frequency analysis proposals were more accurate than all competitors evaluated for velocity measurement. Also, we proposed an alternative approach to estimate relative acceleration from an actual uniformly accelerated motion blur image using homomorphic mapping to extract the characteristic Point Spread Function of a degraded image to train a machine learning regression model. Ensembles of Trees, Gaussian Processes (GPR), Linear, Support Vector Machine (SVM), Tree Regression and 19 variants were evaluated to predict the acceleration. The bests RMSE result was $0.2547 m/s^2$ using GPR (Matern 5/2) with a prediction Speed of 530 observation per second. Finally, the proposed methods are valid alternatives for the estimation of the velocity and the acceleration from a single linear motion blur image.

keywords:

acceleration, DCT, Kinematic quantities, motion blur, ,velocity, vision-based measurement.

Resumen

Esta tesis presenta un nuevo enfoque para estimar cantidades cinemáticas, a saber, el ángulo de la velocidad relativa y la aceleración de una imagen de desenfoque de movimiento único real usando la Transformación discreta de coseno (DCT). El desenfoque de movimiento es un fenómeno común presente en las imágenes. Se produce por el movimiento relativo entre la cámara y los objetos en la escena durante la exposición del sensor de la cámara a la luz. Suele ocurrir con los sistemas de grabación de imágenes montados en vehículos, cámaras de mano, drones, satélites y robots móviles. Nuestra técnica basada en software se enfoca en casos donde la cámara se mueve a una velocidad lineal constante mientras el fondo permanece sin cambios. Para los experimentos de estimación de velocidad se usaron imágenes sintéticas y reales. El error absoluto medio (MAE) del método DCT Radon para la estimación de dirección fue de 4.66° grados. Además, el error relativo medio para la estimación de la velocidad del DCT Pseudo Cepstrum fue del 5.15%. Las propuestas alternativas de análisis de frecuencia DCT fueron más precisas que todos los competidores evaluados para la medición de velocidad. Además, se propuso un enfoque alternativo para estimar la aceleración relativa a partir de una imagen de desenfoque de movimiento acelerado uniformemente real usando mapeo homomórfico para extraer la función de dispersión de puntos característica de una imagen degradada para luego entrenar un modelo de regresión de aprendizaje automático. Se tomaron un total de 125 imágenes de desenfoque de movimiento uniformemente acelerado en un entorno controlado con luz y distancia a 5 aceleraciones diferentes en un rango entre$0.64 m/s^2$ y$2.4 m/s^2$. Se evaluaron Conjuntos de árboles, procesos gaussianos (GPR), Regresión Lineal, Máquinas de Vectores de Soporte (SVM) y 19 variantes de regresión para predecir la aceleración. El mejor resultado RMSE fue$0.2553 m/s^2$ usando regresión GPR con una velocidad de predicción de 530 observaciones por segundo. Finalmente, se concluye que los métodos propuestos son alternativas válidas para la estimación de la velocidad y la aceleración de una sola imagen con desenfoque de movimiento lineal invariante.

Palabras clave:

aceleración, cantidades cinemáticas, DCT, desenfoque por movimiento, velocidad, medida basada en visión.

Acknowledgement

Especially thanks to my thesis advisors, Ph.D. Juan Bernardo Goméz Mendoza, and Ph.D. Juan Carlos Riaño Rojas at Universidad Nacional de Colombia in Manizales, who steered me in the right direction whenever they thought I needed, always respecting my work.

Also, I would like to thank my undergraduate and master students, at Universidad Tecnológica de Pereira, for their active support during the development of this research. They, honestly, made this work more pleasant.

The last, but not the less, Universidad Tecnológica de Pereira for its funding support and for allowing me to have sufficient time to carry out this research thesis.

Contents

List of Figures

List of Tables

List of Algorithms

Chapter 1

INTRODUCTION

Vision-based measurement (VBM) systems are starting to become popular as an affordable and a capable alternative for scientific and engineering applications. When cameras are used as instruments, motion blur usually emerges as a recurrent and undesirable image degradation that deteriorates the visual image content which actually contains kinematic information dismissed. Blur is a frequent phenomenon which occurs when the motion is relatively large compared to the camera exposure time. It is frequently present in all images in a greater or lesser amount depending on the imaging system.

Kinematic quantities are relevant in control [Luh et al.(1980)Luh, Walker, and Paul], transportation [Hoberock(1977)], robotics [Lepetič et al.(2003)Lepetič, Klančar, Škrjanc, Matko, and Potočnik], physics [Sironi and Spitkovsky(2011)], sports biomechanics [Ohgi(2002)], geology [Xu et al.(2013)Xu, Liu, and Li], and technical [Sawicki et al.(2003)Sawicki, Wu, Baaklini, and Gyekenyesi] and medical [Hozumi et al.(2000)Hozumi, Yoshida, Akasaka, Asami, Kanzaki, Ueda, Yamamuro, Takagi, and Yoshikawa] diagnostics. Position, velocity, and acceleration are kinematic quantities that are part of the decision-making in motion systems. One of the most classical approaches to estimate the velocity of a moving object is the Optical Flow. Even Though this technique has shown high accuracy for velocity, and acceleration estimation, it is also highly demanding in computer processing requirements and uses a set of images instead of one [Stanisavljevic et al.(2000)Stanisavljevic, Kalafatic, and Ribaric, Barron et al.(1994)Barron, Fleet, and Beauchemin, Bab-Hadiashar and Suter(1998), Ishiyama et al.(2004)Ishiyama, Okatani, and Deguchi, Pinto et al.(2014)Pinto, Moreira, Correia, and Costa].

As an example, one of the critical objectives for autonomous robotics is to carry out tasks in reliable and efficient navigation, which makes that the images captured by mounted cameras on this have an relvant role in the decision making for navigation, detection of objects and the ability to avoid obstacles, among others. Video captured by robots is not exempt from blur caused by the camera or the object shake under observation. This adds an unwanted degradation to the captured images.

Motion blur is characterized by a Point Spread Function (PSF) whose parameters are strongly related to object and camera motion. The simplest case of motion blur is due to spatially invariant linear distribution, which has been extensively studied, while still being fairly complex as shown in [Su et al.(2011)Su, Lu, and Tan, Wu et al.(2012)Wu, Guan, Su, and Zhang, Wu et al.(2011)Wu, Ling, Yu, Li, Mei, and Cheng]. The researchers of these studies, who made object tracking under motion blurred conditions, stated that image degradation causes problems in defining an object to track since movements or sudden changes in position add

great uncertainty in the estimation of the target position. A typically used solution is first to remove the blurred content and then apply tracking, but this consumes computational resources significantly. The works shown in [Wu et al.(2011)Wu, Ling, Yu, Li, Mei, and Cheng, Dai and Wu(2008)] mention that the researchers have managed to track severely blurred targets effectively without removing the blur under the so-called Blur-Driven tracker technique due to blur can provide information on the spatial change of the object to follow.

When a picture is taken under low light conditions, the camera needs a longer exposure time to obtain enough light to cut the image, which produces some blur on the formed picture. Digital camera makers have introduced two types of hardware solutions to mitigate this undesired effect on images. The first approach is to raise the camera sensitivity (ISO - International Organization for standardization - digital still-camera film speed is described in 12232:2006) by amplifying the sensor signal, which allows a faster shutter speed, but unfortunately, this decreases image quality because of a noise occurrence. The last technique is the optical image stabilization (OIS) [Sorel et al.(2009)Sorel, Sroubek, and Flusser, McCloskey et al.(2011)McCloskey, Muldoon, and Venkatesha] which is made with either a moving image sensor or an optical element in order to balance camera motion blur effect. Unfortunately, these solutions are more expensive and increase weight and energy consumption, and dismiss the kinematic information.

Velocity and acceleration estimation from a single blurred image are aims in this research due to the relevance of this topic in science and engineering. This solution for the estimation of kinematic quantities using blur images has been roughly considered in [Yitzhaky and Stern(2003), Yitzhaky et al.(1998)Yitzhaky, Mor, Lantzman, and Kopeika, Pérez Huerta and Rodriguez Zurita(2005), Loce and Wolberg(1995)]. Surveillance systems, engineering solutions, and physics research usually need the estimation of velocity and acceleration; therefore they can benefit from this single image method when other sources are not available.

The proposed solutions introduced in the thesis can help reduce the use of sensors and camera specifications which increase the economic cost significantly and make harder the development of autonomous vision-based systems. This search introduces some computational algorithms to extract kinematic information from usually discarded images. I propose to explore a Non-traditional source of kinematic quantities such as motion blurred degraded images that are implicitly rich in information. These novel approaches allow obtaining the speed and the acceleration of an object in motion from a single linear motion blur in variant and invariant conditions.

1.1 THEORETICAL FRAMEWORK

1.1.1 Characteristics of optical and electro-optical systems

Point Spread Function PSF is the smallest detail that can produce an imaging optical system through its impulse response $h(x, y)$. The PSF describes the spatial distribution of the illumination produced by a point source in the plane of the image when the optical system responses to a Dirac pulse [Fliegel(2004)]. Figure 1.1 shows a simplified diagram with unit amplification:

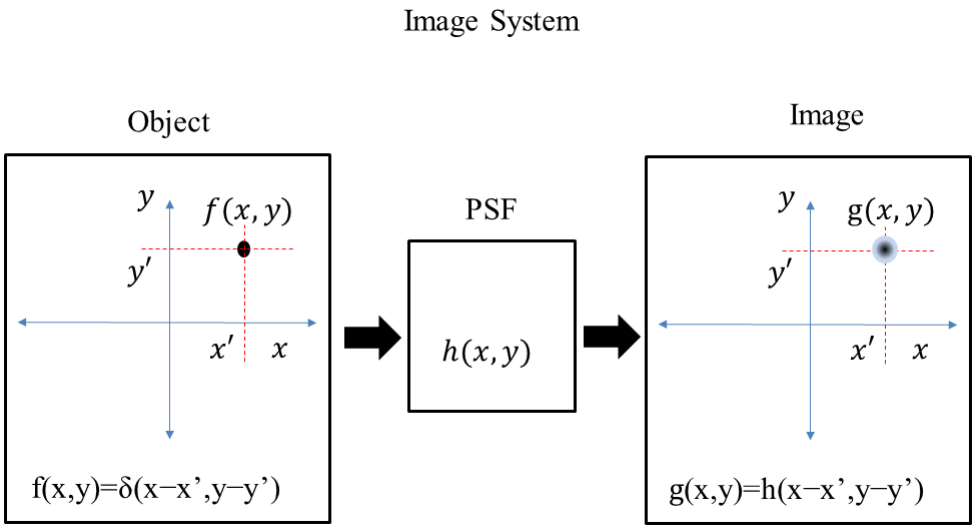

Figure 1.1: Impulse response of a two-dimensional imaging system with its Point Spread Function.

As we can see in Figure 1.1, there is an ideal point source $f(x,y) = \delta(x-x', y-y')$ in the object plane and a phase-shifted impulse response $g(x,y) = h(x-x', y-y')$ in the image plane where the relationship between the object and the image is expressed as shown in Equation 1.1:

$$g(x,y) = f(x,y) * h(x,y) \tag{1.1}$$

The object irradiance distribution $f(x,y)$ is convolved with the impulse response $h(x,y)$ in the Equation 1.1. This can also be represented as a convolution integral as shown in Equation 1.2:

$$g(x,y) = \int\int f(\alpha,\beta)h(x-\alpha, y-\beta)d\alpha d\beta \tag{1.2}$$

From Equation 1.2, we can see that the impulse response of an ideal image system produces a transfer function equals the Delta Dirac $h_{ideal}(x,y) = \delta(x,y)$, which is impossible because of the nature of light in physical systems which brings up some defocus at the edge of the formed image [Fliegel(2004)].

While the product shown in Equation 1.1 is a convolution in the space domain, this same corresponds to a simple multiplication in the frequency domain when the Fourier Transform has been applied to the involved functions as shown in Equation 1.3:

$$G(u,v) = F(u,v)H(u,v) \tag{1.3}$$

$H(u,v)$ is the Optical Fourier Transform (OFT), which is complex in nature; its magnitude and phase are called Modulation Transfer Function (MTF) and Phase Transfer Function (PTF), respectively [Gunturk(2012), Fliegel(2004)].

$$F\{h(x,y)\} = H(u,v) =\mid H(u,v) \mid e^{j\phi(u,v)} \rightarrow OFT$$

$$\mid H(u,v) \mid \rightarrow MTF$$

$$\phi(u, v) \rightarrow PTF$$

1.1.2 Blur Modeling

Blur is the area of an image that can not be precisely distinguished because it has no defined edge due to the little high-frequency content. The relative motion between the camera and the observed scene, an optical system out of focus in its image formation, and optical turbulence added by a contaminated or turbulent atmosphere can produce blur. This phenomenon is not reserved only for the formation of optical images, since it is also present in electronic microscopes (due to spherical electronic lens aberrations), corrupt CT scanner and X-rays which are affected by forced scattering in the medium [Lin and Li(2004a), Bovik(2009)].

Figure 1.2 shows the influence and contribution of different Modulation Transfer Functions in an imaging system. This illustrates that Defocus MTF can have a relevant effect on the overall MTF.

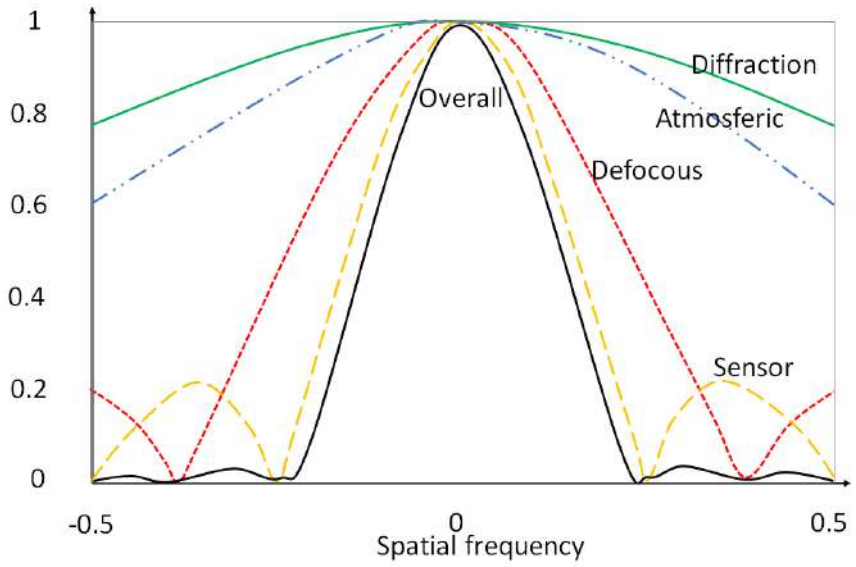

Figure 1.2: Example illustrating the contribution of the Modulation Transfer Function (MTF) of an imaging system [Gunturk(2012)].

Blur is classified into two types depending on its spatial distribution on the affected image: Spatially Invariant Blur in which high-frequency content reduction is produced in the same way over the entire image and Spatially Variant Blur, characterized by different blur levels on the same image as shown in Fig.1.3.

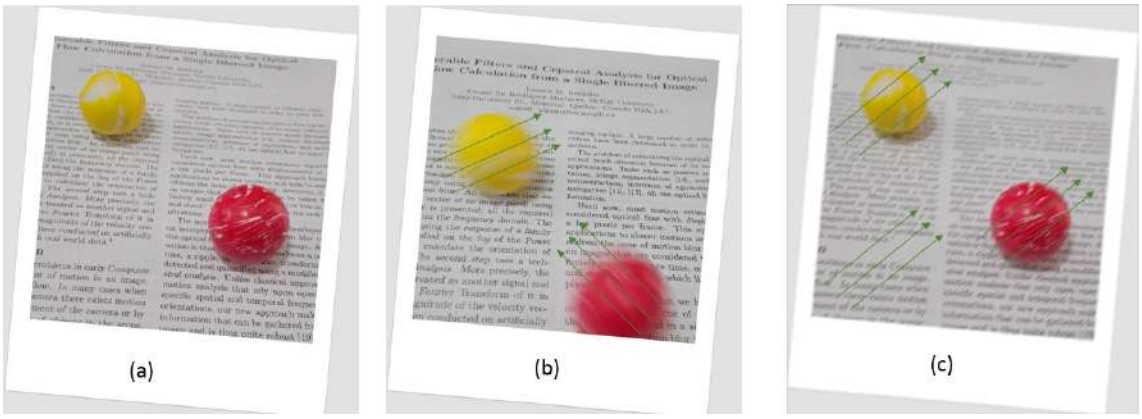

Figure 1.3: (a) Blur-free image (b) is a Spatially Variant motion blurred image and (b) is a Spatially Invariant motion blurred image .

Assuming a fixed distance and ignoring defocus effects and lens aberration, motion blur can be modeled through Eq. 1.4 where $I(x, y)$ is the non-degraded image, $g(x, y)$ is the degraded image and $n(x, y)$ is the additive process noise in image [Rajagopalan and Chellappa(2014)].

$$g(x, y) = \int\int I(\alpha, \beta)h(x - \alpha, y - \beta)d\alpha d\beta + n(x, y) \tag{1.4}$$

There is a case in which the PSF does not depend on the position of (x, y) in the image, so that $h(x - \alpha, y - \beta) = h(\alpha, \beta)$. This is called the Spatially Invariant Point Spread Function. Conversely, if the function varies in space, it is said to be a Spatially Variant Point Spread Function. See Eq. 1.5 [Lin and Li(2004a), Sorel and Flusser(2008)].

$$g(x, y) = \int\int I(\alpha, \beta)h(x - \alpha, y - \beta, \alpha, \beta)d\alpha d\beta + n(x, y) \tag{1.5}$$

Figure 1.4 illustrates the degradation block diagram of an image in Space and Frequency Domain.

Blur can be classified by its nature as: Optical, Mechanic and Medium-induced blur [Chan and Shen(2005a)]. This research only considers the mechanic blur which occurs when the relative velocity among the different objects in a scene and the camera are relatively large compared to the time of exposure so that the resulting image gets a distortion called motion blur [Lin and Li(2004a), Gunturk(2012)]. The PSF $h(x, y)$ of any blur kernel has to satisfy three constraints, namely [Bovik(2010)]:

- $h(x, y)$ does not take negative values because of the physics of the underlying image formation process.
- $h(x, y)$ is real-valued because images are real-valued.
- Energy is neither absorbed nor generated during the image formation process. For spatially continuous blurs, $h(x, y)$ is constrained to satisfy Equation 7.3.

$$\int_{-\infty}^{+\infty}\int_{-\infty}^{+\infty} h(x, y)dxdy = 1 \tag{1.6}$$

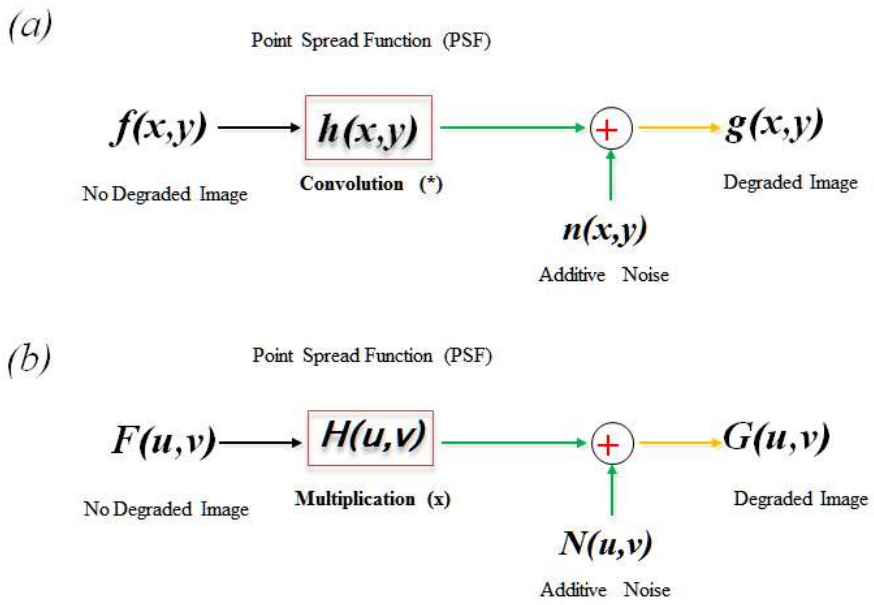

Figure 1.4: (a) Image formation model in the spatial domain (b) Image formation model in the Fourier domain.

There are two main ways that PSF physical meaning can be interpreted: the well known standard point of view which describes how the point sources are spread in space and the other one is to see the PSF as a weighted convolution window [Rajagopalan and Chellappa(2014)].

1.2 GENERAL STATE OF ART

S.C Som study [Som(1971)] is one of the most outstanding theoretical researches about the mathematical model of uniform and accelerated motion blurred images (Universite Laval Quebec, 1972). This work is concerned with the linear smear on photographic images taken with a single analogical camera that uses light-sensitive emulsion film to save the image of the scene. To this day, it is still the most cited study on linear motion blur analysis due to its extensive investigation of the uniform and accelerated motion modeling. Velocity and acceleration estimation from one single motion blurred image has not received in-depth research even its has some broad uses in robotics, forensic science, engineering, and physics among other applications. Traditionally, a motion blurred image has been considered undesired due to the little high-frequency content, refusing this one hides associated kinematic data.

Lin et al. (the National Chung Cheng University of Taiwan, 2004) [Lin and Li(2004a), Lin(2005), Lin and Li(2005)] proposed a method to obtain the speed of a vehicle from a single motion blurred image. Even though their paper is entirely comprehensive and full of detailed geometric analysis, it is just intended for speed measurement of vehicles in highways, deblurring, and recognition of license plates. They summed up that their method had an error less than 2% compared to video-based speed estimation, but they did not collect these results in controlled environment laboratory conditions which would have allowed them a more extensive scientific

evaluation of their technique.

Some researches are based on Lin's work as seen in [Lin and Li(2004a), Lin(2005), Lin and Li(2005)]. If motion blur length L and angle θ are estimated from the degraded image, the instantaneous velocity can be calculated from the ratio between the motion blur length L and the exposure time T while the speed remains constant along a linear trajectory assumption.

Perez and Rodriguez (Universidad Autónoma de Puebla in Mexico, 2005) [Pérez Huerta and Rodriguez Zurita(2005)] performed some experiments by taking pictures of letters painted on sliding carriage which was set on low friction air rail at a constant velocity and acceleration to generate linear motion blur degradation. These experiments were not meant for the estimation of velocity and acceleration; however, they presented a valid approximation to the subject of interest.

Schuon and Diepold (Technische Universität München in Germany, 2006) [Schuon and Diepold(2009),Deb(2005)] set up a motor-driven slider to generate and to take real-world blurred pictures in a controlled uniform velocity environment. They stated that for more than 30 years researchers have developed techniques for deblurring synthetic motion blurred images which work well but fail on naturally blurred images. Their experiments allowed them to find out an alternative solution to address real-world generated blurred images. They were not interested in the calculation of the target speed, but their novel deployment was encouraging for further researchers.

Celestino and Horikawa (Escola Politécnica of Sao Paulo University, 2008) [Celestino and Horikawa(2008)] implemented a new non-contact method based on image analysis to estimate the speed of a vehicle like a built-in vehicle speedometer. They calculated the Speed through the analysis of the asphalt irregularities which produced motion blurred images while the vehicle goes on and its mounted CCD Camera captures still images from the road surface. The authors stated that its speed accuracy is 2.5% in a range lower than 80 kilometers per hour under a simulated asphalt movement. Furthermore, they did not describe any automated technique to estimate blur length in their writing.

Mohammadi, Akbari and Keshavarz (Azad University in Iran, 2010) [Mohammadi et al.(2010)Mohammadi, Akbari, et al.] proposed a novel approach for vehicle speed estimation based on the motion blur occurring in the image taken by a still camera. Their strategy was based on Lin proposal in [Lin(2005), Lin and Li(2005)], but the authors only described an alternative method for the Point Spread Function reconstruction of a uniform motion blurred image based on Radon Transform in the frequency domain for length and direction estimation of motion from the projection of the Fourier pattern. They were only interested in the speed and the displacement in the interval of exposure. Mohammadi et al. stated that their proposed method increased the accuracy of speed estimation and measurement of motion blur parameters, with aided Radon Transform between 28% and 40%. Radon transform method was merely one of several methods to calculate the angle of the pattern dark lines, which was related to the direction of motion, of the 2D Fourier transform of the blurred image as shown in Figure 1.5. A newer paper of the same researchers introduced how to estimate the speed of a spherical object in the frequency domain in 2013 [Mohammadi and Taherkhani(2013)]. They set the case that the moving object traveled along a direction perpendicular to the optical axis of the camera;

hence the angle of motion direction was zero. On the other hand they calculated the distance between lines in the Fourier spectrum to estimated the motion blur length according to the model described in Figures 1.5 and 1.6 by collapsing the pattern along the motion axis.

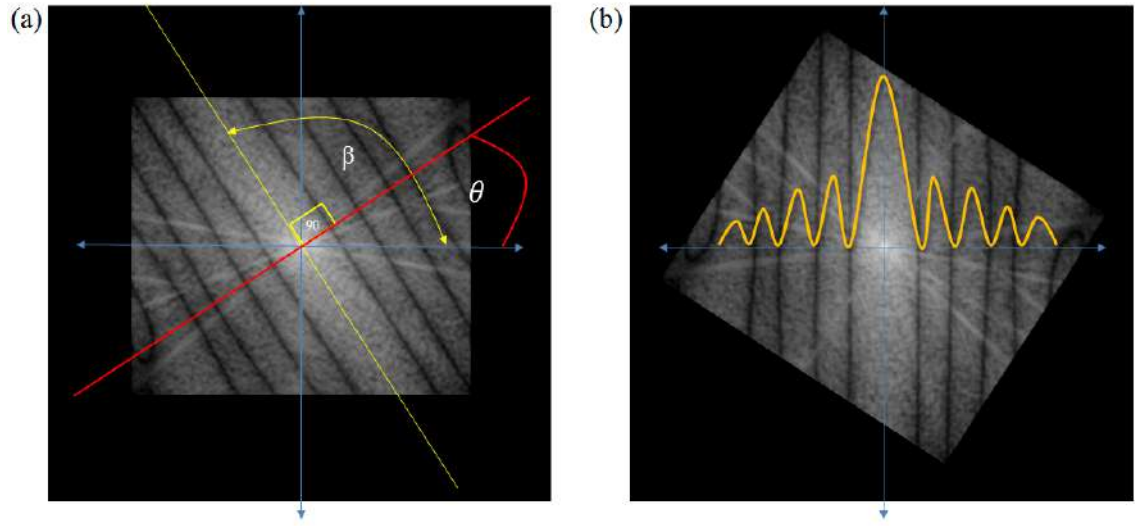

Figure 1.5: (a) illustrates how to calculate the angle from the Fourier Pattern and (b) shows the rotated pattern and its Sinc function sketch on the image.

In their paper, Olivas, Sorel, Nikzad and Ford (University of California San Diego, 2012) [Olivas et al.(2012)Olivas, Šorel, and Ford] introduced a computational imaging system that incorporated an optical position sensing detector array and a regular camera to reconstruct images degraded by spatially variant motion blur using a sliding platform. They built a prototype system capable of capturing consistent motion blurred images while performing tracking by using position detectors. Their setup was not intended to measure kinematic quantities, but the deployment was proper for motion blur research.

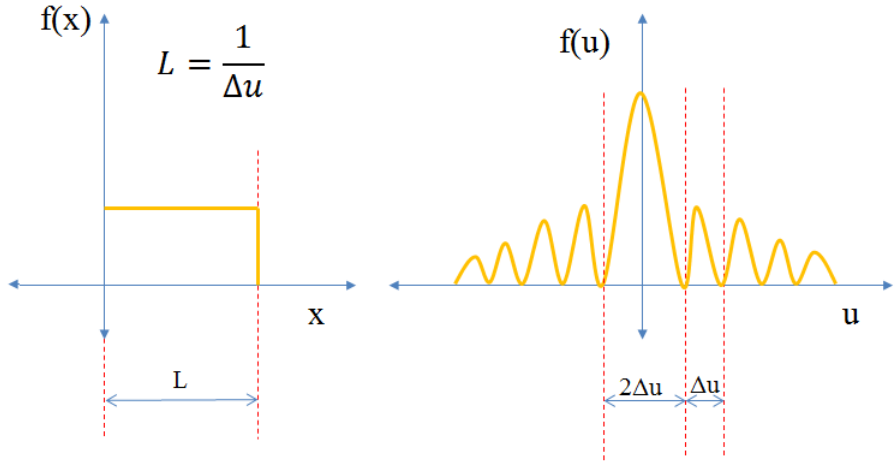

Figure 1.6: (a) shows the Gate Function for spatially invariant motion blurred image system and (b) is its frequency response. [Dobeš et al.(2010)Dobeš, Machala, and Fürst]

Nemeth and Zarandy (Hungarian Academy of Sciences in Hungary, 2016) [Nemeth and Zarandy(2016)] proposed a method to calculate the speed of vehicles using the light trace produced on motion blur images. The suggested method estimated speed based on the saturated regions of the image, so light conditions were a critical aspect. Finally, they indicated that speed-accuracy was 5% in actual images.

Lee et al. (Korea Advanced Institute of Science and Technology in south Korea, 2017) [Lee et al.(2016)Lee, Kim, and Kim,Lee(2017),Lee et al.(2017)Lee, Kim, Cho, and Kim] introduced a method for estimating the velocity of a vehicle using a moving camera in a different direction of the car motion. They stated in their work that the inclination of the motion blur pattern line of the single image was directly related to the resulting velocity vector of the vehicle and the known modulation speed. Also, they denoted that the level of inclination could be measured using line extraction methods such as the Hough transform or the Gabor filter. They found that the longitudinal velocity absolute error was less than $2.13km/h$ and that The proposed method was independent of the exposure time. Finally, they concluded that their proposal could be used for vehicular technology.

Jing et al. (School of Oil & Gas Engineering, Southwest Petroleum University in China, 2018) [Jing et al.(2018)Jing, Xiao, Yang, Wang, and Yu] proposed a defocus correction method to obtain the velocity of particles a single-frame & single-exposure image (SFSEI). Their approach was based on the change of focus, size, and shape of close and far particles shot on a single motion-blurred image. This method was confirmed in a free-falling particle experiment. Finally, the researchers found that the average deviation of particle velocity between measured values and numerical solutions was 6.1%.

Matsuo et al. (Faculty of Science and Technology, Keio University, Yokohama in Japan, 2018) [Matsuo and Yakoh(2018)] showed a method to find the position and measure velocity from a single motion blur by detecting the stat and the endpoint of the blur. The researches noticed that under constant illumination environment the motion direction start and end could not be determined. To solved this issue, they used modulated illumination adopting a red light illumination at the beginning and blue light at the end to tag the blurred image. As a conclusion, the method has not been yet used in an actual conditions.

Dwi Cahya et al. (Informatics and Computer Departments Electronic Engineering Polytechnic in Indonesia, 2018) [Dwicahya et al.(2018a)Dwicahya, Ramadijanti, and Basuki] presented a method to estimate the speed of regular plain shapes based on the grayscale levels. They made a micro-controlled prototype to rotate the object and, in this way, produce motion blur. They stated that the identification approach of blur parameters used in was in the frequency domain. The authors did not provide detailed information about how to measure blur length. Finally, they concluded that their method was not suitable for images of circular objects. Additionally, they denoted that the accuracy level was 93.06%. This study is still undergoing research.

Zhou et al. (Nanjing University of Aeronautics and Astronautics in China, 2019) [Zhou et al.(2019)Zhou, Chen, Zhang, Ye, and Tao] adopted a motion blur modeling for accurate 3D reconstruction and speed estimation of rotating objects such as rotating helicopter blades in wind tunnel testing. They used two synchronized and calibrated cameras to take a temporal series of image pairs of coded targets (CTs) on the surface of blades to serve as visual features.

This feature matching-based algorithm depends on the motion estimation between contiguous target image pairs. In their experiments, they used a rotating fan at 120 rpm and a convolutional neural network to recognize the CTs change of position during the known exposure time. Even though they did not calculate the speed explicitly of the blades, they concluded that their method benefits high-speed object measurement applications.

1.2.1 Strategies to estimate length and angle of motion blurred images

There are basically three strategies to estimate the angle and the blur length. One is based on space, the other one in the frequency domain (See Figures 1.7, and 1.8) and the last one in the Wavelet domain. The space and the frequency approaches have been widely studied for the reconstruction of PSF and, thereafter, to do deconvolution. Even though there are some works on the Wavelet Domain, they do not allow estimating the PSF parameters, only to locate blur in on image [Liu et al.(2008)Liu, Li, and Jia]. Zhang and Hirakawa (University of Dayton, 2013) [Zhang and Hirakawa(2013a), Zhang and Hirakawa(2013b)]study was one of the few studies that involved the procedure to reconstruct the kernel and to find out a non-degraded image in the Wavelet transform.

Guo, Wang and Liu (Chongqing University in China, 2013) presented a method to identify the PSF of motion blurred images based on two-dimensional discrete Wavelet transform (2D-DWT) and Cepstrum. The principal idea was to determine the blur length and the blur direction by using 2D-DWT on the motion blur image, and then detecting the decomposed image with the Cepstral analysis [Guo and Wang(2013)].

Motion Blur Orientation Angle Estimation

Space Domain

Phansalkar (College of Engineering in India, 2010) presented one of the simplest methods that assumes a spatially invariant linear blur over the whole image and uses the Hough transform in space. The entire image was gridded into smaller parts of the same image, and then the Hough transform was applied to each resulting rectangle. The motion blur length and angle were statistically estimated from the set of collected data on each grid. The author indicated that these algorithms were not completely automatic and require user interaction at some-time [Phansalkar(2010a)].

Group-Szabo and Shibata proposal (University of Tokyo in Japan, 2009) [Grou-Szabo and Shibata(2009a)] was based on edge detection. They asserted that blurred images had little high-frequency content, so edges were dismissed and only motion blur lines were kept. Motion blur angle was found by rotating the image at different angles, and then an edge detector was applied on these. The angle with the highest difference in edge count and its corresponding perpendicular angle was determined and considered to be the angle at which shifting has occurred.

There are also some machine learning methods, but they are based on the premise the original non-degraded image is known. These methods use different classification techniques such as Neural Networks [Grou-Szabo and Shibata(2009a), Aizenberg et al.(2000)Aizenberg, Aizenberg, Butakov, and Farberov] and Support Vector Regression [Li et al.(2007)Li, Mersereau, and Simske].

Chen, Yang, Wu, and Zhao (Shanghai Jiao Tong University in China and University of Technologyin Australia, 2010) [Chen et al.(2010)Chen, Yang, Wu, and Zhao] stated on their paper that high-frequency energy decreased significantly along motion direction on a blurred image, so the motion direction angle could be estimated by detecting the lowest directional high-frequency energy where it was regarded as the sum of the squared derivative of the image. They summed up that their proposed method could produce more accurate results with less computation.

Frequency Domain

Tiwari, Shukla and Singh (Institute of Technology in India, 2013) in their review explained that blur direction could be identified using Hough Transform to detect the orientation of the line in the log magnitude spectrum of the blurred image. They concluded that the angle of motion blur related to the Dark lines in the Fourier Frequency Domain [Tiwari et al.(2014)Tiwari, Singh, and Shukla, Lokhande et al.(2006)Lokhande, Arya, and Gupta, Su et al.(2012)Su, Lu, and Lim, Moghaddam and Jamzad(2007), Dobeš et al.(2010)Dobeš, Machala, and Fürst].

Mughaddam and Jamzad (University of Technology in Iran, 2004) also studied an alternative technique to estimate motion blur angle to overcome some Hough transform issues. Radon transform can be applied to the Fourier Spectrum without needing to convert the image to a binary format as Hough methods require. It makes this approach more accessible and faster to implement [Tiwari et al.(2014)Tiwari, Singh, and Shukla, Moghaddam and Jamzad(2007), Jia and Wen(2013), Krahmer et al.(2006)Krahmer, Lin, McAdoo, Ott, Wang, Widemann, and Wohlberg, Pazhoumand-Dar et al.(2010)Pazhoumand-Dar, Abolhassani, and Saeedi]. Later, Ji and Liu (National University of Singapore, 2008) also introduced a hybrid Fourier-Radon transform to estimate the parameters of the blurring kernel with improved robustness to noise [Ji and Liu(2008)].

Rekleitis (University St in Canada, 1996) [Rekleitis(1996), Krahmer et al.(2006)Krahmer, Lin, McAdoo, Ott, Wang, Widemann, and Wohlberg] proposed to apply a family of steerable filters such as Gaussian and Gabor on the log of the power spectrum image and evaluate the highest response angle.

Krahmer et al. (Los Alamos National Laboratory in USA, 2014) [Tiwari et al.(2014)Tiwari, Singh, and Shukla, Ji and Liu(2008), Krahmer et al.(2006)Krahmer, Lin, McAdoo, Ott, Wang, Widemann, and Wohlberg, Tiwari and Shukla(2013)] stated in their paper that if the noise level of the blurred image was not too high, there will be two pronounced peaks in the Cepstrum. They proposed to draw a straight line from the origin to the first negative peak to estimate the angle of motion blur. This was approximated by the inverse tangent of the slope of this line in the Cepstral plot.

Cannon (University of Utah, 1974) [Cannon(1976)] stated in his paper that zeros of $G(u, v)$ are related to the zeros of $F(u, v)$ and $H(u, v)$, therefore, he asserted that if we have the PSF, the parametric values of the blur can be found. This is done by tracing the zero crossing of the frequency response of the blurred image. Motion blur has its zeros along lines perpendicular to the direction of the blur, and they are separated each other at a regular interval $1/\Delta u$ as seen in Fig.1.6. This technique had a low computational complexity and reliability, but failed

when SNR was low [Kundur and Hatzinakos(1996),Dash(2012)]. Yitzhaky et al. (University of Negev in Israel, 1998) [Yitzhaky et al.(1998)Yitzhaky, Mor, Lantzman, and Kopeika] considered that the spectral domain zeros technique was not suitable for the study of accelerated motion degradation and low-frequency vibrations.

Figure 1.7 sums up the techniques previously presented to estimate the motion blur angle in space domain.

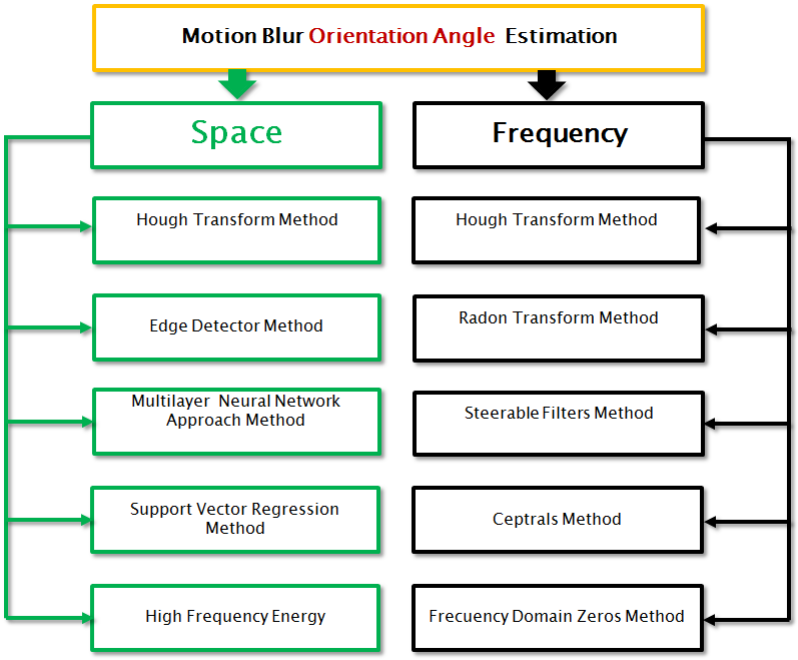

Figure 1.7: Motion blur Angle estimation techniques

Motion Blur Length Estimation

The reader can find out that some of the following proposed techniques to estimate motion blur extent are based on similar methods such as those described before for motion blur angle estimation.

Space Domain

Phansalkar (College of Engineering in India, 2010) [Phansalkar(2010a)] stated that once the motion blur angle has been calculated, the motion blur length can be estimated. They applied the Hough transform to the entire edge image which was gridded. They claimed that all the lines of length above certain threshold and making an angle θ with X-axis in the counterclockwise direction are averaged to obtain the actual angle. After the angle had been determined, the pixel displacement length could be estimated. Finally, they also suggested that human intervention was needed to stop the algorithm. An edge detector was swept over the convoluted image until the wave-patterns on the image were dissolved. When these periodic patterns were not present, the actual length could be estimated [Grou-Szabo and Shibata(2009a)].

Yang et al. (Guizhou University in China, 2011) [Yang et al.(2011)Yang, Liu, Liu, and Liao] suggested that motion blur length could be estimated by measuring the ringing artifact amount of the deblurred image. Ringing artifacts are ripples that appear near strong edges. They also stated that the correct motion blur length caused minimum ringing artifacts on the image, so the main ringing artifacts could be obtained by using a high-pass filter response.

Frequency Domain

Moghaddam and Jamzad algorithm (Sharif University of Technology in Iran, 2006) was based on the central peaks and valleys in the Fourier spectrum collapsed pattern. they used the parallel dark lines that appeared in the Fourier spectrum of the degraded image to find motion length. It could be estimated as illustrated in Figure 1.6. All valleys were candidates of dark line places but some of them could be false. The best ones were valleys that correspond to Sinc function in the Fourier spectrum. These valleys were located in two sides of the central peak [Moghaddam and Jamzad(2007)] (Also review [Dobeš et al.(2010)Dobeš, Machala, and Fürst] from Dobes, Machala, and Furst in 2010).

Sakano, Suetake, and Uchino algorithm (Yamaguchi University, Yamaguchi in Japan, 2006) [Moghaddam and Jamzad(2007)] found the dark lines in the Fourier spectrum pattern by a modified version of the Hough Transform. According to the authors, the algorithm could accurately and robustly estimate the motion blur PSF even in a highly noisy case.

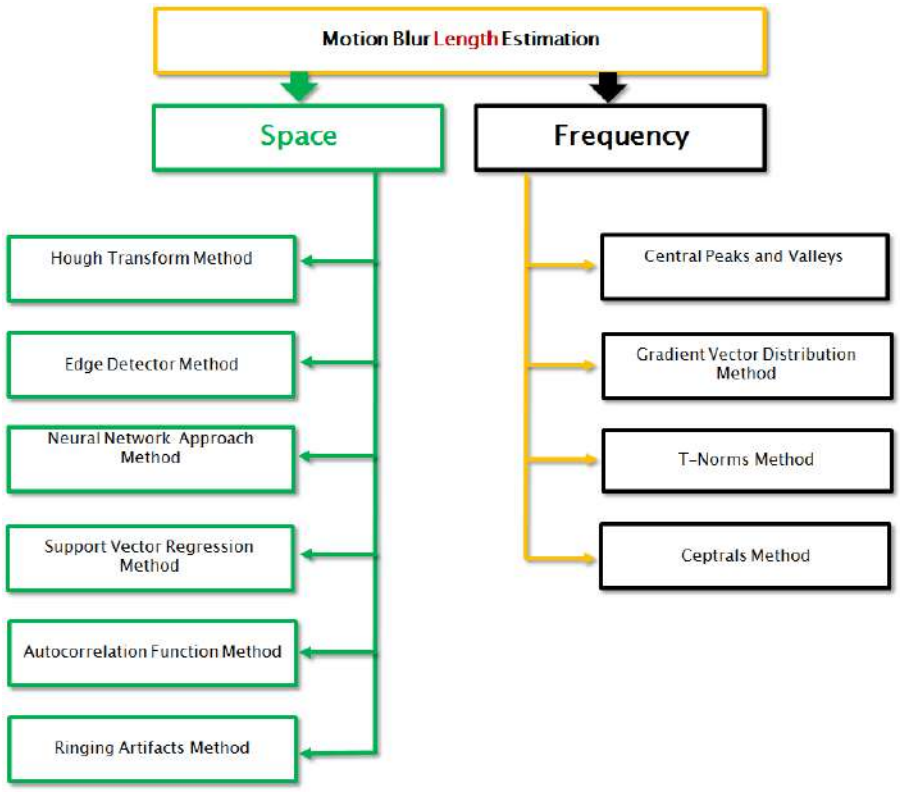

Figure 1.8: Motion blur length estimation techniques

1.3 SUMMARY

This thesis is divided into six selft-contained chapters. Chapter 1 introduces in a general manner the relevance of this study. Likewise, this chapter presents the state of the art through the review of the scientific literature related to the estimation kinematic quantities from motion blur images.

In Chapter 3, I firstly present detailed modeling of the Point Spread Function for uniform and accelerated motion blurred images using the Fourier Transform, and finally the Cosine Transform.

Chapter 4 focuses on the estimation of the Point Spread Function in synthetically motion blurred images. In this one, I explored some of the traditional approaches for the estimation of the linear motion blur parameters, namely, angle and length in noisy conditions. Continuedly, I suggest an alternative approach based on the cosine transform which results highly noise tolerant as presented.

Chapter 5 proposes an alternative to the estimation of relative velocity from a single actual linear motion blurred image using the cosine transform for an object moving at a constant velocity under invariant blur conditions. Certainly, the proposed alternative method overcomes all competitors evaluated.

Chapter 6 goes further and estimates the acceleration using a single motion blur image. This approach has not been explored in using blur as a source of kinematic information as presented here. The suggested method evaluates some machine learning regression algorithms extensively and uses homomorphic filtering to extract the characteristic PSF for training.

Chapter 7 introduces proof of concept to ensure that spatially variant motion blur also allows estimating blur length using the proposed DCT method. As mentioned in Chapter IV, blur length L and exposure time T are needed to calculate relative motion speed in invariant motion blur images. This is a piece of evidence that blur length estimation is possible using only a motion blur region of the image.

Finally, on Chapter 8, we present the design and the construction of an electromechanical slider, which is not a minor matter. It endures all the Metrologic framework needed to estimate the accuracy of the velocity and the acceleration estimated from the linear motion blur image. It provides ground truth values. Even though there exist some commercial sliders used in movies and advertisements production, none gives data about its speed uncertainty and far less about acceleration, among other issues.

Chapter 2

RESEARCH HYPOTHESIS

It is possible to estimate the acceleration from a a single uniformly accelerated motion blurred image taken in a controlled environment, starting from the Point Spread Function model found in space and frequency domain and the blur itself.

2.1 OBJECTIVES

2.1.1 General

To estimate fundamental kinematic quantities from a single linear motion blurred image taken in a controlled environment in an uniformly accelerated motion, using an approximated Point Spread Function model computed from the image. The image contains a fixed background and a moving object whose shape and color are known. The object motion is restricted to the plane perpendicular to the main axis of the camera.

2.1.2 Specific

- To model a Point Spread Function from the blur using linear uniformly accelerated motion.
- To propose a kinematic function to describe motion in time from a single linear motion blurred image using the approximated PSF model.
- To estimate the trajectory, the speed and the acceleration of an object from a single linear motion blurred image.

Chapter 3

MOTION BLUR MODELING

Mathematical Modeling is a significant instrument that strengthens the understanding of linear motion blur. In this chapter, we firstly reviewed a classical model based on the Fourier Transform. Even though it results in a regular solution that explains the phenomenon, its complex mathematical approach adds further elements to consider. Alternatively, we explored the Continuous Cosine transform that simplifies the model using only real numbers and providing an analogous equivalent solution. Finally, as shown in a later chapter, the Discrete Cosine Transform results more suitable when extracting the Point Spread function in motion blur degraded images.

3.1 MOTION BLUR MODELING USING FT

Motion blur Blur degradation of an image arises mainly when relative motion between the camera and the scene occurs during the exposure time T of imaging sensor to light. Although the motion blurred image is considered degraded, it has some kinematic information that can be presented concerning a function called Effective Propagation Function. Soms in [Som(1971)] described how to analyze the characteristics of an image to obtain information from it. As a first step, He introduced a function $f(x, y)$, called Irradiance Distribution, that is defined analytically and is square integrable in all its domain. This function is known as the relative linear motion of the photographic image in the positive side of the x-axis, for a given time t. Also, a continuous displacement function $s(t)$ is assumed at all t, the total exposure time T, and Total Effective Exposure $E_e(x, y)$ is introduced as follows in Eq.3.1:

$$E_e(x, y) = C_1 \int_0^T f[x - s(t), y] * e(x, y)dt \tag{3.1}$$

Where $e(x, y)$ is the emulsion PSF, C_1 is a constant that depends on the photographic material, and $*$ means the convolution operation. if motion is only along the x-axis, then the Taylor series of $f[x - s(t), y]$ can be considered in a single dimension. Starting from the definition shown in Eq.3.2 for Taylor's:

$$f(x) = \sum_{n=0}^{\infty} \frac{(x - a)^n}{n!} f^{(n)}(a) \tag{3.2}$$

Then:

$$f(x) = \sum_{n=0}^{\infty} \frac{(x - s(t))^n}{n!} f_x^{(n)}(s(t))$$

$$f(x) = \sum_{n=0}^{\infty} \frac{(-s(t))^n}{n!} f_x^{(n)}(x, y)$$

$$f(x) = \sum_{n=0}^{\infty} \frac{(-1)^n (s(t))^n}{n!} f_x^{(n)}(x, y) \tag{3.3}$$

Replacing Eq.3.3 in Eq.3.1:

$$E_e(x, y) = C_1 \int_0^T \left[\sum_{n=0}^{\infty} \frac{(-1)^n s(t)^n}{n!} f_x^{(n)}(x, y) \right] * e(x, y) dt$$

Later, moving the integral:

$$E_e(x, y) = C_1 \left[\sum_{n=0}^{\infty} \frac{(-1)^n \int_0^T s(t)^n}{n!} f_x^{(n)}(x, y) \right] * e(x, y) dt$$

Defining A_n:

$$A_n = \int_0^T s(t)^n dt \tag{3.4}$$

$$E_e(x, y) = C_1 \left[\sum_{n=0}^{\infty} \frac{(-1)^n A_n}{n!} f_x^{(n)}(x, y) \right] * e(x, y) \tag{3.5}$$

Equation 3.5 is an explicit description of the actual exposure. It tells that the physical image, in its acquisition, is described by a function proportional to the Total Effective Exposure (photograph processing is linear during exposure), then:

$$I(x, y) = C_2 E_e(x, y)$$

where C_2 is a proportionality constant. Then the functions are transformed to the Fourier Frequency domain, since the convolution operator becomes a simple point-wise multiplication which reduces the calculations dramatically. Now, The Fourier Transform is introduced in two dimensions to perform the first step, as shown in Eq.3.6:

$$P(u, v) = \int_{-\infty}^{\infty} \int_{-\infty}^{\infty} p(x, y) e^{-2i\pi(ux+vy)} dx dy \tag{3.6}$$

Substituting $p(x, y) = f_x^n(x, y)$ into Eq.3.6, the Fourier Transform of the derivative function is obtained in Eq.3.7:

$$P(u, v) = \int_{-\infty}^{\infty} \int_{-\infty}^{\infty} f_x^{(n)}(x, y) e^{-2i\pi(ux+vy)} dx dy = (i2\pi u)^n F(u, v) \tag{3.7}$$

Now, substituting Eq.3.7 into Eq.3.5:

$$I(u,v) = C_2(i2\pi u)^n F(u,v) C_1 \left[\sum_{n=0}^{\infty} \frac{(-1)^n A_n}{n!}\right] E(u,v),$$

$$I(u,v) = C_2 C_1 F(u,v)[\sum_{n=0}^{\infty} \frac{(i2\pi u)^n (-1)^n A_n}{n!}]E(u,v),$$

Letting $C = C_1 C_2$

$$I(u,v) = CF(u,v)[\sum_{n=0}^{\infty} \frac{(-i2\pi u)^n A_n}{n!}]E(u,v)$$

Then, from Eq.3.4 :

$$I(u,v) = CF(u,v)E(u,v)\left[\sum_{n=0}^{\infty} \frac{(-i2\pi u)^n \int_0^T s(t)^n dt}{n!}\right]$$

$$I(u,v) = CF(u,v)E(u,v)\int_0^T \left[\sum_{n=0}^{\infty} \frac{(-i2\pi u)^n s(t)^n}{n!}\right] dt$$

$$I(u,v) = CF(u,v)E(u,v)\int_0^T [\sum_{n=0}^{\infty} \frac{(-i2\pi u\, s(t))^n}{n!}]dt \tag{3.8}$$

The term $\sum_{n=0}^{\infty} \frac{[-i2\pi u\, s(t)]^n}{n!}$, from Eq.3.8, has the basic form of Taylor series e^x :

$$e^x = \sum_{n=0}^{\infty} \frac{x^n}{n!}$$

Where $x = -i2\pi u\, s(t)$

$$\sum_{n=0}^{\infty} \frac{[-i2\pi u\, s(t)]^n}{n!} = e^{-i2\pi u\, s(t)}$$

$$I(u,v) = CF(u,v)E(u,v)\int_0^T e^{-i2\pi u\, s(t)} dt$$

$$L(u) = \int_0^T \sum_{n=0}^{\infty} \frac{[-i2\pi u\, s(t)]^n}{n!} dt = \int_0^T e^{-i2\pi u\, s(t)} dt$$

$$I(u,v) = CF(u,v)L(u,v)E(u,v)$$

The functions $I(u,v)$, $F(u,v)$, $E(u,v)$ are the Fourier Transforms of $I(x,y)$, $F(x,y)$, $E(x,y)$, respectively. These are considered the characteristics of the image, each of them is independent from the other; therefore they can be calculated, separately, and superposed. For this study, only Eq.3.9 is considered because it describes the blur in the image.

$$L(u) = \int_0^T e^{-i2\pi u\, s(t)} dt \tag{3.9}$$

When there is no blur, the function must be equal to an instant time T :

$$L(u) = T \quad for\ all\ u$$

Therefore, 3.9 is equal to:

$$L(u) = \frac{1}{T} \int_0^T e^{-i2\pi u\, s(t)} dt$$

The displacement is called blur and dependents on time $s(t)$. Furthermore, the speed $v(t) = \frac{d[s(t)]}{dt}$ also relays explicitly on the displacement using Eq.3.10:

$$g(s(t)) = v(t) = \frac{d\,[s(t)]}{dt} y dt = \frac{d\,[s(t)]}{v(t)} \tag{3.10}$$

Now, replacing Eq.3.10 into Eq.3.9 to make it depend on the speed at any time $0 < t < T$.

$$L(u) = \frac{1}{T} \int_0^T \frac{e^{-i2\pi u\, s(t)}}{v(t)} d\,[s(t)]$$

$$L(u) = \frac{1}{T} \int_0^T \frac{e^{-i2\pi u\, s(t)}}{g(s)} ds$$

$$L(u) = \int_0^T \frac{e^{-i2\pi u\, s(t)}}{T g(s)} ds$$

Let

$$l(s) = \frac{1}{T\, g(s)} \quad or \quad l(s) = \frac{1}{T\, v(t)} \tag{3.11}$$

$$L(u) = \int_0^T l(s)\, e^{-i2\pi u\, s(t)} ds \tag{3.12}$$

This is the general equation for a blur $s(t)$ at speed $g(s(t)) = v(t)$ in the time interval $0 < t < T$.

3.1.1 Uniform Velocity

Considering an uniform velocity $g(s) = v = v_0$, the blur length is $s = v_0 t$; therefore $l(s) = \frac{1}{T\, v_0}$, where $T \times v = x$ =constant, we can say that $l(s) = \frac{1}{x}$ in the interval $0 < s < x$ and zero at any other.

$$L(u) = \frac{1}{x}\int_0^x e^{-i2\pi u\, s(t)} ds \tag{3.13}$$

The function in Eq.3.13 is integrated:

$$L(u) = \frac{1}{x}\,\frac{e^{-i2\pi ux} - e^0}{-2\pi iu}$$

$$L(u) = \frac{e^{-i2\pi ux} - 1}{-2\pi iux}$$

Grouping the common factor $e^{-i\pi ux}$:

$$L(u) = \frac{e^{-i\pi ux}(e^{-i\pi ux} - e^{i\pi ux})}{-2\pi iux}$$

$$L(u) = e^{-i\pi ux}\frac{(e^{-i\pi ux} - e^{i\pi ux})}{-2\pi iux}$$

The sine of an angle, in terms of Euler identity, is defined as:

$$\sin\theta = \frac{e^{i\theta} - e^{-i\theta}}{2i}$$

It is obtained that:

$$L(u) = e^{-i\pi ux}\frac{\sin(\pi ux)}{\pi ux}$$

Where:

$$\frac{\sin x}{x} = \mathrm{Sinc}(x)$$

$$L(u) = \mathrm{Sinc}(\pi ux)e^{-i\pi ux} \tag{3.14}$$

The term $e^{-i\pi ux}$ represents the phase of the image, as its is dimensionless, it does not affect the image in its structure, only amplifies it, so it is not considered. Different displacement values will now be used $x_1 = 0.05$ mm, $x_2 = 0.1$ mm, $x_3 = 0.5$ mm, in Eq.3.14 which is an important part of study and provides information about the blur parameters. See Figure 3.1.

3.1.2 Uniform acceleration

For the case of uniform acceleration, the speed $v(t)$ and the blur $s(t)$ can be found using Eq.3.15 and Eq.5.4, respectively:

$$s(t) = v_0 t + \frac{1}{2}at^2 \tag{3.15}$$

$$v(t) = v_0 + at \tag{3.16}$$

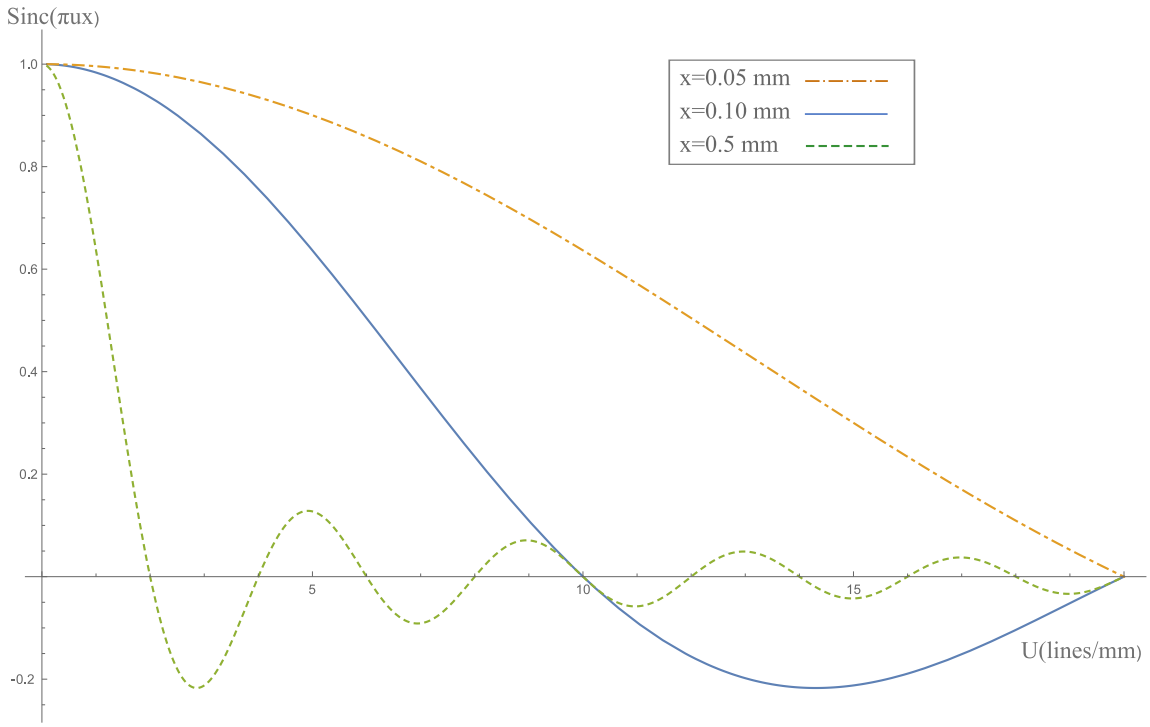

Figure 3.1: The Transfer function due to linear motion blur. We have the function sinc on the vertical axis and $u = \frac{m}{x}$ on the horizontal axis, with $m = 1, 2, 3, ...$

Time t is derived from Eq.3.16:

$$t = \frac{v - v_o}{a}$$

Then, it is replaced into Eq.3.15:

$$s = v_0 \left(\frac{v - v_o}{a}\right) + \frac{1}{2} a \left(\frac{v - v_o}{a}\right)^2$$

$$s = v_0 \left(\frac{v - v_o}{a}\right) + \frac{1}{2} a \left(\frac{v^2 - 2v_o v + v_o^2}{a^2}\right)$$

$$s = v_0 \left(\frac{v - v_o}{a}\right) + \frac{1}{2} \left(\frac{v^2 - 2v_o v + v_o^2}{a}\right)$$

$$s\, a = v_0 \left(v - v_o\right) + \frac{1}{2} \left(v^2 - 2v_o v + v_o^2\right)$$

$$s\, a = v_0 v - v_o^2 + \frac{1}{2} v^2 - v_o v + \frac{1}{2} v_o^2$$

$$s\, a = \frac{1}{2} v^2 - \frac{1}{2} v_o^2$$

$$2s\, a = v^2 - v_o^2$$

$$v^2 = v_o^2 + 2s\,a$$

$$g(s) = v = \pm\sqrt{v_o^2 + 2s\,a} \tag{3.17}$$

Consequently, using Eq.3.11

$$l(s) = \frac{1}{T}(v_0^2 + 2a\,s)^{-1/2} \tag{3.18}$$

Assuming v_o is the speed at $t = 0s$ and a is the uniform acceleration in the interval $0 < s < x$ and zero at any other. An important parameter is the ratio $R = \frac{v_o^2}{a}$, which can be integrated as $l(s) = \frac{1}{T}(1 + \frac{2s}{R})^{-1/2}$. Considering this ratio with $R = (0.001,\ 0.01,\ 0.02)$ mm and $x_1 = 0.05$ mm, $x_2 = 0.1$ mm, $x_3 = 0.5$ mm, moving an offset s, Fig.3.2, 3.3, 3.4 are obtained, respectively:

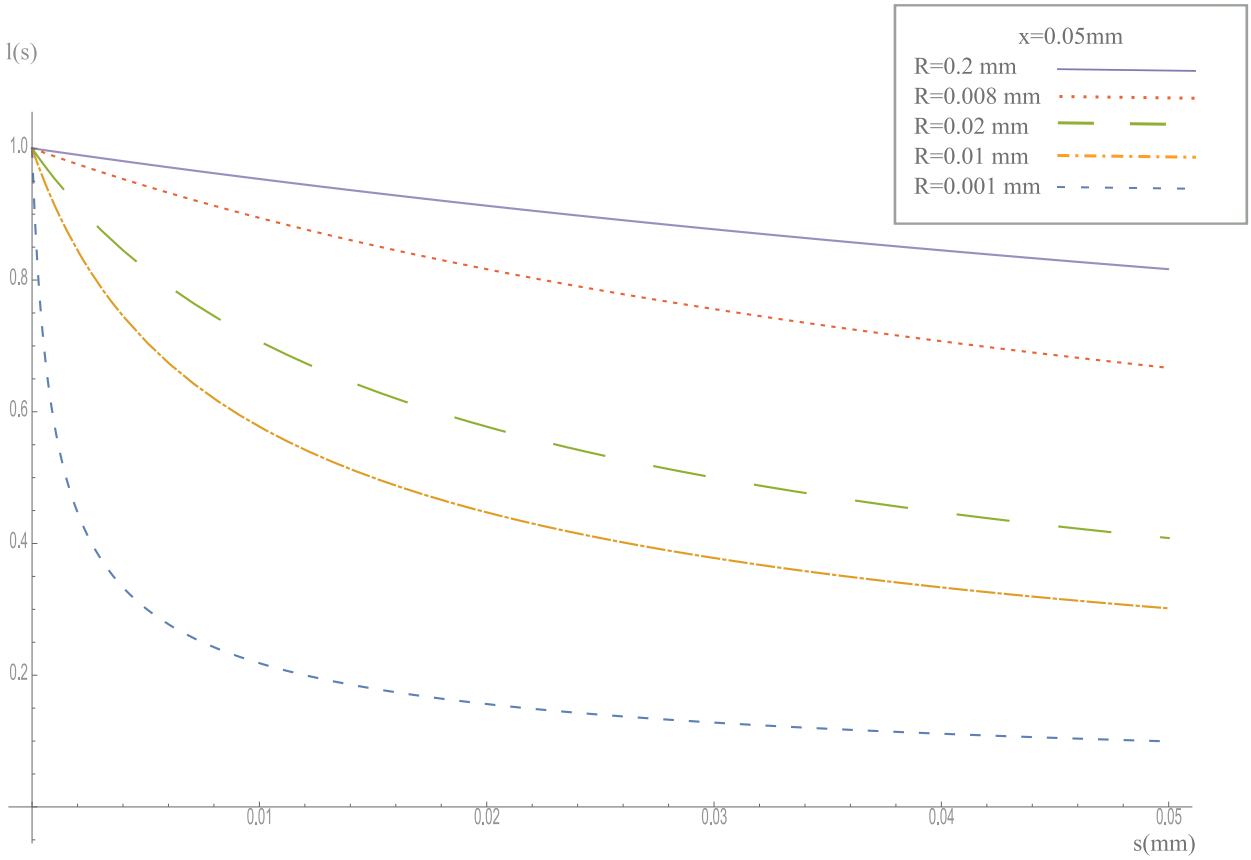

Figure 3.2: Plot of the PSF $l(s)$ of uniformly accelerated motion for with $x = 0.05$ mm, and $R = 0.001$ mm.

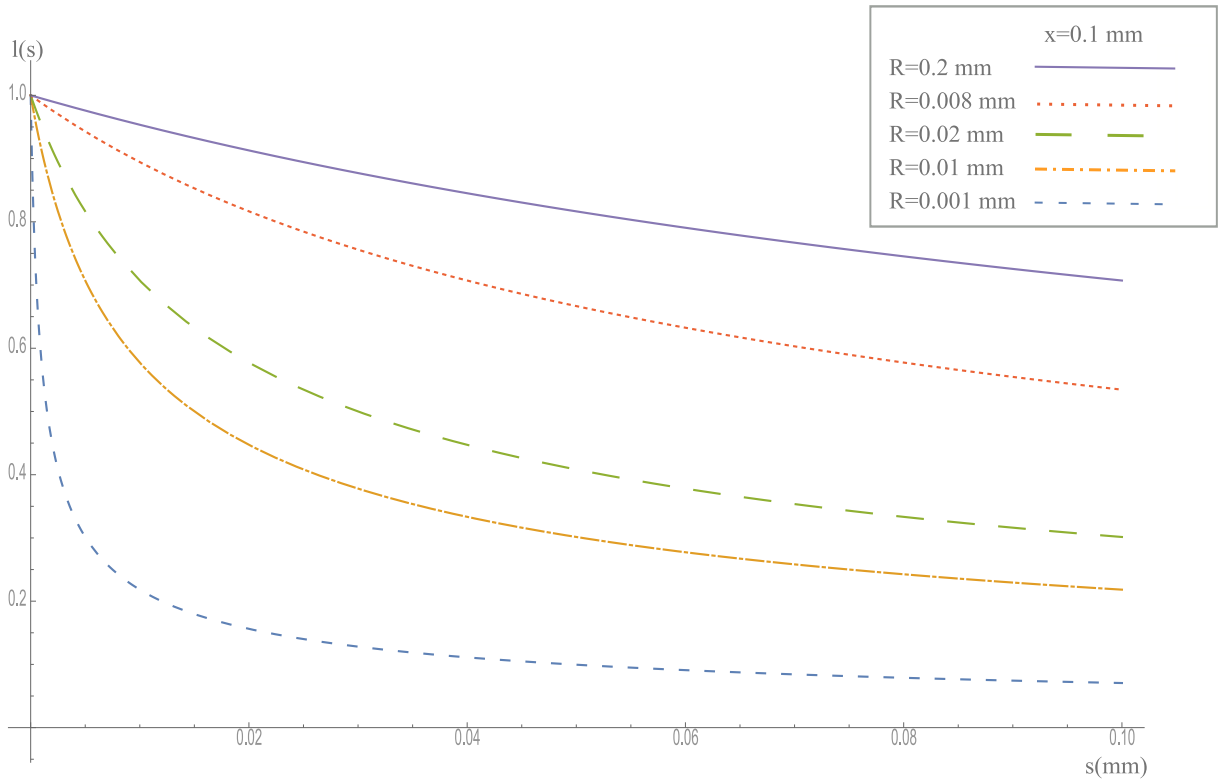

Figure 3.3: Plot of the PSF $l(s)$ of uniformly accelerated motion for with for $x = 0.1$ mm, and $R = 0.01$ mm.

The integral for the uniform acceleration is estimated from the general $L(u)$ function by replacing the acceleration function $l(s)$ shown in Eq.3.18 into Eq.3.12:

$$L(u) = \frac{1}{T}\int_0^x \frac{e^{-i2\pi u\, s(t)}}{(v_0^2 + 2as)^{1/2}} ds$$

A change of variable is performed by multiplying by one the numerator using $e^{iu(2\pi\, s + \frac{v_o^2 \pi}{a})} e^{-iu(2\pi\, s + \frac{v_o^2 \pi}{a})} = 1$ and dividing the denominator of the integral by one using $\left(\frac{\pi}{a}\right)^{1/2}\left(\frac{a}{\pi}\right)^{1/2} = 1$:

$$L(u) = \frac{1}{T}\int_0^x \frac{e^{-i2\pi u\, s} e^{iu(2\pi\, s + \frac{v_o^2 \pi}{a})} e^{-iu(2\pi\, s + \frac{v_o^2 \pi}{a})}}{(v_0^2 + 2as)^{1/2}\left(\frac{\pi}{a}\right)^{1/2}\left(\frac{a}{\pi}\right)^{1/2}} ds$$

$$L(u) = \frac{1}{T}\int_0^x \frac{e^{-i2\pi u\, s + iu(2\pi\, s + \frac{v_o^2 \pi}{a})} e^{-iu(2\pi\, s + \frac{v_o^2 \pi}{a})}}{(\frac{\pi v_0^2}{a} + 2\pi\, s)^{1/2}\left(\frac{a}{\pi}\right)^{1/2}} ds$$

$$L(u) = \frac{1}{T}\int_0^x \frac{e^{iu\frac{v_o^2 \pi}{a}} e^{-iu(\frac{v_o^2 \pi}{a} + 2\pi\, s)}}{(\frac{\pi v_0^2}{a} + 2\pi\, s)^{1/2}\left(\frac{a}{\pi}\right)^{1/2}} ds$$

The following variable changes are done:

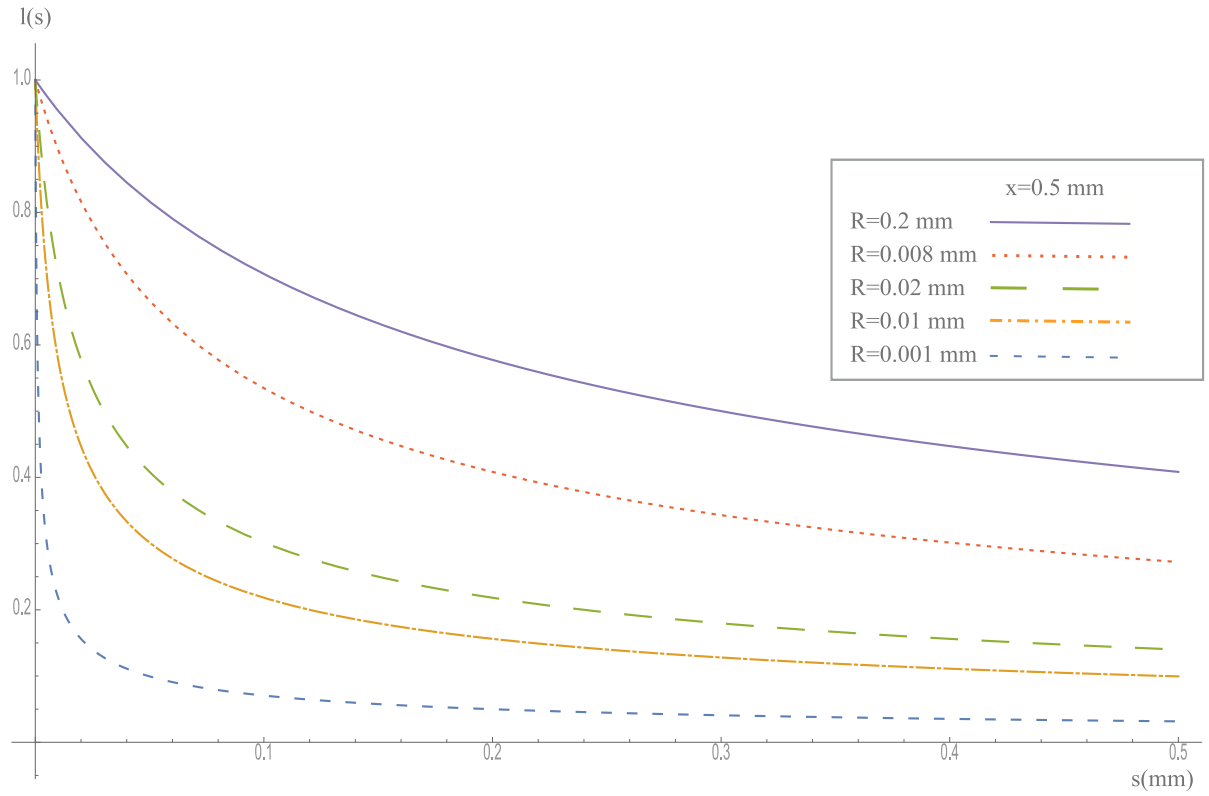

Figure 3.4: Plot of the PSF $l(s)$ of uniformly accelerated motion for with for 0.5 mm, and $R = 0.02$ mm.

$$k = \frac{v_o^2 \pi}{a} + 2\pi\, s\ ;\ dk = 2\pi ds$$

$$ds = \frac{dk}{2\pi}$$

Then, the limits of the integral are evaluated to obtain the new limits of integration. $x = 0 \rightarrow K_1 = \frac{v_o^2 \pi}{a}$ and $s = x \rightarrow K_2 = \frac{v_o^2 \pi}{a} + 2\pi x$ so $K_2 = K_1 + 2\pi x$.

$$L(u) = \frac{1}{2T\sqrt{a\pi}} \int_{K_1}^{K_2} \frac{e^{iuK_1} e^{-iuk}}{(k)^{1/2}} dk$$

$$L(u) = \frac{e^{iuK_1}}{2T\sqrt{a\pi}} \int_{K_1}^{K_2} \frac{e^{-iuk}}{(k)^{1/2}} dk$$

According to Euler's identity $e^{\pm i\theta} = \cos\theta \pm i \sin\theta$, then:

$$e^{-iuk} = \cos uk - i \sin uk$$

$$L(u) = \frac{e^{iuK_1}}{2T\sqrt{a\pi}} \int_{K_1}^{K_2} \frac{\cos uk - i \sin uk}{(k)^{1/2}} dk \tag{3.19}$$

$$L(u) = \frac{e^{iuK_1}}{2T\sqrt{a\pi}} \left(\int_{K_1}^{K_2} \frac{\cos uk}{(k)^{1/2}} dk - i \int_{K_1}^{K_2} \frac{\sin uk}{(k)^{1/2}} dk \right) \tag{3.20}$$

From the definition of Bessel functions:

$$\int_{K_1}^{K_2} \frac{\cos uk \, dk}{(k)^{1/2}} = (2\pi)^{1/2} \sum_{n=1}^{\infty} J_{2n+\frac{1}{2}}(uK_2) - J_{2n+\frac{1}{2}}(uK_1) \tag{3.21}$$

$$\int_{K_1}^{K_2} \frac{\sin uk \, dk}{(k)^{1/2}} = (2\pi)^{1/2} \sum_{n=1}^{\infty} J_{2n+1+\frac{1}{2}}(uK_2) - J_{2n+1+\frac{1}{2}}(uK_1) \tag{3.22}$$

Substituting Bessels functions shown in Eq.3.21 and Eq.3.22 into Eq.3.20:

$$L(u) = \frac{e^{iuK_1}\sqrt{2\pi}}{2T\sqrt{a\pi}} \left\{ \sum_{n=1}^{\infty} \left[J_{2n+\frac{1}{2}}(uK_2) - J_{2n+\frac{1}{2}}(uK_1) \right] - i \sum_{n=1}^{\infty} \left[J_{2n+1+\frac{1}{2}}(uK_2) - J_{2n+1+\frac{1}{2}}(uK_1) \right] \right\}$$

$$L(u) = \frac{e^{iuK_1}}{T\sqrt{2a}} \left\{ \sum_{n=1}^{\infty} \left[J_{2n+\frac{1}{2}}(uK_2) - J_{2n+\frac{1}{2}}(uK_1) \right] - i \sum_{n=1}^{\infty} \left[J_{2n+1+\frac{1}{2}}(uK_2) - J_{2n+1+\frac{1}{2}}(uK_1) \right] \right\}$$

$$L(u) = \frac{e^{iuK_1}}{T\sqrt{2a}} \left\{ \sum_{n=1}^{\infty} \left[J_{2n+\frac{1}{2}}(uK_2) - iJ_{2n+1+\frac{1}{2}}(uK_2) \right] - \sum_{n=1}^{\infty} \left[J_{2n+\frac{1}{2}}(uK_1) - iJ_{2n+1+\frac{1}{2}}(uK_1) \right] \right\}$$

$$L(u) = \frac{e^{iuK_1}}{\sqrt{2}} \left\{ \frac{1}{T} \left(\frac{1}{a} \right)^{1/2} \sum_{n=1}^{\infty} \left[J_{2n+\frac{1}{2}}(uK_2) - iJ_{2n+1+\frac{1}{2}}(uK_2) \right] \right\}$$

$$- \frac{e^{iuK_1}}{\sqrt{2}} \left\{ \frac{1}{T} \left(\frac{1}{a} \right)^{1/2} \sum_{n=1}^{\infty} \left[J_{2n+\frac{1}{2}}(uK_1) - iJ_{2n+1+\frac{1}{2}}(uK_1) \right] \right\}$$

Considering that:

$$j_N(x) = \sqrt{\frac{\pi}{2x}} J_{N+\frac{1}{2}}(x) \qquad ; \qquad J_{N+\frac{1}{2}}(x) = \sqrt{\frac{2x}{\pi}} j_N(x)$$

$$L(u) = \frac{e^{iuK_1}}{\sqrt{2}} \left\{ \frac{1}{T} \left(\frac{1}{a} \right)^{1/2} \sum_{n=1}^{\infty} \left[J_{\left(2n+\frac{1}{2}\right)}(uK_2) - iJ_{\left(2n+\frac{1}{2}\right)+1}(uK_2) \right] \right\}$$

$$-\frac{e^{iuK_1}}{\sqrt{2}}\left\{\frac{1}{T}\left(\frac{1}{a}\right)^{1/2}\sum_{n=1}^{\infty}\left[J_{\left(2n+\frac{1}{2}\right)}(uK_1)-iJ_{\left(2n+\frac{1}{2}\right)+1}(uK_1)\right]\right\} \tag{3.23}$$

For this case $N = 2n$:

$$j_{2n}(x)=\sqrt{\frac{\pi}{2x}}J_{2n+\frac{1}{2}}(x) \qquad ; \qquad J_{2n+\frac{1}{2}}(x)=\sqrt{\frac{2x}{\pi}}j_{2n}(x) \tag{3.24}$$

Substituting Eq.3.22 into 3.23 :

$$L(u)=\frac{e^{iuK_1}}{\sqrt{2}}\left\{\frac{1}{T}\left(\frac{2K_1}{\pi a}\right)^{1/2}\sum_{n=1}^{\infty}\left[j_{2n}(uK_2)-ij_{2n+1}(uK_2)\right]-\frac{1}{T}\left(\frac{2K_2}{\pi a}\right)^{1/2}\sum_{n=1}^{\infty}\left[j_{2n}(uK_1)-ij_{2n+1}(uK_1)\right]\right\}$$

$$L(u)=e^{iuK_1}\left\{\frac{1}{T}\left(\frac{K_1}{\pi a}\right)^{1/2}\sum_{n=1}^{\infty}\left[j_{2n}(uK_2)-ij_{2n+1}(uK_2)\right]-\frac{1}{T}\left(\frac{K_2}{\pi a}\right)^{1/2}\sum_{n=1}^{\infty}\left[j_{2n}(uK_1)-ij_{2n+1}(uK_1)\right]\right\}$$

Normalizing $u = 0$, $L(0) = 1$ for all x:

$$L(0)=\frac{1}{T}\left[\left(\frac{K_1}{\pi a}\right)^{1/2}-\frac{1}{T}\left(\frac{K_2}{\pi a}\right)^{1/2}\right]$$

$$L(u)=\frac{e^{iuK_1}}{L(0)}\left\{\frac{1}{T}\left(\frac{K_1}{\pi a}\right)^{1/2}\sum_{n=1}^{\infty}\left[j_{2n}(uK_2)-ij_{2n+1}(uK_2)\right]-\frac{1}{T}\left(\frac{K_2}{\pi a}\right)^{1/2}\sum_{n=1}^{\infty}\left[j_{2n}(uK_1)-ij_{2n+1}(uK_1)\right]\right\}$$

The function L(u) is complex, so it has a magnitude $M(u)$ and a phase $\theta(u)$:

$$M(u)=\frac{1}{L(0)}\left\{\frac{1}{T}\left(\frac{K_1}{\pi a}\right)^{1/2}\sum_{n=1}^{\infty}\left[j_{2n}(uK_2)-ij_{2n+1}(uK_2)\right]-\frac{1}{T}\left(\frac{K_2}{\pi a}\right)^{1/2}\sum_{n=1}^{\infty}\left[j_{2n}(uK_1)-ij_{2n+1}(uK_1)\right]\right\}$$

$$\theta(u)=e^{iuK_1}$$

Finally:

$$L(u)=\theta(u)M(u)$$

Evaluating once again the same values $x_1 = 0.05$ mm, $x_2 = 0.1$ mm, $x_3 = 0.5$ mm. It starts from $x_1 = 0.05$ mm , the following parameters are calculated:

$$R = 0.001 \text{ mm}, \qquad a = 1000 \text{ mm}/s^2, \qquad R=\frac{v_o^2}{a}$$

$$v_o^2 = R\,a = (0.001 \text{ mm})(1000 \text{ mm}/s^2) = 1 \text{ mm}^2/s^2, \qquad T = 0.5 \text{ s}$$

$$K_1 = \frac{v_o^2 \pi}{a} = \frac{1mm^2/s^2 \times \pi}{1000mm/s^2} = 0.0031415 \text{ mm}$$

$$= K_1 + 2\pi x = 0.0031415 \text{ mm} + 2\pi 0.05 \text{ mm} = 0.31730 \text{ mm}$$

$$L(0) = 0.180998$$

The same calculations are done for $R = (0.01, 0.02, 0.2, 0.008, 0.001)$ mm and $x_1 = 0.05$ mm, 0.1 mm, 0.5 mm. The results are shown in Fig.3.5, 3.6, 3.7, respectively.

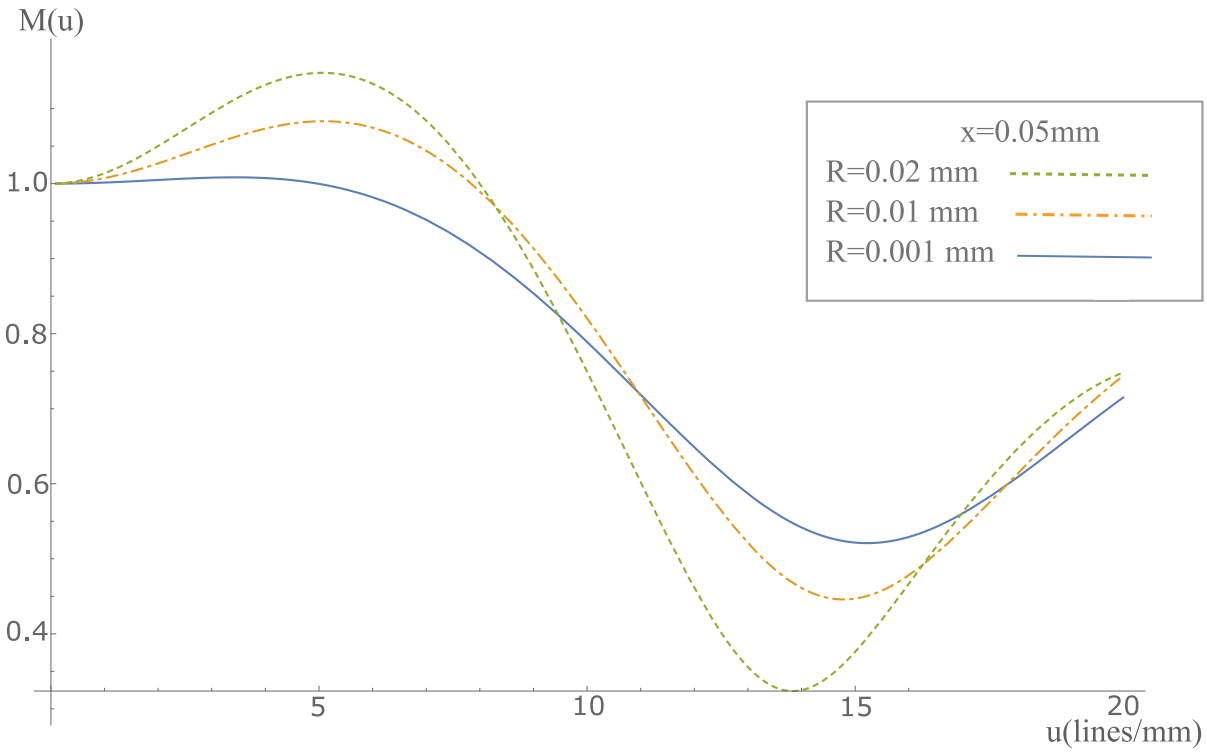

Figure 3.5: Plot of the PSF magnitude $M(u)$ for $x_1 = 0.05$ mm and $R = (0.01, 0.02, 0.2, 0.008, 0.001)$mm.

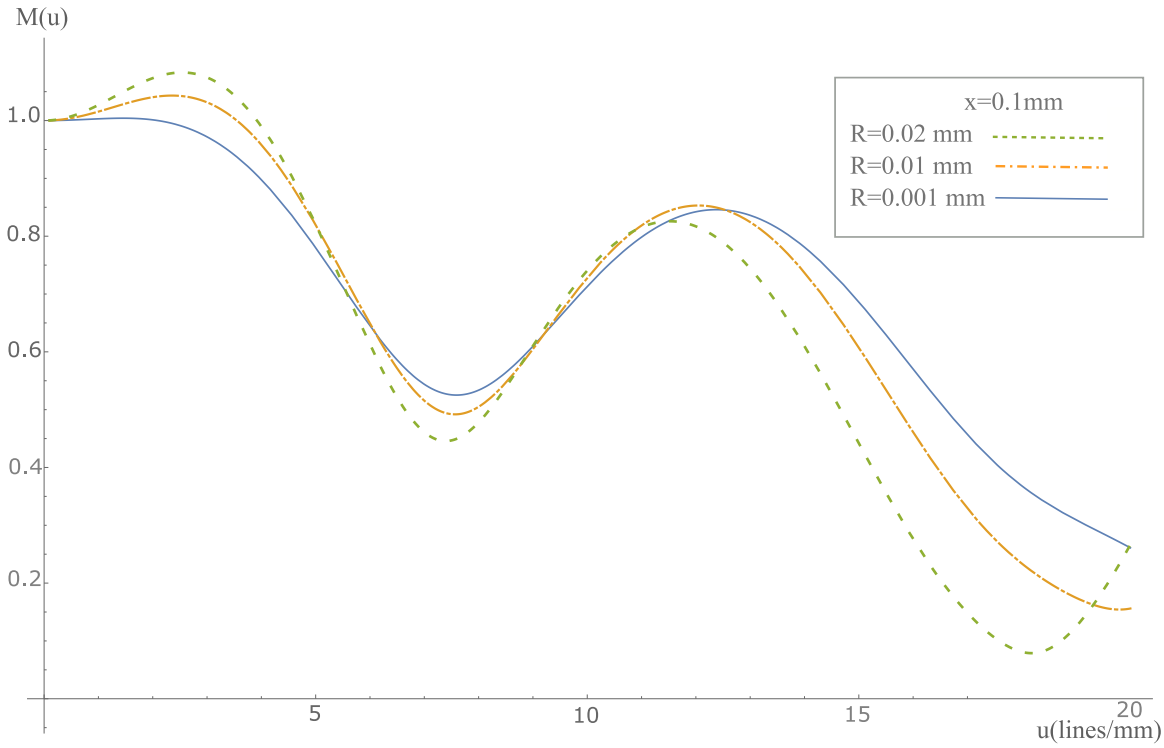

Figure 3.6: Plot of the PSF magnitude $M(u)$ for $x_1 = 0.1$ mm and $R = (0.01, 0.02, 0.2, 0.008, 0.001)$ mm.

3.2 MOTION BLUR MODELING USING CT

A new method is proposed to model the blur with uniform velocity and acceleration, using the Cosine Transform, without neglecting that Fourier transform method has been extensively studied. The proposed alternative method, based on Cosine Transform, has some advantages when compared to classic Fourier Transform. These will be discussed in the further applications on this thesis.

$$P(\omega) = \int_{-\infty}^{\infty} f(x) e^{-i\omega x} dx$$

$$e^{i\theta} = \cos(\theta) + i\sin(\theta)$$

$$P(\omega) = \int_{-\infty}^{\infty} f(x) \left(\cos(\omega x) - i\sin(\omega x)\right) dx$$

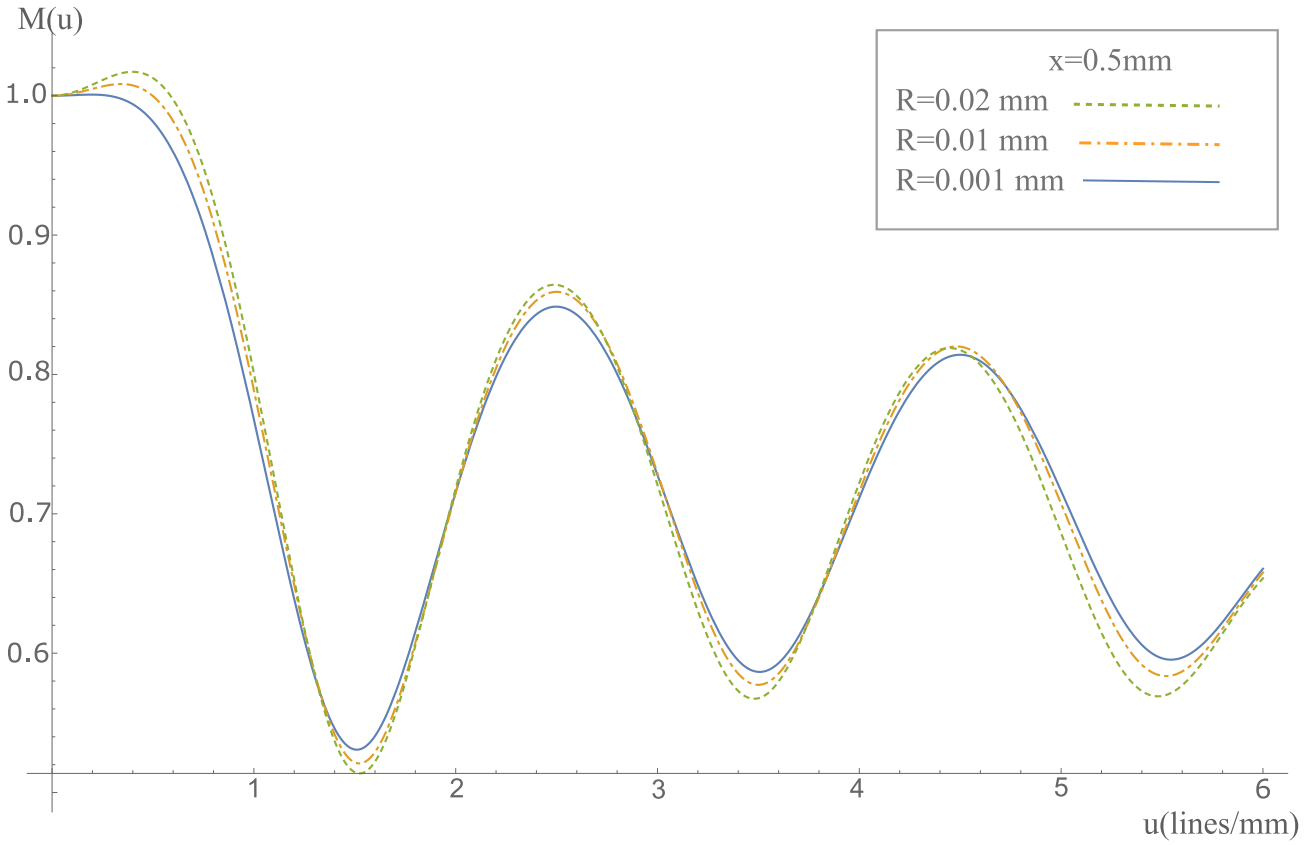

Figure 3.7: Plot of the PSF magnitude $M(u)$ for $x_1 = 0.5$ mm and $R = (0.01, 0.02, 0.2, 0.008, 0.001)$ mm.

$$P(\omega) = \int_{-\infty}^{\infty} f(x)\cos(\omega x)dx - i\int_{-\infty}^{\infty} f(x)\sin(\omega x)dx$$

$$P_1(\omega) = \int_{-\infty}^{\infty} f(x)\cos(\omega x)dx$$

$$P_2(\omega) = -i\int_{-\infty}^{\infty} f(x)\sin(\omega x)dx$$

For this study only $P_1(\omega)$ is used. It is considered the Continuous Cosine Transform as shown in Eq.3.25:

$$F(\omega) = \int_{-\infty}^{\infty} f(x)\cos(\omega x)dx \tag{3.25}$$

3.2.1 Uniform Velocity

For the case of speed $f(x) = b$ is a constant, which is replaced in (3.25):

$$F(\omega) = \int_0^L b\cos(\omega x)dx \tag{3.26}$$

Solving the integral:

$$F(\omega) = \left[\frac{b}{\omega}\sin(\omega x)\right]_0^L \tag{3.27}$$

Evaluating the integral:

$$F(\omega) = \frac{b}{\omega}\sin(\omega L) \tag{3.28}$$

All the equation is multiplied and divided by L:

$$F(\omega) = \frac{Lb}{L\omega}\sin(\omega L) \tag{3.29}$$

Replacing $\varpi = \omega L$:

$$F(\omega) = Lb\frac{\sin(\varpi)}{\varpi} \tag{3.30}$$

Finally:

$$F(\omega) = Lb\,\mathrm{sinc}(\omega L) \tag{3.31}$$

Figure 3.8 depicts a Plot curve of $F(\omega)$ using $L = 0.5$ mm and $b = 1$ mm/s.

3.2.2 Uniform acceleration

The PSF for the case of acceleration is given by $f(x) = \left(\frac{1}{\sqrt{v^2+2ax}}\right)$, Which is replaced in (3.25):

$$F(\omega) = \int_0^L \frac{\cos(\omega x)}{\sqrt{v^2+2ax}}dx \tag{3.32}$$

Substituting u:

$$u = \sqrt{2ax + v^2} \tag{3.33}$$

$$\frac{du}{dx} = \frac{a}{\sqrt{2ax+v^2}} \tag{3.34}$$

x is obtained from Eq.3.33 by squaring both sides:

$$x = \frac{u^2 - v^2}{2a} \tag{3.35}$$

Substituting Eq.3.33, 3.34, and 3.35 into Eq.3.32:

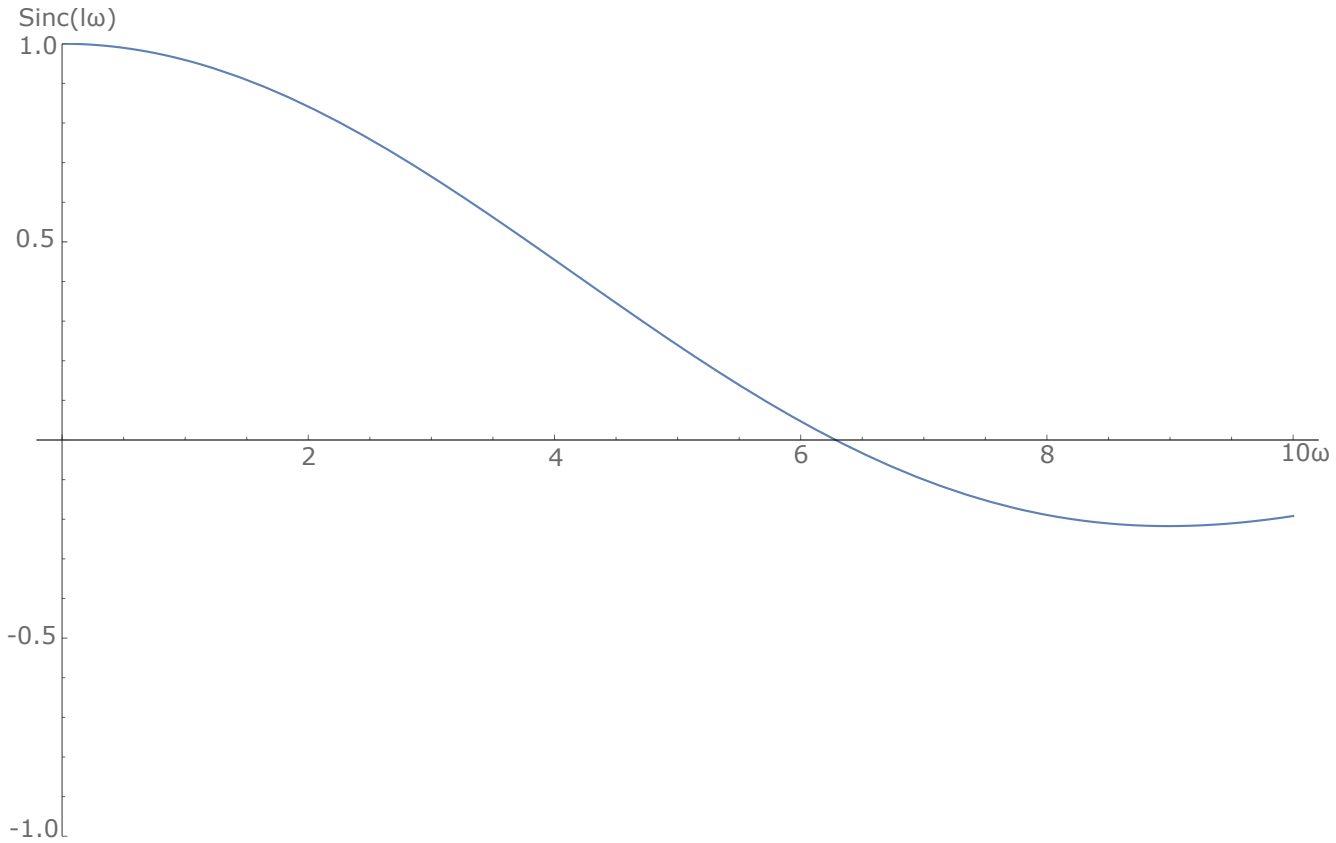

Figure 3.8: function $F(\omega)$ using $L = 0.5$ mm and uniform velocity $b = 1$mm/s

$$\int_0^L \cos\left[\omega\left(\frac{u^2 - v^2}{2a}\right)\right] du \tag{3.36}$$

Using the double angle identity:

$$\cos(\alpha - \beta) = \cos\alpha\cos\beta + \sin\alpha\sin\beta$$

Hence:

$$\int_0^L \cos\left(\frac{\omega u^2 - \omega v^2}{2a}\right) du = \int_0^L \cos\left(\frac{\omega u^2}{2a} - \frac{\omega v^2}{2a}\right) du =$$

$$\int_0^L \left(\sin\left(\frac{\omega v^2}{2a}\right)\sin\left(\frac{\omega u^2}{2a}\right) + \cos\left(\frac{\omega v^2}{2a}\right)\cos\left(\frac{\omega u^2}{2a}\right)\right) du \tag{3.37}$$

Reorganizing:

$$\sin\left(\frac{\omega v^2}{2a}\right)\int_0^L \sin\left(\frac{\omega u^2}{2a}\right) du + \cos\left(\frac{\omega v^2}{2a}\right)\int_0^L \cos\left(\frac{\omega u^2}{2a}\right) du \tag{3.38}$$

Solving the first integral from Eq.3.38:

$$\int_0^L \sin\left(\frac{\omega u^2}{2a}\right) du \tag{3.39}$$

Now, multiplying and dividing the cosine argument by π:

$$\int_0^L \sin\left(\frac{\omega u^2}{2a}\frac{\pi}{\pi}\right) du \tag{3.40}$$

Let:

$$y^2 = \left(\frac{\omega u^2}{\pi a}\right) \tag{3.41}$$

$$y = \sqrt{\frac{\omega}{\pi a}}u \tag{3.42}$$

$$\frac{dy}{du} = \sqrt{\frac{\omega}{\pi a}} \tag{3.43}$$

Then, replacing Eq.3.42) and 3.43 into Eq.3.40:

$$\sqrt{\frac{\omega}{\pi a}}\int_0^L \sin\left(\frac{\pi y^2}{2}\right) dy \tag{3.44}$$

Equation 3.44 is similar to Fresnel integrals definition:

$$S(y) = \int_0^L \sin\left(\frac{\pi y^2}{2}\right) dy \tag{3.45}$$

$$C(y) = \int_0^L \cos\left(\frac{\pi y^2}{2}\right) dy \tag{3.46}$$

These are known as the integrals of Fresnel $S(y)$ and $C(y)$ respectively. Using Eq.3.45 in Eq.3.44:

$$\sqrt{\frac{\omega}{\pi a}}S(y) \tag{3.47}$$

Substituting y from Eq.3.42:

$$\sqrt{\frac{\omega}{\pi a}}S\left(\sqrt{\frac{\omega}{\pi a}}u\right) \tag{3.48}$$

Now, repeating the same procedure with the second integral in Eq.3.38:

$$\int_0^L \cos\left(\frac{\omega u^2}{2a}\right) du \tag{3.49}$$

Multiplying and dividing the cosine argument by π:

$$\int_0^L \cos\left(\frac{\omega u^2}{2a}\frac{\pi}{\pi}\right) du \tag{3.50}$$

Then, substituting Eq.3.42 and Eq.3.43 in Eq.3.50:

$$\sqrt{\frac{\omega}{\pi a}}\int_0^L \cos\left(\frac{\pi y^2}{2}\right) dy \tag{3.51}$$

Eq.3.51 is also similar to $C(y)$ shown in Eq.3.46, therefore Eq.3.51 can be rewritten as shown in Eq.3.52:

$$\sqrt{\frac{\omega}{\pi a}}C(y) \tag{3.52}$$

Once again, y can be obtained from Eq.3.42:

$$\sqrt{\frac{\omega}{\pi a}}C\left(\sqrt{\frac{\omega}{\pi a}}u\right) \tag{3.53}$$

Substituting Eq.3.48, and Eq.3.53 in Eq.3.38:

$$F(\omega) = \left[\sqrt{\frac{\omega}{\pi a}}\sin\left(\frac{\omega v^2}{2a}\right) S\left(\sqrt{\frac{\omega}{\pi a}}u\right) + \sqrt{\frac{\omega}{\pi a}}\cos\left(\frac{\omega v^2}{2a}\right) C\left(\sqrt{\frac{\omega}{\pi a}}u\right)\right]_0^L \tag{3.54}$$

and u from Eq.3.33:

$$F(\omega) = \left\{\sqrt{\frac{\omega}{\pi a}}\sin\left(\frac{\omega v^2}{2a}\right) S\left[\sqrt{\left(\frac{\omega}{\pi a}\right)(2ax+v^2)}\right] + \sqrt{\frac{\omega}{\pi a}}\cos\left(\frac{\omega v^2}{2a}\right) C\left[\sqrt{\left(\frac{\omega}{\pi a}\right)(2ax+v^2)}\right]\right\}_0^L \tag{3.55}$$

Finally, Evaluating the solution integral:

$$F(\omega) = \left\{\sqrt{\frac{\omega}{\pi a}}\sin\left(\frac{\omega v^2}{2a}\right) S\left\{\sqrt{\left(\frac{\omega}{\pi a}\right)(2aL+v^2)}\right\} + \sqrt{\frac{\omega}{\pi a}}\cos\left(\frac{\omega v^2}{2a}\right) C\left[\sqrt{\left(\frac{\omega}{\pi a}\right)(2aL+v^2)}\right]\right\} -$$

$$\left\{\sqrt{\frac{\omega}{\pi a}}\sin\left(\frac{\omega v^2}{2a}\right) S\left[\sqrt{\left(\frac{\omega}{\pi a}\right)(v^2)}\right] + \sqrt{\frac{\omega}{\pi a}}\cos\left(\frac{\omega v^2}{2a}\right) C\left[\sqrt{\left(\frac{\omega}{\pi a}\right)(v^2)}\right]\right\} \tag{3.56}$$

The plot solutions shown in Fig.3.9 are at $a = 1000\,\mathrm{mm}/s^2$, $a = 100\,\mathrm{mm}/s^2$, $a = 50\,\mathrm{mm}/s^2$, initial speed $v = 1$ m/s, and $x = 0.5\,\mathrm{mm}$ respectively.

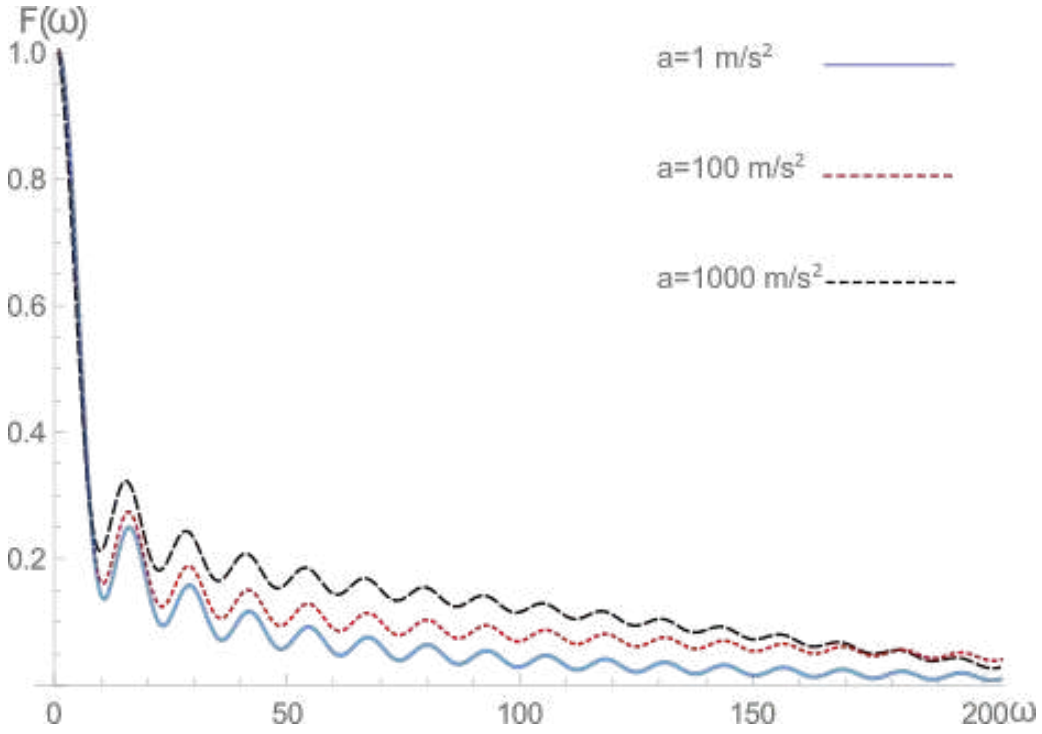

Figure 3.9: Function $F(\omega)$ with x=0.5 mm, $v_0 = 1$ mm/s and uniform acceleration $a = 1000\,\mathrm{mm}/s^2$, $a = 100\,\mathrm{mm}/s^2$., and $a = 50\,\mathrm{mm}/s^2$.

3.3 CONCLUSIONS

As presented in this chapter, it is possible to model linear motion blur using the Discrete Cosine Transform obtaining similar results. The alternative proposal introduces some advantages that are widely discussed in this thesis based on experiments performed on synthetic and actual images. Additionally, CT modeling is more straightforward because it does not use complex numbers.

Chapter 4

ESTIMATION OF THE PSF PARAMETERS

111

This chapter presents an alternative approach of Discrete Cosine Transform (DCT) for the estimation of the angle and length parameters of the Point Spread Function (PSF) in motion blur images. Motion degradation is a frequent issue in surveillance, traffic-camera ticket, and robotics systems. Its parameters can help image restoration and, besides, to calculate motion direction and relative speed of an object. Our technique addresses the case of spatially invariant uniform linear motion blur occurrences when the camera moves at constant velocity, and the background does not change. Several algorithms have been introduced to estimate the parameters of the PSF, but they fail when using noisy images. Twenty test images were synthetically degraded with motion blur and Additive White Gaussian Noise (AWGN) to be used for both angle and length estimation in these experiments. The proposed DCT Radon approach to the Point spread Function parameters estimation of invariant uniform linear motion blurred images has shown to be a suitable alternative for its reconstruction even in the presence of Gaussian noise in a signal-to-noise ratio ranging between 20dB and 36dB. Its mean absolute error for angle estimation was 0.66° degrees and 7.78° degrees for noise-free and noisy images, respectively. Similarly, our DCT Pseudo Cepstrum had the lowest mean error of 0.99 pixels and 7.78 pixels for noise-free and noisy images, respectively.

4.1 INTRODUCTION

Blur in digital images can be produced by the relative motion between the camera and the observed scene by an optical system out of focus during image formation or by optical turbulence added by a particle-loaded or turbulent atmosphere, among others. Said phenomena cause a reduction of high-frequency contents in the images, perceivable in the direction of the distortion. Blur is not unique to the formation of optical images since it is also present in data coming from electronic microscopes (due to spherical electronic lens aberrations), corrupt CT scanners, and X-rays affected by forced scattering in the medium [Bovik(2009), Bovik(2010)].

As mention earlier, blur can be classified, according to its nature, in three categories: optical, mechanic, and medium induction blur [Gunturk and Li(2012)]. This chapter only considers mechanic blur, which occurs when the relative velocity between different objects in the scene and the camera are significant, in comparison to the exposure time, and blur is invariant at every

spatial location, resulting in a motion-blurred image [Lin and Li(2004a), Šorel et al.(2009)Šorel, Šroubek, and Flusser].

Motion blur can be classified into two types, depending on its distribution in the degraded image: spatially invariant blur, in which the distortion degrades the image uniformly; and spatially variant blur, characterized by different blurring levels in the same image. The first type is produced by either mechanical vibration or handshaking during image formation, which results in a uniformly blurred image. When the camera stays still in a 3D scene, induced motion blur is typically not uniform, as it captures objects moving at different speeds and in different directions on the image plane [Pretto et al.(2009)Pretto, Menegatti, Bennewitz, Burgard, and Pagello, Chan and Shen(2005b), Potmesil and Chakravarty(1983)].

Though this chapter does not deal with kinematic quantities estimation, such as motion direction and relative speed at a constant rate of a moving object using a single linear motion blur image, it results in helping to calculate them [Lin and Li(2004a), Celestino and Horikawa(2008), Kawamura et al.(2002)Kawamura, Kondo, Konishi, and Ishlgakl, Xu and Zhao(2010), Rezvankhah et al.(2012)Rezvankhah, Bagherzadeh, Moradi, and Member].

In the present chapter of this research thesis, we focus on computing the main parameters of linear motion blur, namely length and angle. These parameters can be used to estimate kinematic quantities related to the movement that causes distortion [Pretto et al.(2009)Pretto, Menegatti, Bennewitz, Burgard, and Pagello, Zhang and Hirakawa(2015)]. The proposed blind approach is much more challenging, as the PSF and its non-degraded image are unknown. Blind deconvolution of motion blur images is a practical and helpful research area in a variety of disciplines, including, but not limited to, image processing, computer vision, physics, astronomy, and medical imaging [Rajagopalan and Chellappa(2014)].

4.2 LINEAR MOTION BLUR

This occurs when there is relative motion between the camera and the object being captured. If we can identify the angle θ with respect to the camera and the length L of the blur, the PSF can be reconstructed. When the camera moves over a certain distance L during exposure time T, every point in the captured image frame is mapped onto several pixels of the resulting degraded image, producing a photograph that is blurred along the direction of motion [Brusius et al.(2011)Brusius, Schwanecke, and Barth]. Fig. 4.1(b) shows length and angle of the linear motion blur kernel $h(x, y)$.

PSF length L equals the distance that one pixel is moved by the motion, and its angle θ is the direction of motion with respect to the x-axis. Equation 4.1 is derived from Eq.1.4 and models the space invariant motion blur where $I(x, y)$ is the non-degraded original image, $h(x, y)$ is the blurring Point Spread Function, $n(x, y)$ is usually Gaussian white noise, and $g(x, y)$ is the degraded image.

$$g(x, y) = I(x, y) * h(x, y) + n(x, y) \tag{4.1}$$

Finding the blur kernel angle and length allows for the reconstruction of the image prior to degradation. With the proper estimated PSF, an undistorted image can be obtained using the inverse Fourier Transform, in a process which is called Inverse Filtering. This is possible under ideal conditions, but more difficult to attain in actual images due to the presence of additive noise, which permeates the result in inverse filtering [Brusius et al.(2011)Brusius, Schwanecke, and Barth].

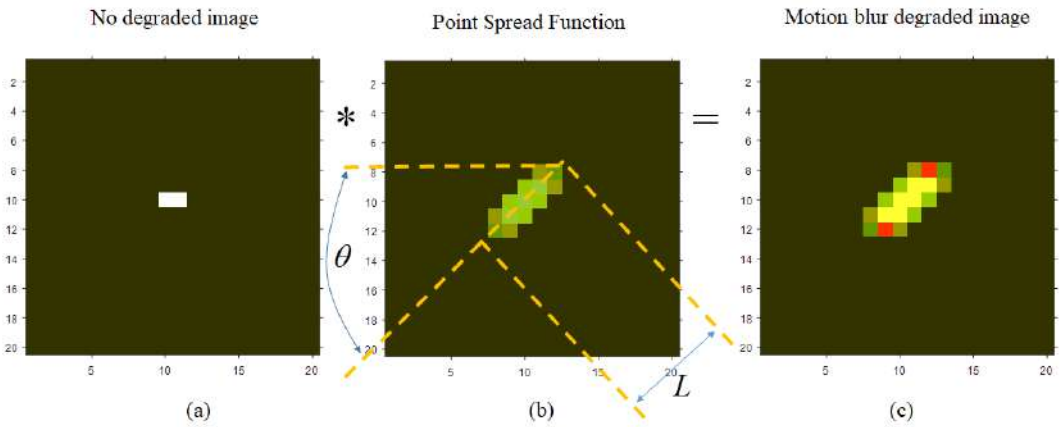

Figure 4.1: Convolution steps. (a) Two pixels no degraded image. (b) Point Spread Function and (c) Motion blur degraded image.

$$h(x,y) = \begin{cases} \frac{1}{L} & 0 \leq x \leq L\cos\theta\,;\; y = L\sin\theta \\ 0 & \text{otherwise} \end{cases} \tag{4.2}$$

If we assume that motion is along the x-axis, that is to say $\theta = 0$, then Eq.4.2 can be simplified and expressed, as seen in Eq.4.3:

$$h(x,y) = \begin{cases} \frac{1}{L} & 0 \leq x \leq L\,;\; y = 0 \\ 0 & \text{otherwise} \end{cases} \tag{4.3}$$

Figure 4.1 illustrates the convolution process of a non-degraded image (two pixels) with a linear motion blur kernel (with a length of 4 and a 45° degrees angle).

4.2.1 Strategies to estimate length and angle

There are three common strategies used to estimate the angle and its blur length: space, frequency and wavelet domain approaches. Space and frequency have been widely studied for the reconstruction of PSF and, after that, for deconvolution. Although there are some investigations regarding wavelet domain, most of them do not allow for the estimation of PSF parameters, but instead for the location of blur in space in an image [Chan and Shen(2005a), Lu(2006), Zhang and Hirakawa(2015)]. Zhang and Hirakawa (University of Dayton, 2013) reconstruct kernel to find a non-degraded image in the Wavelet domain [Zhang and Hirakawa(2013b), Zhang and Hirakawa(2015)]. Guo, Wang and Liu (Chongqing University, China, 2013) presented a method to identify the PSF of a motion blurred image, based on two-dimensional discrete Wavelet Transform (2D-DWT) and Cepstrum. The key idea was to estimate blur length and blur direction by employing 2D-DWT on a motion blurred image, then detecting the decomposed image with Cepstrum analysis [GUO et al.(2013)GUO, WANG, and LIU].

Space Domain Approaches for Angle Estimation

Yitzhaky, Mor, Lanzman, and Kopeika (University of Negev, Israel, 1998) proposed a space domain method to estimate the motion blur angle. They used, in their approach, a tangential

directional derivative kernel. This had to be convoluted with the motion blurred image at angles between 0° and 90° degrees to estimate its response at each angle. The motion direction was then the direction in which the total energy response was the lowest. Unfortunately, their method fails when the angle is bigger than 45° degrees [Yitzhaky and Kopeika(1997), Yitzhaky et al.(1998)Yitzhaky, Mor, Lantzman, and Kopeika]. The Szabo and Shibata Group's proposal (University of Tokyo, Japan, 2009) is based on edge detection and count. Blurred images have little high-frequency content, so edges are dismissed somehow, and only motion blur lines are kept. The motion blur angle is found by rotating the image to different angles and applying an edge detector. The angle with the highest difference in edge count is determined and considered to be the angle at which shifting occurred [Grou-Szabo and Shibata(2009b)]. Phansalkar (College of Engineering, India, 2010) presented one of the simplest methods, which assumes a spatially invariant linear blur over the entire image, and uses the Hough Transform in space. The entire image is gridded into smaller parts of the same image, and the Hough Transform is applied to each resulting rectangle. The motion blur length and angle are statistically estimated from the set of collected data on each grid. The author indicates that these algorithms are not completely automatic and require user interaction [Phansalkar(2010a)]. Chen et al. (Shanghai Jiao Tong University, China, and University of Technology, Australia, 2010) stated in their publication that high-frequency energy decreases significantly along motion direction in a blurred image, so the motion direction angle can be estimated by detecting the lowest directional high-frequency energy, where energy is regarded as the sum of the squared image derivative. They conclude by stating that their proposed method can produce more accurate results with less computation [Chen et al.(2010)Chen, Yang, Wu, and Zhao].

Frequency Domain Approaches for Angle Estimation

Rekleitis (University St, Canada, 1996) proposed the application of a family of steerable filters such as Gaussian and Gabor on the power spectrum image log, and evaluate the highest response angle, but they have a large amount of error in angle detection, even with no noise [Rekleitis(1996), Krahmer et al.(2006)Krahmer, Lin, McAdoo, Ott, Wang, Widemann, and Wohlberg]. Tiwari, Shukla and Singh (Institute of Technology, India, 2013) explained in their review that blur direction can be identified using the Hough Transform to detect the position of a line in the log magnitude spectrum of the blurred image. Dark lines in the Fourier Frequency Domain are related to the motion blur angle [Tiwari et al.(2014)Tiwari, Singh, and Shukla, Lokhande et al.(2006)Lokhande, Arya, and Gupta, Su et al.(2012)Su, Lu, and Lim, Moghaddam and Jamzad(2004), Dobeš et al.(2010)Dobeš, Machala, and Fürst]. Mughaddam and Jamzad (University of Technology, Iran, 2004) also reviewed an alternative technique to estimate motion blur angle to overcome Hough Transform issues. Radon Transform can be applied to the Fourier Spectrum, without needing to convert the image to binary format, as required by the Hough methods. This makes the approach easier and faster to implement [Krahmer et al.(2006)Krahmer, Lin, McAdoo, Ott, Wang, Widemann, and Wohlberg, Tiwari et al.(2014)Tiwari, Singh, and Shukla, Dobeš et al.(2010)Dobeš, Machala, and Fürst, Jia and Wen(2013), Pazhoumand-Dar et al.(2010)Pazhoumand-Dar, Abolhassani, and Saeedi]. Ji and Liu (National University of Singapore, Singapore, 2008) introduced a hybrid Fourier-Radon Transform to estimate the parameters of the blurring kernel with improved robustness to noise [Ji and Liu(2008)]. Krahmer, Lin, McAdoo, Ott, Wang and Widemann (Los Alamos National Laboratory, USA, 2014) stated that if the noise level of the blurred image is not too high, there are two pronounced peaks in the Cepstrum of the one dimension (1D)

collapsed power spectrum from the motion blurred image. To estimate the angle of motion blur, they proposed drawing a straight line from the origin to the first negative peak. The Cepstral method breaks down in the presence of noise [Krahmer et al.(2006)Krahmer, Lin, McAdoo, Ott, Wang, Widemann, and Wohlberg]. The angle of motion blur is approximated using the inverse tangent of the slope of this line in the Cepstral plot [Krahmer et al.(2006)Krahmer, Lin, McAdoo, Ott, Wang, Widemann, and Wohlberg]. This is a technique that has been widely used in signal processing [Tiwari et al.(2014)Tiwari, Singh, and Shukla, Ji and Liu(2008), Qi et al.(2005)Qi, Zhang, and Tan, Tiwari and Shukla(2013), Schuon and Diepold(2009)].

Space Domain Approaches for Length Estimation

Phansalkar (College of Engineering, India, 2010) stated that once the motion blur angle has been calculated, the motion blur length can be estimated. The Hough Transform is applied to the entire gridded image edge, and all the lines with length above a certain threshold at a certain angle are averaged, to obtain the right length [Phansalkar(2010b)]. Grou-Szabo and Shibata (University of Tokyo, Japan, 2009) presented a technique, based on the iterative restoration process. An edge detector is swept over the convoluted image until wave-patterns on the image are dissolved. The precise length is estimated, when these periodic patterns are vanished [Grou-Szabo and Shibata(2009a)]. Yang, Liu, and Liu (Guizhou University, China, 2011) expressed that motion blur length can be estimated by measuring the ringing artifact amount of a deblurred image. Ringing artifacts are ripples that appear near strong edges. The correct motion blur length causes minimal ringing artifacts on the image, so the main ringing artifacts can be obtained by using a high-pass filter response [Yang et al.(2011)Yang, Liu, Liu, and Liao]. There are also several machine learning techniques to estimate the PSF parameters n the scientific literature, but they consider that some training samples are needed, as shown in [Grou-Szabo and Shibata(2009b), Aizenberg et al.(2000)Aizenberg, Aizenberg, Butakov, and Farberov], and [Cannon(1976)] which used Neural Networks and and Support Vector Regression, respectively.

Frequency Domain for Length Estimation

Cannon (University of Utah, USA, 1974) stated in his investigation that zeroes of $G(u, v)$ are related to the zeroes of $I(u, v)$ and $H(u, v)$; therefore, if we have a parametric form of the Point Spread Function, the parametric values can be found [Cannon(1976)]. This is done by looking for the zero crossing of the blur system frequency response. Motion blur has its zeroes along lines perpendicular to the direction of the blur and are separated from each other at a regular interval $1/L$. This technique has low computational complexity, and is reliable, but fails when SNR is low [Kundur and Hatzinakos(1996), Dash(2012)]. Yoshida, Horiike and Fujita (Department of Electronics and information Science Japan,1993) used the DCT to estimate motion blur length, and radius of out-of -focus blur, but their length estimation procedure was completely manual, using the DCT plotted curve of the collapsed DCT spectrum. They stated that the DCT approach was better than DFT [Yoshida et al.(1993)Yoshida, Horiike, and Fujita]. Yitzhaky, Mor, Lanzman, and Kopeika (University of Negev, Israel, 1998) considered that the spectral domain zeros technique was not suitable for accelerated motion degradation or low frequency vibrations [Yitzhaky et al.(1998)Yitzhaky, Mor, Lantzman, and Kopeika]. The Moghaddam and Jamzad algorithm (Sharif University of Technology, Iran, 2006) is based on the central peaks and valleys in the Fourier spectrum collapsed pattern. To find motion length, they used

the parallel dark lines that appear in the Fourier spectrum of the degraded image. All valleys are candidates for dark line places, but some of them may be false. The best ones are valleys that correspond to the SINC function in the Fourier spectrum. These valleys are on both sides of the central peak [Moghaddam and Jamzad(2007)] (Also review [Dobeš et al.(2010)Dobeš, Machala, and Fürst] from Dobes, Machala and Furst, 2010). Sakano, Suetake, and Uchino's algorithm (Yamaguchi University, Yamaguchi, Japan, 2006) [Sakano et al.(2006)Sakano, Suetake, and Uchino] found the dark lines in the Fourier spectrum pattern, using a modified version of the Hough Transform, concerning gradient vectors, which can accurately and robustly estimate the motion blur PSF even in highly noisy cases.

Blind Deconvolution

Blind deconvolution is the restoration of a fine copy of a blurred picture when the kernel is untold or partially known. It needs an initial hypothetical estimation, or it can not withdraw a suitable deblur solution. This iterative approach, for the reconstruction of motion blur images, was considered as a possible solution to realize the PSF. The algorithm converged to a solution in a proof of concept test carried out in the laboratory. Its response was far from the actual PSF in terms of angle and length. However, the deblurred image was accurate [Levin et al.(2011)Levin, Weiss, Durand, and Freeman, Perrone and Favaro(2016), Lam and Goodman(2000)].

4.2.2 Motion Blur Length Estimation using Continuous Cosine Transform

The mathematical framework that supports DCT approach to the estimation of blur length is introduced in 3.2. That section explains widely both cases for constant velocity and acceleration. It is highly recommended to review the full chapter 3 if needed further details.

Uniform motion blur can be modeled as an even Gate function of amplitude b and length L as seen in Fig.4.2 and Eq.4.4.

$$f(x) = \begin{cases} b & -\frac{L}{2} \leq x \leq \frac{L}{2} \\ 0 & \text{otherwise} \end{cases} \tag{4.4}$$

Introducing the Continuous Cosine Transform in Eq. 4.5:

$$\int_{-\infty}^{+\infty} f(x)\cos(\omega x)dx \tag{4.5}$$

solving this integral for the Gate function in Fig.4.3:

$$F_c(\omega) = 2\int_{0}^{\frac{L}{2}} f(x)\cos(\omega x)dx$$

$$F_c(\omega) = \frac{2b}{\omega}\sin\left(\frac{\omega L}{2}\right)$$

Finally, we obtain Eq. 4.6:

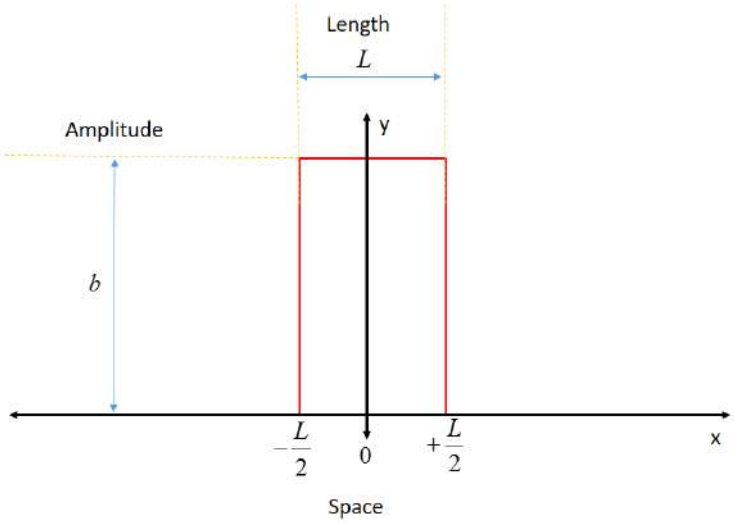

Figure 4.2: Motion blur Gate model. L represents the length of the blur in the image during the exposure time T.

$$F_c(\omega) = \left(\frac{\omega L}{2}\right) \frac{2b}{\omega} \frac{\sin\left(\frac{\omega L}{2}\right)}{\frac{\omega L}{2}}$$

$$F_c(\omega) = bL\text{sinc}\left(\frac{\omega L}{2}\right) \tag{4.6}$$

If it is necessary to find motion blur length L, it is possible to do so from the cosine spectrum, using the valley points where the sinc function is zero:

$$bL\text{sinc}\left(\frac{\omega L}{2}\right) = 0$$

Therefore, motion blur length L can be calculated with Eq.4.7 :

$$L = \frac{2\pi n}{\omega_n} \tag{4.7}$$

Where $n = 1, 2, 3, ...$
Figure 4.3 plots the regular curve of the Power Spectrum of Cosine Transform.

4.2.3 Motion Blur Angle Estimation using Continuous Cosine Transform

DFT spectrum of a motion blurred image has an anisotropic nature due to the predominant presence of motion lines in space. Besides, the spectrum is oriented in a direction perpendicular to the motion. It allows for the discovery of the motion blur angle just by estimating the relative position of either the dark or bright zones of the rippling pattern (See Fig.4.4), but this needs to be windowed to soften the rapid change in the image's edges, which produce undesired brighter lines along the center of the power spectrum pattern.

On the other hand, the DCT power spectrum is also positioned perpendicular to the motion, so its energy is more concentrated in the left upper corner (See Fig.4.5).

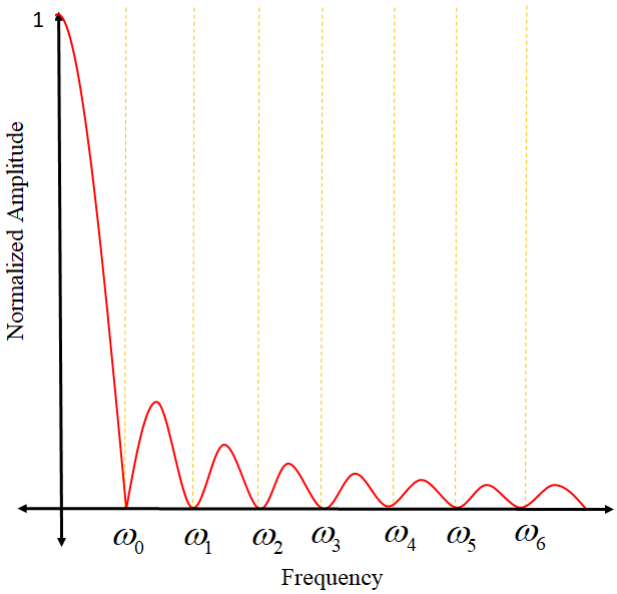

Figure 4.3: Power Spectrum of Continuous Cosine Transform for The Gate Function.

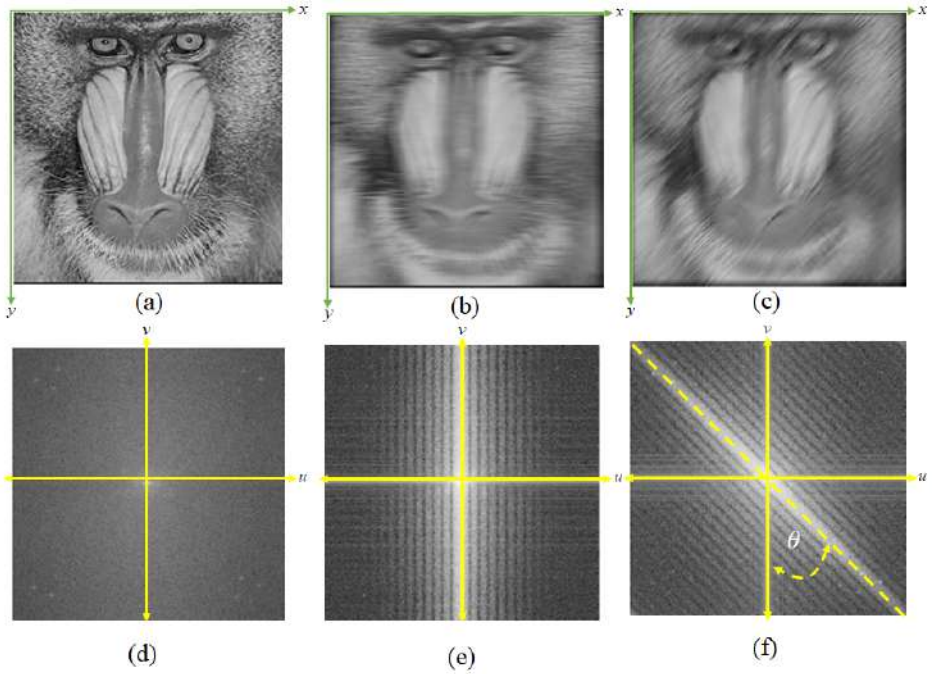

Figure 4.4: Angle estimation of Baboon image at several motion blur angles. (a) Non-blurred Baboon image. - (b) Motion blurred Baboon image at 0^{o} degrees. - (c) Motion blurred Baboon image at 45^{o} degrees. - (d) DFT Power spectrum of image (a). - (e) DFT Power spectrum of image (b). - (f) DFT Power spectrum of image (c). This images has not been windowed.

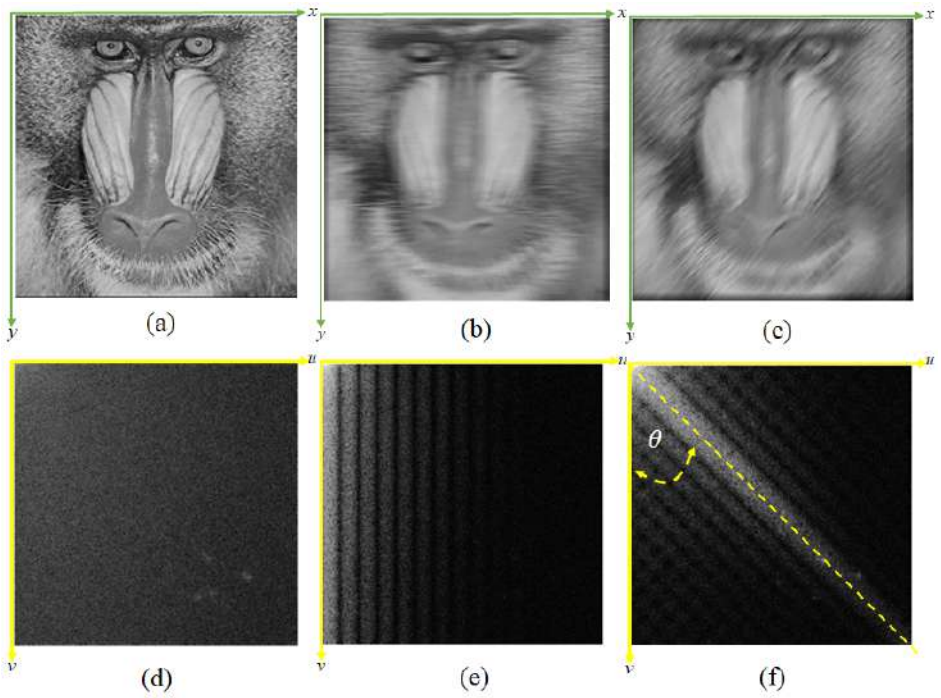

Figure 4.5: Angle estimation of Baboon image at several motion blur angles. (a) Non-blurred Baboon image. - (b) Motion blurred Baboon image at 0^{o} degrees. - (c) Motion blurred Baboon image at 45^{o} degrees. - (d) DCT Power spectrum of image (a). - (e) DCT Power spectrum of image (b). - (f) DCT Power spectrum of image (c).

4.3 DISCRETE COSINE TRANSFORM PROPOSAL

4.3.1 The Discrete Cosine Transform

One of the main advantages of 2D DCT is its removal property of redundancy between neighboring pixels, called decorrelation characteristic, which leads to superior energy compaction in just a few coefficients for highly correlated images. Usually, neighbor pixels are correlated, if surfaces are smooth. Even though DCT algorithms can have slightly longer run-times, today several fast algorithms are being developed, that use only real arithmetic. These have helped reduce hardware implementations dramatically. Moreover, the DCT divides all frequencies of the signal by two, due to this, they are more densely distributed than in the DFT spectrum causing a double frequency resolution in the DCT spectrum [Burger et al.(2009)Burger, Burge, Burge, and Burge]. Equation 4.8 is a 2D definition of the DCT.

$$G(n,m) = \frac{2}{\sqrt{MN}} \sum_{u=0}^{M-1} \sum_{v=0}^{N-1} \left[g(u,v)\, D_m^M(u)\, D_n^N(v) \right] \tag{4.8}$$

Where:

$$D_m^M(u) = C_m \cos\left(\frac{\pi(2u+1)m}{2M} \right)$$

and

$$D_n^N(v) = C_n \cos\left(\frac{\pi(2v+1)n}{2N}\right)$$

$$C_m = \begin{cases} \frac{1}{\sqrt{2}} & for\ m = 0 \\ 1 & otherwise \end{cases} \quad C_n = \begin{cases} \frac{1}{\sqrt{2}} & for\ n = 0 \\ 1 & otherwise \end{cases}$$

For $0 \leq m < M$ and $0 \leq n < N$ DCT spectrum has the same image size.

4.3.2 Cepstral and Pseudocepstral Analysis

The Cepstrum can be defined in different ways [Benesty et al.(2007)Benesty, Sondhi, and Huang, Whittaker and Shives(1983), Randall(2013)], but the first paper on Cepstral analysis (Ceps) introduced it as "the power spectrum of the logarithm of the power spectrum". In our study, it is the Fourier Transform of the log power spectrum for image $I(x, y)$ [Bogert(1963)]. See Eq.4.9.

$$Ceps = DFT\left\{\log \mid DFT\left\{I(x,y)\right\} \mid\right\} \tag{4.9}$$

Similarly, the pseudo Cepstrum (Pceps) can be introduced as shown in Eq.4.10. Instead of using the DFT, the proposed pseudo cepstral analysis uses the Discrete Cosine Transform. Not only did it not degrade the information contained in the general cepstrum, but it also improved the signal's energy compaction and resolution [Hassanein and Rudko(1984)].

$$PCeps = DCT\left\{\log \mid DCT\left\{I(x,y)\right\} \mid\right\} \tag{4.10}$$

4.3.3 Peak Signal Noise Ratio

It is suitable to introduce the Peak Signal to Noise Ratio ($PSNR$) due to the fact that there are several definitions in the scientific literature. In this thesis, $PSNR$ is calculated with Eq.4.11 in decibels [Sung et al.(2002)Sung, Kim, Kim, Kwak, Yoo, and Yoo]:

$$PSNR = 10\log_{10}\frac{R^2}{MSR} \tag{4.11}$$

Mean Square Error (MSE) is similarly defined in Eq.4.12:

$$MSE = \frac{1}{N \times M}\sum_{i=1}^{N}\sum_{j=1}^{M}\left[I(i,j) - I_n(i,j)\right]^2 \tag{4.12}$$

Where I is the reference grayscale image, I_n is the noisy grayscale image, and R is the highest pixel value in the reference image.

4.3.4 Radon Transform

Radon Transform is the collapse of a 2D $f(x, y)$ function, along an arbitrary line, at an angle θ_k. In other words, it is the sum of parallel rays along line ρ_j, which is actually a line integral. Its geometry and Sinogram are introduced in Fig.4.6(a) and Fig.4.6(b), respectively. The Radon Transform is presented in Eq.4.13.

$$g(\rho,\theta) = \int_{-\infty}^{+\infty}\int_{-\infty}^{+\infty} f(x,y)\delta(x\sin\theta + y\cos\theta - \rho)dxdy \tag{4.13}$$

4.3.5 Proposal of Algorithms

We have proposed two alternative algorithms to estimate motion blur angle and length for the reconstruction of the PSF. These are shown in Alg. 5.1 and 5.2, respectively. Figure 4.7 presents the process to calculate motion blur length using our DCT Pseudo Cepstrum.

Algorithm 4.1 Algorithm for the estimation of motion blur Angle.

1: Convert motion blurred image to Grayscale.
2: Apply 2D Discrete Cosine Transform to Motion blurred image .
3: Obtain logarithm of 2D DCT spectrum obtained in (2).
4: Binarize DCT Spectrum image (3) using a 0.9 threshold.
5: Apply Radon Transform to thresholded DCT spectrum (4).
6: Locate maximum Radon peak to find motion blur angle.

Algorithm 4.2 Algorithm for the estimation of motion blur Length.

1: Convert motion blurred image to Grayscale.
2: Rotate motion blurred image (1) using estimated motion blurred angle.
3: Apply 2D Discrete Cosine Transform to rotated image (2).
4: Obtain logarithm of 2D DCT spectrum (3).
5: Collapse and average 2D DCT spectrum (4) along 1D X axis.
6: Obtain logarithm of 1D collapsed 2D DCT spectrum (5).
7: Apply 1D Discrete Cosine Transform to (6).
8: Motion blur length is the lowest peak location in (7).

4.4 MATERIALS AND METHODS

The USC-SIPI image database (University of Southern California - Signal and Image Processing Institute) [sip(2017)] was used in this research. Although it was first Published in 1977, all its images have become standards for an image processing algorithm benchmark. We used a set of 20 color and grayscale images for this study. The image size selected was 512×512 pixels with 8 bits/pixel depth. Some of the color images were converted to grayscale following recommendation 601 from the International Telecommunication Union [bt6(2017)] (See Fig.5.6). Additionally, Matlab 2015b and its image processing toolbox were used to code angle and length estimation algorithms.

4.4.1 Noise robustness

The Gabor Steerable filter in space [Rekleitis(1996), Krahmer et al.(2006)Krahmer, Lin, McAdoo, Ott, Wang, Widemann, and Wohlberg], the Hough in frequency [Tiwari

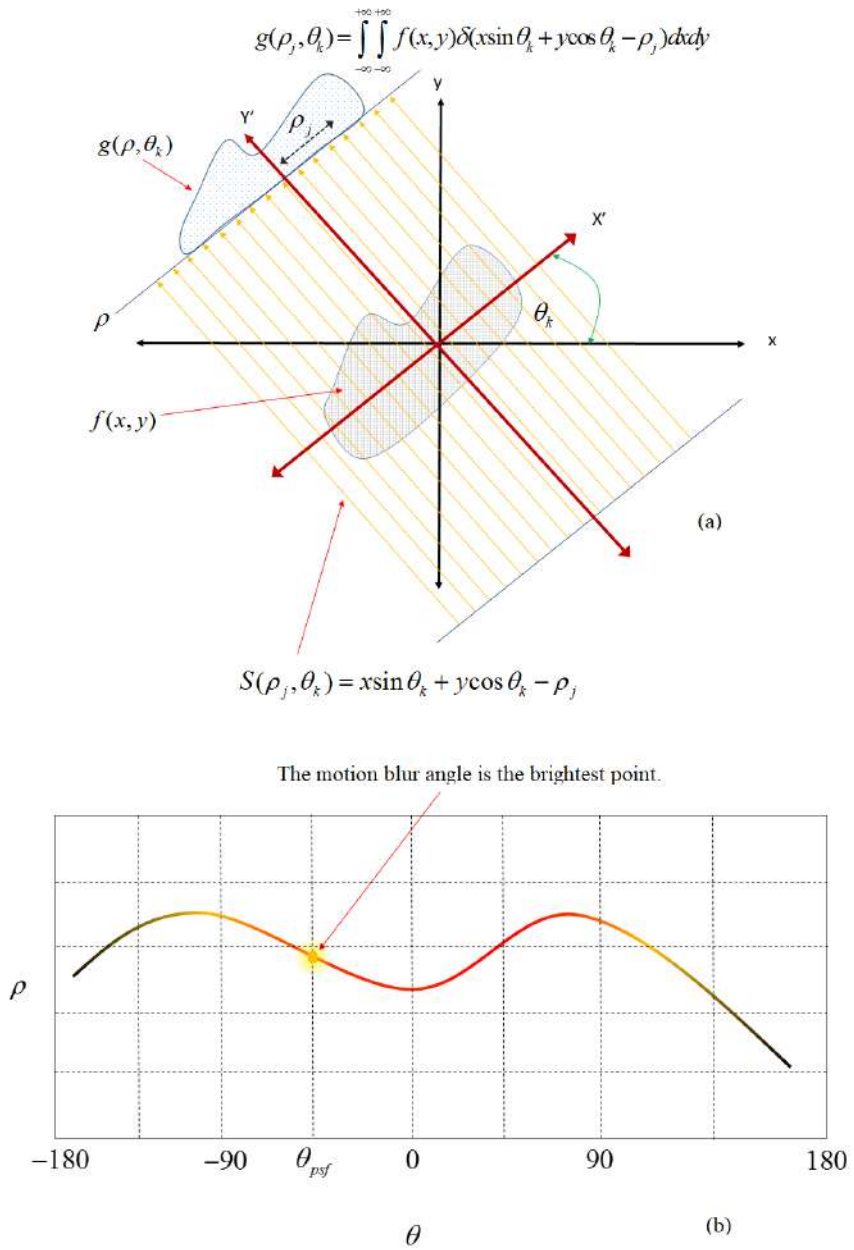

Figure 4.6: (a) Radon Transform Geometry and (b) Sinogram.

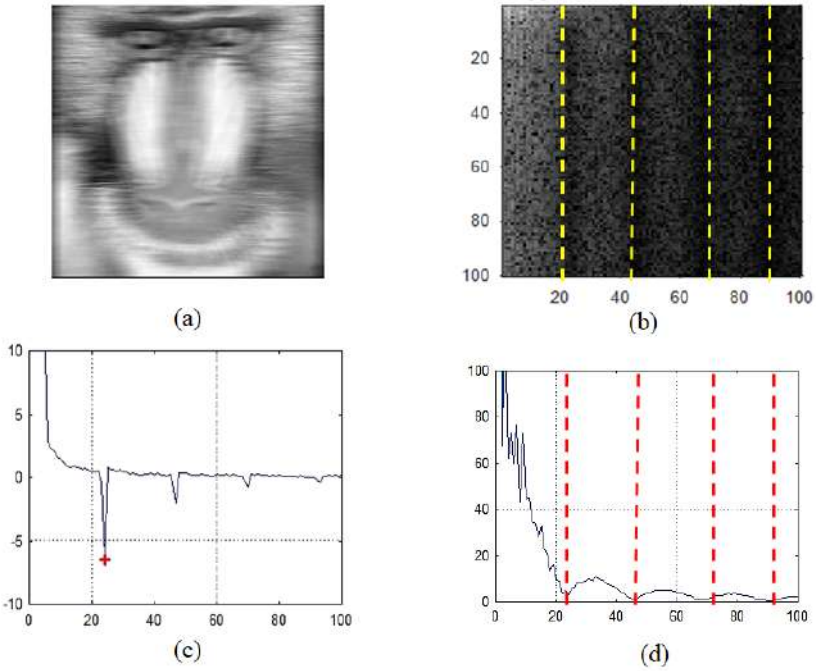

Figure 4.7: DCT Pseudo Cepstrum for length estimation. (a) Motion blur image. (b) 2D DCT power spectrum of motion blur image. (c) DCT Pseudo Cepstrum of collapsed Spectrum. (d) Colapsed spectrum of 2D DCT of motion blur image.

et al.(2014)Tiwari, Singh, and Shukla], the 2D Cepstrum [Krahmer et al.(2006)Krahmer, Lin, McAdoo, Ott, Wang, Widemann, and Wohlberg,Shah et al.(2014)Shah, Dalal, Deshpande, and Patnaik], Radon in frequency [Deshpande and Patnaik(2012)] algorithms, and our DCT-Radon proposal were implemented to carry out the angle experiments in order to estimate the mean absolute error of each method. Nowadays, this is a representative set of the most notable methods used in scientific literature to estimate motion blur angle. All 20 images were synthetically degraded at different angles from 0^{o} to 90^{o}, increasing one degree at the time, with 55 pixel motion blur length.

Furthermore, the Auto-correlation Function (ACF) in space [Yitzhaky and Kopeika(1997), Yitzhaky and Stern(2003)], DFT 1D Cepstrum [Krahmer et al.(2006)Krahmer, Lin, McAdoo, Ott, Wang, Widemann, and Wohlberg,Shah et al.(2014)Shah, Dalal, Deshpande, and Patnaik], DFT Radon [Dobeš et al.(2010)Dobeš, Machala, and Fürst], and our novel DCT proposal of modified Pseudo Cepstrum were tested using the same 20 images from USC-SIPI database. This was also done for angle estimation. All 20 images were synthetically motion blur degraded with lengths between five and 95 pixels, in one pixel intervals, at zero angle.

In addition, test Images were synthetically noise degraded for both the angle and the length estimation, by adding white Gaussian noise (AWGN) to produce a Peak Signal Noise Ratio range (PSNR) between 20dB and 36dB. Once again, all algorithms for the angle and the length estimation were assessed with each AWGN value to appraise their noise robustness.

4.4.2 Runtime comparison

To evaluate the runtime of each approach, only one noise-free image (Lenna) was used (See Fig.4.8(d)). Each algorithm was run 100 times to calculate its mean runtime.

4.5 EXPERIMENTAL RESULTS

Angle Estimation Results

The proposed DCT Radon had the lowest mean absolute error (0.66° degrees) for angle estimation for noise-free motion blurred images as seen in Fig.4.9 and Table 4.1. On the other hand, the DFT Gabor method mean value (0.90° degrees) was also close to DCT Radon, but the DFT Gabor had the longest runtime (≈ 2.92 s) and a broad spread of data. The DCT Radon proposal was not the fastest method (≈ 0.68 s); however, its runtime was average as shown in Fig.4.12 and Table 4.3.

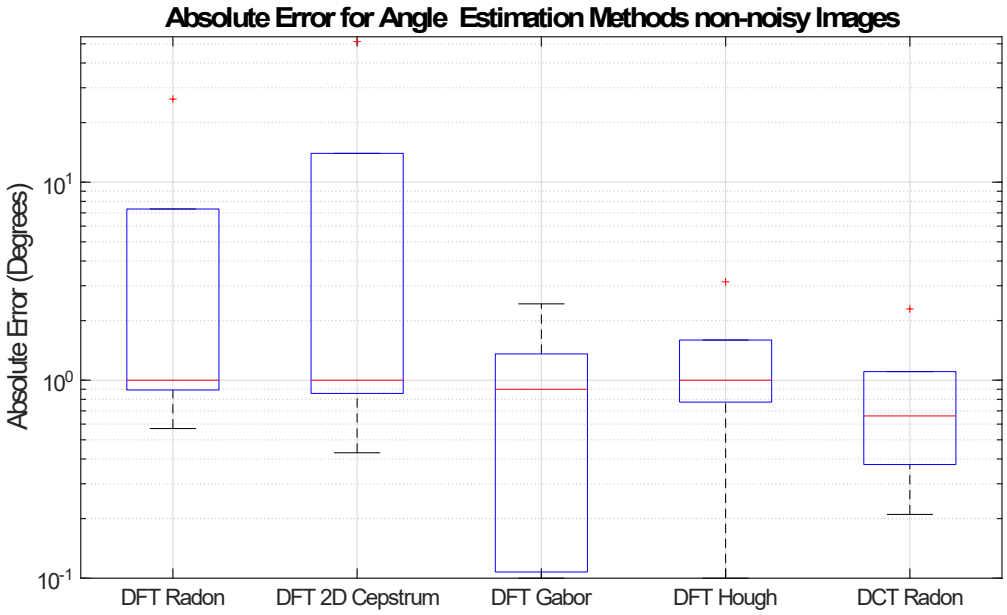

Figure 4.9: Mean Absolute Error comparison for angle estimation of noise-free motion blurred images. The boxplot chart shows the distribution of data based on minimum, first quartile Q_1, mean, third quartile Q_3, and maximum.

In contrast, regarding angle estimation, the DCT Radon approach was more tolerant of noise than all other evaluated methods. The DCT Radon mean absolute error for angle estimation was 1.70° degrees. Moreover, its worst estimation value was below 2.59° degrees for all cases, with a PSNR between 36 dB and 20 dB, which makes this method more noise robust. See the boxplot in Fig.4.10, the lowest solid line in Fig.4.11, and Table 4.2 for detailed information.

Length Estimation Results

From the bars in Fig.4.14 and Table 4.4, we can see that proposed DCT Pseudo Cepstrum has the lowest error (0.99 pixels) for noise-free motion blur length estimation.

Furthermore, our DCT Pseudo Cepstrum approach for length estimation is more tolerant than all the other evaluated methods. The error of the proposed DCT was always lower than

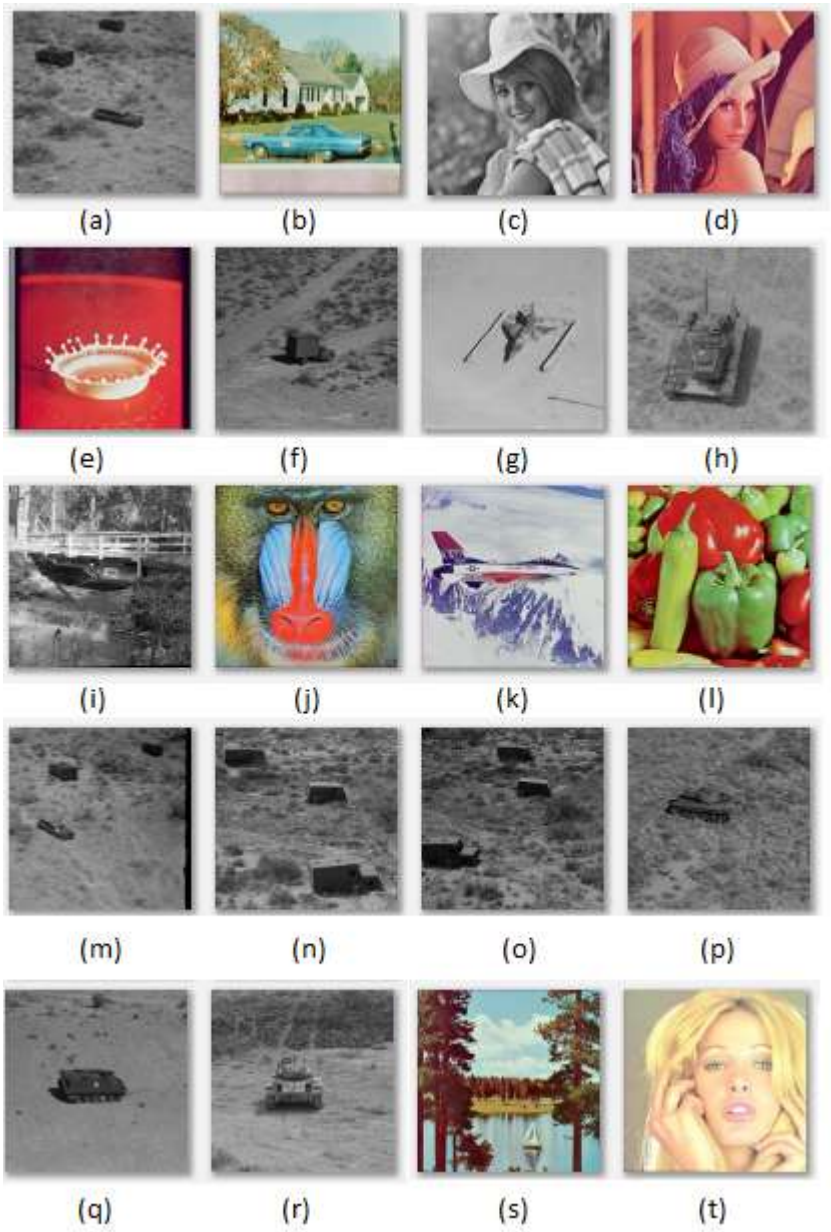

Figure 4.8: Sample images from USC-SIPI database used to carry out the experiments. (a)Car and APCs, (b)House, (c)Elaine, (d)Lenna, (e)Splash, (f)Truck, (g) Airplane, (h)Tank, (i)Stream and bridge, (j)Mandrill, (k)Airplane F-16, (l)Peppers, (m)Car and APCs (n)Truck and APCs, (o)Truck and APCs, (p)Tank, (q)APC, (r)Tank, (s)Sailboat on lake and (t)Tiffany.

Method	Min	Q_1	Mean	Q_3	Max
DFT Radon	0.57	1.00	1.00	1.00	26.29
DFT 2D Cepstrum	0.43	1.00	1.55	1.00	51.29
DFT Gabor	0.10	0.11	0.90	1.00	2.43
DFT Hough	0.10	1.00	1.08	1.00	3.14
DCT Radon	0.21	0.43	0.66	0.71	2.29

Table 4.1: Mean Absolute Error in degrees for Angle Estimation of noise-free Motion Blurred Images. It shows the distribution of data based on minimum, first quartile Q_1, mean, third quartile Q_3, and maximum.

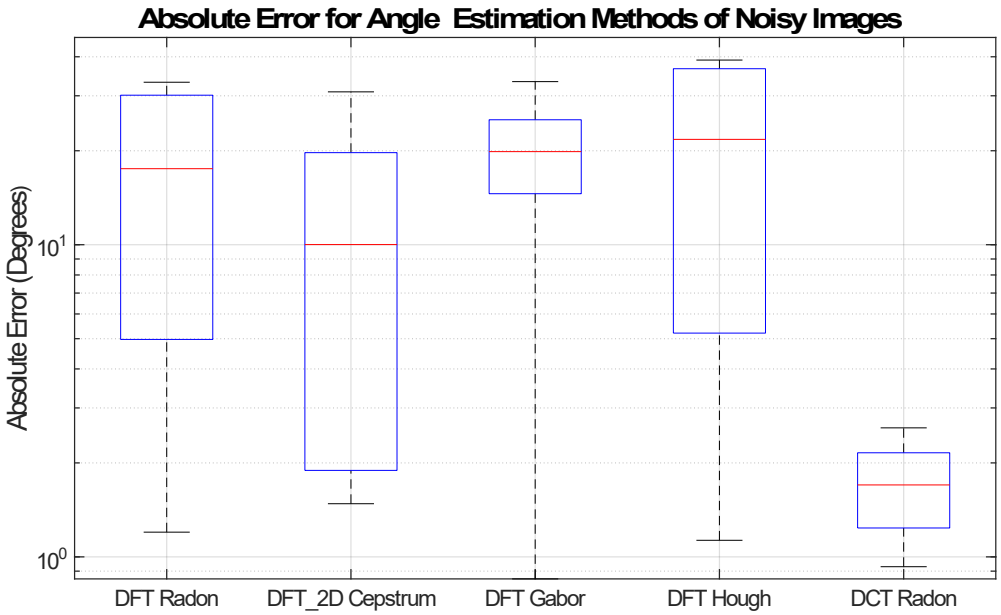

Figure 4.10: Mean Absolute Error for Angle Estimation of Noisy Motion Blurred Images. The boxplot chart shows the distribution of data based on minimum, first quartileQ_1, mean, third quartile Q_3, and maximum.

	Min	Q_1	Mean	Q_3	Max
DFT Radon	1.20	6.23	17.52	29.12	33.15
DFT 2D Cepstrum	1.48	2.03	10.01	16.00	30.88
DFT Gabor	0.85	19.14	19.87	22.41	33.30
DFT Hough	1.13	6.57	21.75	35.82	39.04
DCT Radon	0.93	1.34	1.70	2.01	2.59

Table 4.2: Mean Absolute Error for Angle Estimation of Noisy Images. The Table shows the distribution of data based on minimum, first quartile Q_1, mean, third quartile Q_3, and maximum.

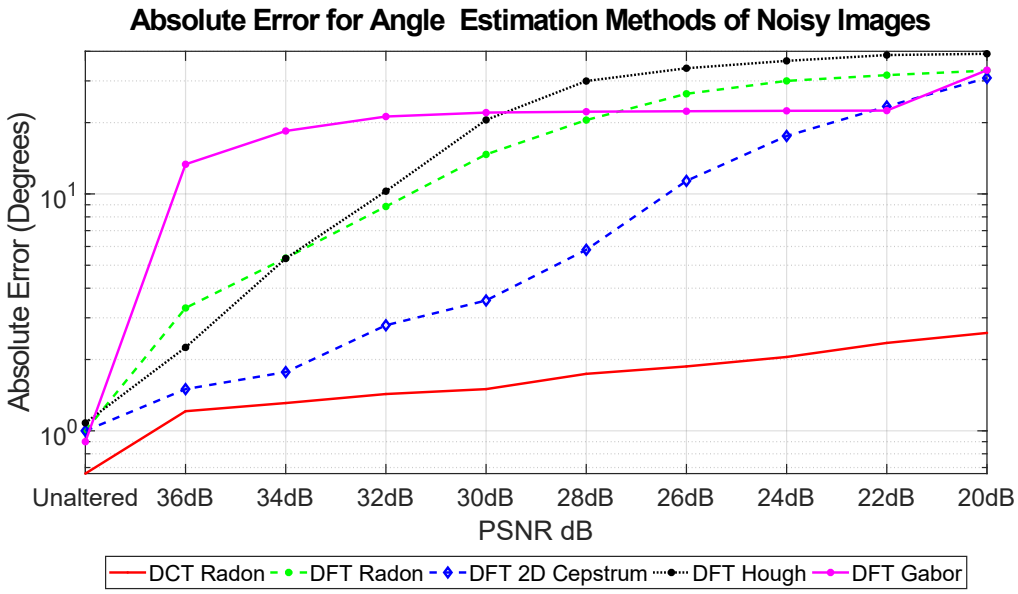

Figure 4.11: Mean absolute errors between actual and predicted blur angles.

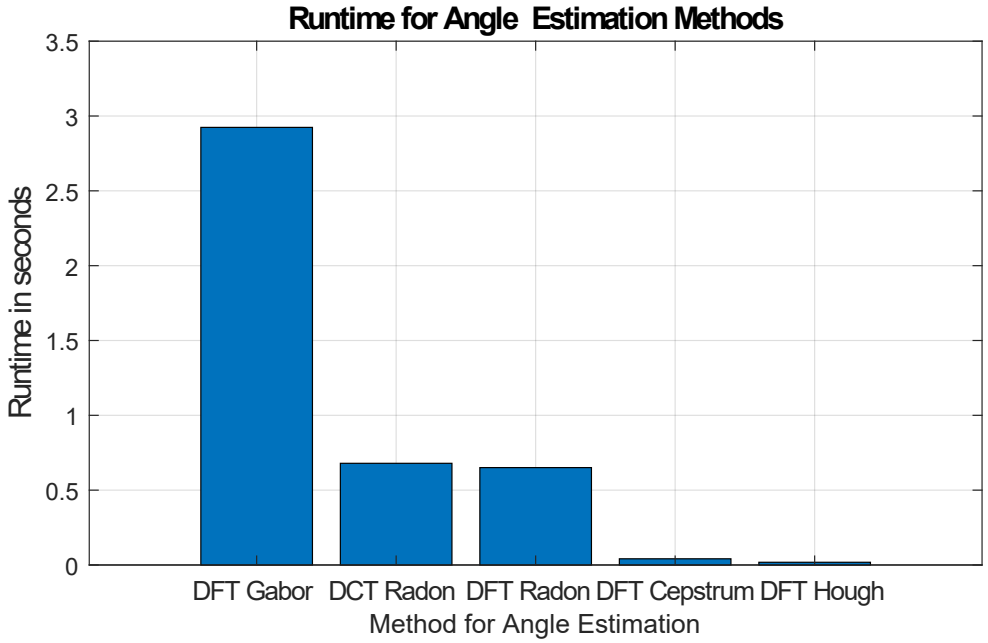

Figure 4.12: Mean runtime for angle estimation methods in seconds.

Method	Runtime (s)
DFT Radon	0.600 ± 0.0000332
DFT 2D Cepstrum	0.041 ± 0.0000076
DFT Gabor	2.920 ± 0.0006673
DFT Hough	0.018 ± 0.0000035
DCT Radon	0.680 ± 0.0000318

Table 4.3: Mean runtime for angle estimation methods in seconds.

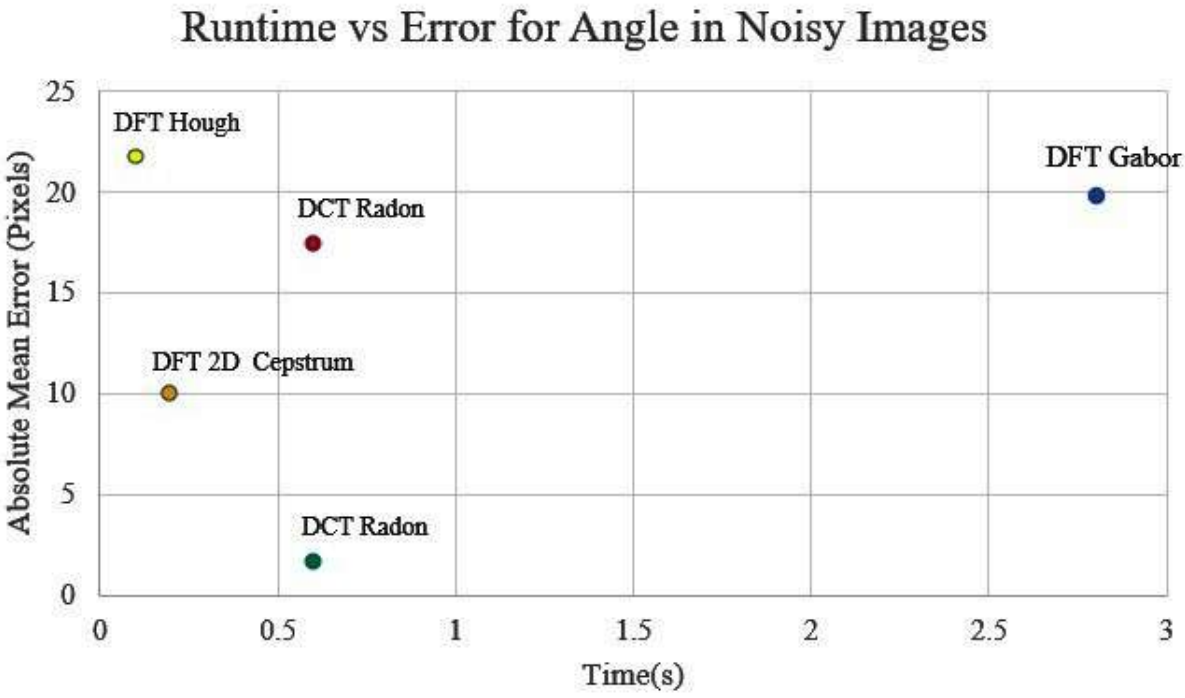

Figure 4.13: Runtime vs Mean Error for Angle in noisy images. DCT radon is the method that is closer to the zero in terms of both variables.

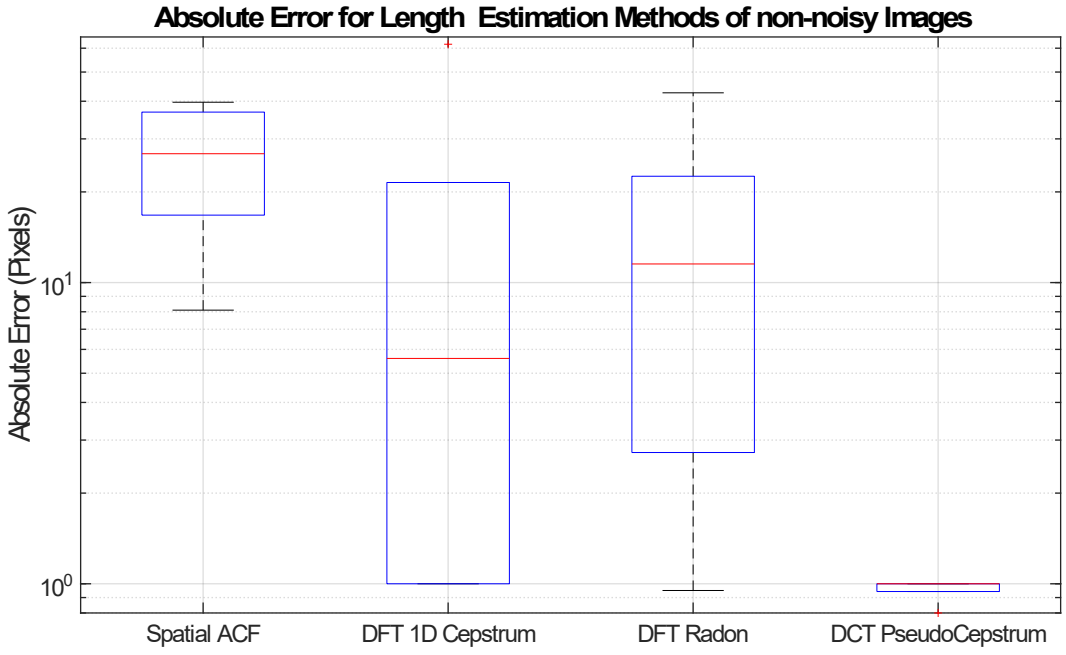

Figure 4.14: Mean Absolute Error Comparison for length estimation of the methods evaluated for noise-free motion blurred images. The boxplot shows the distribution of data based on minimum, first quartile Q_1, mean, third quartile Q_3, and maximum.

Method	Min	Q_1	Mean	Q_3	Max
Spatial ACF	8.10	19.63	26.78	35.85	39.70
DFT 1D Cepstrum	1.00	1.00	8.04	5.60	61.85
DFT Radon	0.95	3.32	11.53	15.84	42.66
DCT Pseudo Cepstrum	0.80	1.00	0.99	1.00	1.00

Table 4.4: Mean Absolute Error in pixels for Length Estimation of noise-free Images. The Table shows the distribution of data based on minimum, first quartile Q_1, mean, third quartile Q_3, and maximum.

Method	Min	Q_1	Mean	Q_3	Max
Spatial ACF	26.78	47.27	45.78	48.50	48.50
DFT 1D Cepstrum	8.04	43.08	39.75	43.42	43.48
DFT Radon	9.32	11.89	18.21	24.71	28.69
DCT Pseudo Cepstrum	0.99	2.71	7.78	11.63	19.13

Table 4.5: Mean Absolute Error in Pixels for Length Estimation of Noisy Images. The Table shows the distribution of data based on minimum, first quartileQ_1, mean, third quartile Q_3, and maximum.

19.3 pixels. In the worst scenario, and it also had a mean error of 7.78 pixels in the presence of AWGN, as seen in the boxplot chart in Fig.4.15 and Table 4.5.

Although a shorter runtime is desirable, the results have shown that our DCT Pseudo Cepstrum is close to the DFT Radon method for length estimation. See Fig.4.17 and Table 4.6.

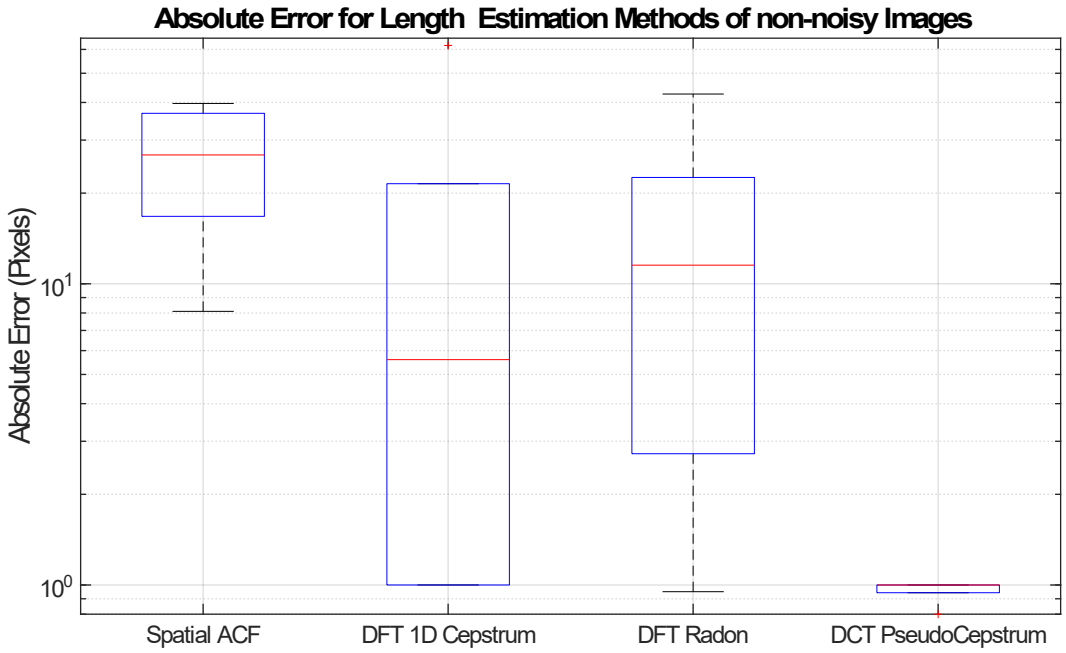

Figure 4.15: Mean Absolute Error in Pixels for Length Estimation of Noisy Images. The boxplot shows the distribution of data based on minimum, first quartile Q_1, mean, third quartile Q_3, and maximum.

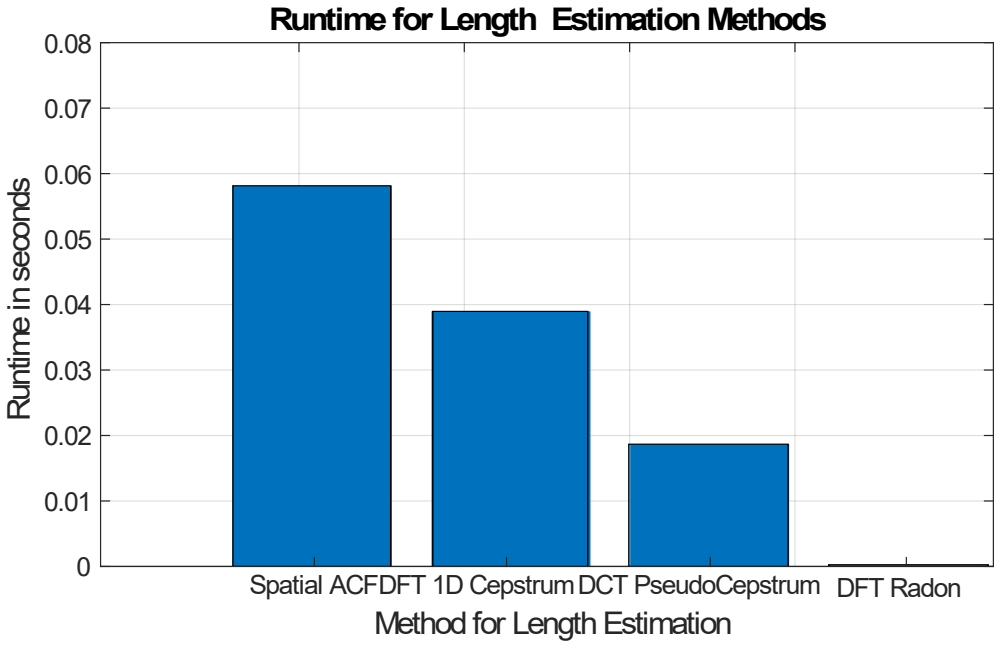

Figure 4.17: Mean runtime for Length estimation.

When Mean Error and Runtime are plotted simultaneously, it is possible to find a more suitable approach in terms of both variables. DCT radon and DCT Pseudo Cepstrum for angle and length estimation are the best as shown in Fig. 4.13, and Fig. 4.18, respectively.

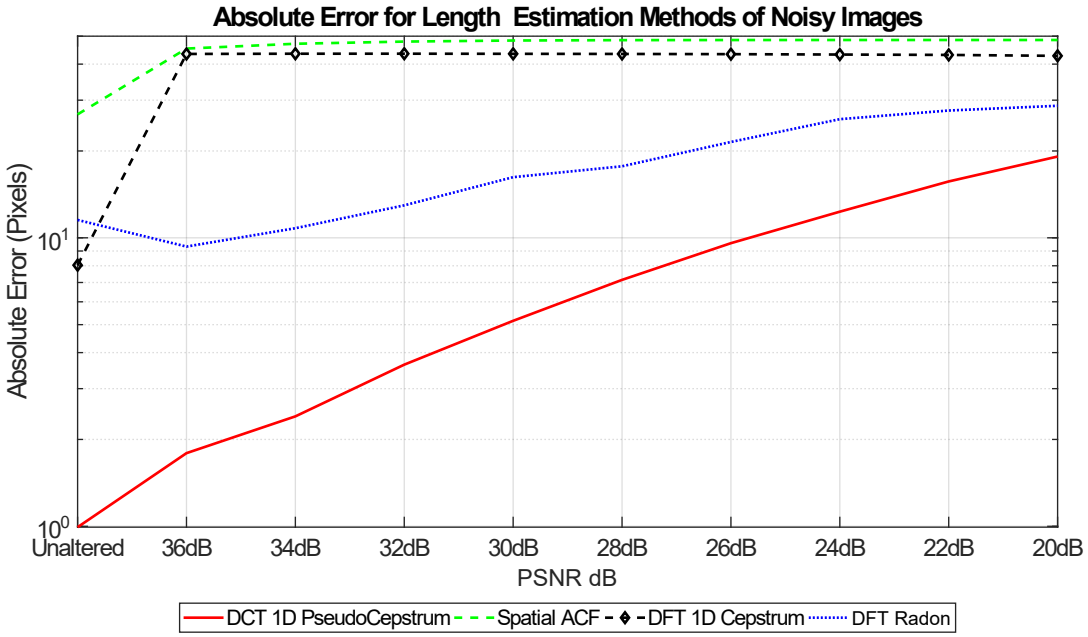

Figure 4.16: Mean absolute error between actual and predicted blur length.

Method	Runtime (s)
Spatial ACF	0.0581467 ± 0.0000018
DFT 1D Cepstrum	0.0186817 ± 0.0000022
DFT Radon	0.0002700 ± 0.0000021
DCT Pseudo Cepstrum	0.0389605 ± 0.0000026

Table 4.6: Mean runtime for angle estimation methods in seconds.

4.6 DISCUSSION

The Yoshida, Horiike and Fujita method [Yoshida et al.(1993)Yoshida, Horiike, and Fujita] also used the DCT to only estimate motion blur length, but their approach was completely manual, as mentioned earlier. On the other hand, they used their DCT approach only to estimate motion blur length, and our proposed DCT methods were used to measure the length and the angle with no human intervention even in the presence of AWGN. The solid red line in Fig.4.16 shows that the DCT proposal for our DCT Pseudo Cepstrum has a lower mean absolute error for motion blur length estimation. This novel DCT Pseudo Cepstrum proposal is much more robust against noise than the other evaluated methods, but its runtime of less than 0.03 seconds is not as fast as the other methods evaluated. See bars in Fig.4.17 and Table 4.6. These DCT approaches can be easily implemented to restore linear motion blur images using some well-known deconvolution algorithms, such as the Richardson–Lucy [Richardson(1972), Lucy(1974)] or the Wiener algorithms, among other applications. It is not considered in this thesis.

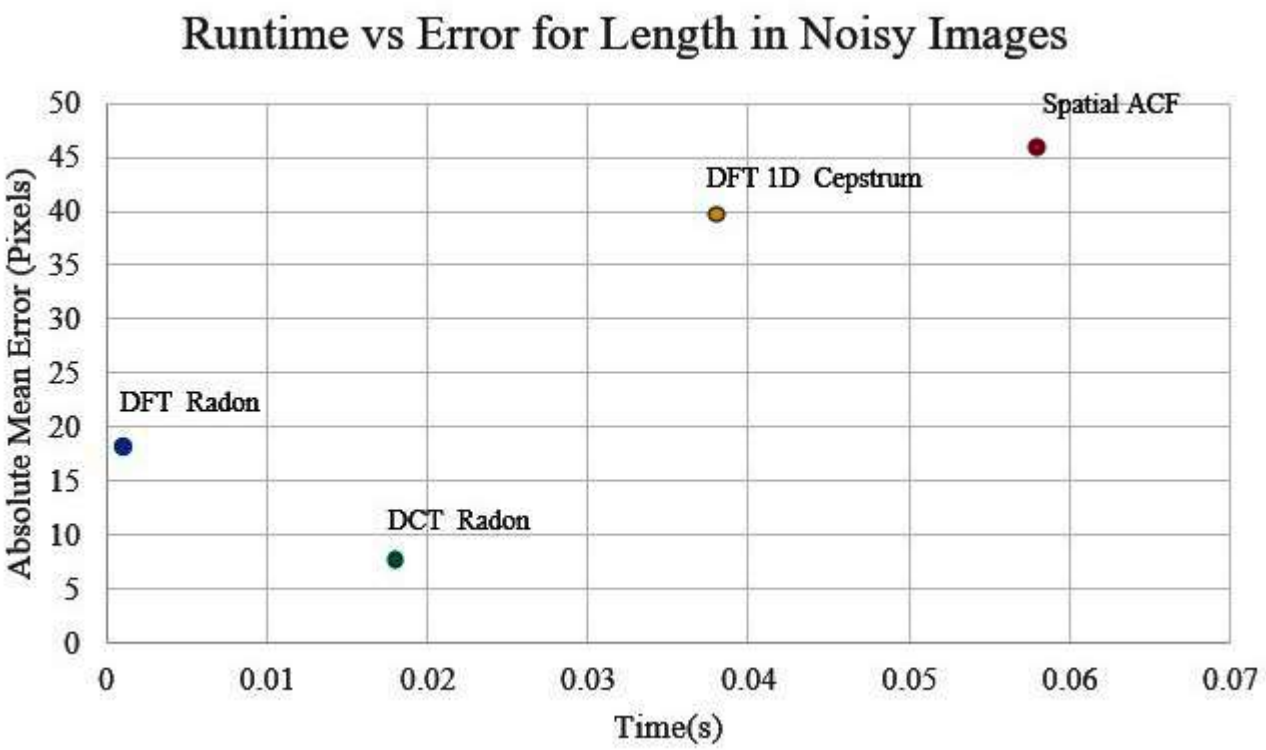

Figure 4.18: Runtime vs Mean Error for length in noisy images. DCT radon is the method that is closer to the zero in terms of both variables.

4.7 CONCLUSIONS

Our DCT approaches to the Point spread Function parameters estimation of invariant uniform linear motion blurred images has shown to be a suitable alternative for its reconstruction even in the presence of Gaussian noise in a signal-to-noise ratio ranging between 20 dB and 36 dB. Its mean absolute error for angle estimation was 0.66° degrees and 7.78° degrees for noise-free and noisy images, respectively. Regarding to runtime of angle estimation, it took 0.68 seconds. Furthermore, with respect to length estimation, our DCT Pseudo Cepstrum had the lowest mean error of 0.99 pixels and 7.78 pixels for noise-free and noisy images, respectively. Its mean runtime for length estimation was 0.04 seconds. Runtime for length and angle estimation are suitable to consider these methods for real time application. ITM Journal published, in Spanish, a portion of the comparison results introduced in this chapter for the reconstruction of the point spread function as shown in [Cortés-Osorio et al.(2018)Cortés-Osorio, López-Robayo, and Hernández-Betancourt]. This paper did not include the DCT proposal which succeeded the other alternatives evaluated.

Chapter 5

VELOCITY ESTIMATION

This chapter introduces a new approach for estimating kinematic quantities, namely the angle and the relative speed, from an actual single motion blur image using the Discrete Cosine Transform (DCT). Motion blur is a common phenomenon present in images. It is produced by the relative movement between the camera and the objects in the scene during camera sensor exposure to light. It usually happens to image recording systems mounted in vehicles, hand-held cameras, drones, satellites, and mobile robots. Today, this source of kinematic data is mostly dismissed in favor of image restoration. Our software-based technique focuses on cases where the camera moves at a constant linear velocity while the background remains unchanged. We took 2250 motion blur pictures for the angle experiments and 500 for the speed experiments, in a light and distance controlled environment, using a belt driven motor slider at angles between 0 and 90 and 10 preset speeds. The DCT Hough and DCT Radon results were compared to DFT Hough and DFT Radon algorithms for angle estimation. The Mean Absolute Error (MAE) of DCT Radon method for direction estimation was 4.66° degrees. Additionally, the Mean Relative Error for speed estimation of the DCT Peudo Cepstrum was 5.15%. Our alternative DCT frequency analysis proposals were more accurate than all competitors evaluated for the reconstruction of the Point Spread Function (PSF) that enable calculation of relative velocity and motion direction.

5.1 INTRODUCTION

Classic speed measurement methods can be divided in hardware-based and software-based methods. Some examples for hadware-based methods are magnetic and capacitive sensors, lasers, and radars. The software-based methods use video images to measure some variables. Usually, hardware-based solutions for velocity are invasive, more expensive and bulky [Pelegri et al.(2002)Pelegri, Alberola, and Llario, Li et al.(2011)Li, Dong, Jia, Xu, and Qin, Odat et al.(2017)Odat, Shamma, and Claudel, Cheung et al.(2005)Cheung, Ergen, and Varaiya]. This research focuses on a software-based solution that proposes the use of a single motion-blurred image to calculate velocity, although other multi-frame video strategies were used in [Luvizon et al.(2017)Luvizon, Nassu, and Minetto, Wang(2016), Kruger et al.(1995)Kruger, Enkelmann, and Rossle, Litzenberger et al.(2006)Litzenberger, Kohn, Belbachir, Donath, Gritsch, Garn, Posch, and Schraml].

Blurring can be generated by relative motion between a camera and observed scene when there is a long exposure time. It causes a reduction of high-frequency content in

the image, perceivable in the direction of motion. This study only considers the estimation of relative velocity from a single mechanical motion blurred image, which occurs when the relative velocity between the different objects in the scene and the camera is high, in comparison to the exposure time [Lin and Li(2004a), Šorel et al.(2009)Šorel, Šroubek, and Flusser, Bovik(2009), Bovik(2010), Pretto et al.(2009)Pretto, Menegatti, Bennewitz, Burgard, and Pagello, Chan and Shen(2005b), Potmesil and Chakravarty(1983)]. Motion blur is common in surveillance, speeding ticket and laboratory cameras. It happens when either people, vehicles, or cameras move with respect to one another. All of this usually produces a degradation of the image. Researchers have been actively developing techniques that restore the parts of the image that are masked by motion blur [Arashloo and Ahmadyfard(2007), Jia and Wen(2013), Gal et al.(2014)Gal, Kiryati, and Sochen]; however, there is also the possibility of harnessing the information provided by the distortion itself in order to analyze the movement that produced the blur in the first place.

Analyzing the nature of motion blur in images captured with mobile robots allows us to have implicit information which provides an overview of the kinematics of the observed object or the robot itself. In some of image processing and robotics studies, blur is eliminated from images and videos, in turn neglecting the implicit kinematic information blur can provide [Dai and Wu(2008), Joshi et al.(2010)Joshi, Kang, Zitnick, and Szeliski, Li et al.(2012)Li, Zhang, Fu, and Meng, Wu et al.(2011)Wu, Ling, Yu, Li, Mei, and Cheng, Sorel and Flusser(2008), Rajagopalan and Chellappa(2014)].

Today, mobile robots play an increasingly important role in places where direct human intervention has a high risk: nuclear power plants, contaminated areas, places of natural disasters, minefields, and terrorist attacks. Traditional robotic hardware systems are large, unwieldy and, in some cases, limited to remote-controlled systems [Rizo et al.(2003)Rizo, Coronado, Campo, Forero, Otalora, Devy, and Parra, Rajasekharan and Kambhampati(2003), Nagatani et al.(2013)Nagatani, Kiribayashi, Okada, Otake, Yoshida, Tadokoro, Nishimura, Yoshida, Koyanagi, Fukushima, et al., Yamamoto(1992), Murphy et al.(2008)Murphy, Tadokoro, Nardi, Jacoff, Fiorini, Choset, and Erkmen, Casper and Murphy(2003)]. The proposed single image solution to estimate velocity can help reduce the use of external additional sensors and camera specifications. This study introduces a computational algorithm based on the Discrete Cosine Transform to extract valuable image information from unwanted motion blur images. These images are actually rich in kinematic quantities and can support decision-making at the scene without having to stop the robot camera to capture a new frame to avoid blur.

Motion blur has been recently used to estimate kinematic quantities that describe the motion captured in an image. Lin, Huei-yung and Li [Lin and Li(2004a), Lin and Li(2004b), Lin(2005)] proposed a method to estimate the speed of moving vehicles from single still images based on motion blur analysis for the purpose of traffic law enforcement. The speed of a moving vehicle is calculated according to imaging geometry, camera parameters, and the estimated blur parameters. They took a picture of a turntable with known constant angular velocity to verify the accuracy of their method as a reference measurement. They reported results of less than 10% error for highway vehicle speed detection. Kawamura, Satoshi and Kondo [Kawamura et al.(2002)Kawamura, Kondo, Konishi, and Ishlgakl] proposed an algorithm to estimate the optical flow of a moving object with the motion blur in a scene using Cepstral analysis. The authors stated that accuracy in both velocity and orientation estimation was improved if the speed increased. They did not provide any reference of how they estimated speed error in their research. Alternatively, Xu and Zhao's proposal [Xu and Zhao(2010)] performed object speed measurement with uniformly accelerated/retarded motion, by using a single interlaced

scanned CCD image. They used a video sequence approach to calculate the actual motion speed to estimate its margin of error. Celestino and Horikawa [Celestino and Horikawa(2008)] gathered elements for the study and analysis of principal problems and difficulties inherent in the implementation of a device used for the inspection of motor vehicle speedometers, to meet anticipated Brazilian legislation requirements. Speed information was then determined by analyzing the uniformities contained in the dynamic image due to the blur effect. They compared the motion blur estimated speed to the actual speed by using a toothed wheel, a hall sensor, and an oscilloscope. Song et al. [Song et al.(2009)Song, Peng, Lu, Yang, and Yan] introduced a digital imaging-based method for measuring the velocity of pneumatically conveyed particles. By controlling exposure time blurred images of moving particles were captured, which contained particle velocity information. In order to improve the robustness of the system to noise in the acquired particle images, the traveling wave Equation (TWE) method was used to estimate motion blur length, and subsequently deduce particle velocity. Rezvankhah et al. [Rezvankhah et al.(2012)Rezvankhah, Bagherzadeh, Moradi, and Member] described an air hockey puck velocity estimation technique based on motion blur images. The proposed approach was implemented with an actual air hockey table, using two different cameras. They did not provide information about error estimation in their method. Taherkhani and Mohammadi [Mohammadi and Taherkhani(2013)] presented a speed measurement method of spherical objects using a single motion blur image taken in front of a still background. They estimated their method error by comparing it to a video-based approach. The actual speed was calculated by measuring the distance traveled between two fixed locations divided by the time difference. They reported the estimation error was lower than 4%. Pazhoumand-dar et al. [Pazhoumand-Dar et al.(2010)Pazhoumand-Dar, Abolhassani, and Saeedi] carried out their experiments for speed estimation using a toy car. They stated, in their paper, that the actual speed of the vehicle was an approximation. They did not provided any information about the calibration method to guarantee a measurement within an acceptable range. Furthermore, according to their report, only about 10 images were used to evaluate their proposed algorithm.

These are some remarkable studies regarding the estimation of kinematic quantities from single motion blur images. However, a great deal of work remains to be done on this topic.

In this chapter we mainly focus on computing the parameters of the linear motion blur kernel, namely length L and angle θ. These variables are used to estimate some kinematic quantities [Pretto et al.(2009)Pretto, Menegatti, Bennewitz, Burgard, and Pagello, Zhang and Hirakawa(2015)].

5.1.1 Motion Blur Length Estimation using Continuous Cosine Transform

The mathematical framework that supports DCT approach to the estimation of blur length is introduced in 3.2. That section explains widely both cases for constant velocity and acceleration. It is highly recommended to review the full chapter 3 if needed further details.

5.1.2 Motion Blur Angle Estimation using Discrete Cosine Transform (DCT)

The DFT spectrum of a motion blurred image has anisotropic nature due to the predominant presence of motion lines in space. Moreover, the spectrum is positioned in a direction

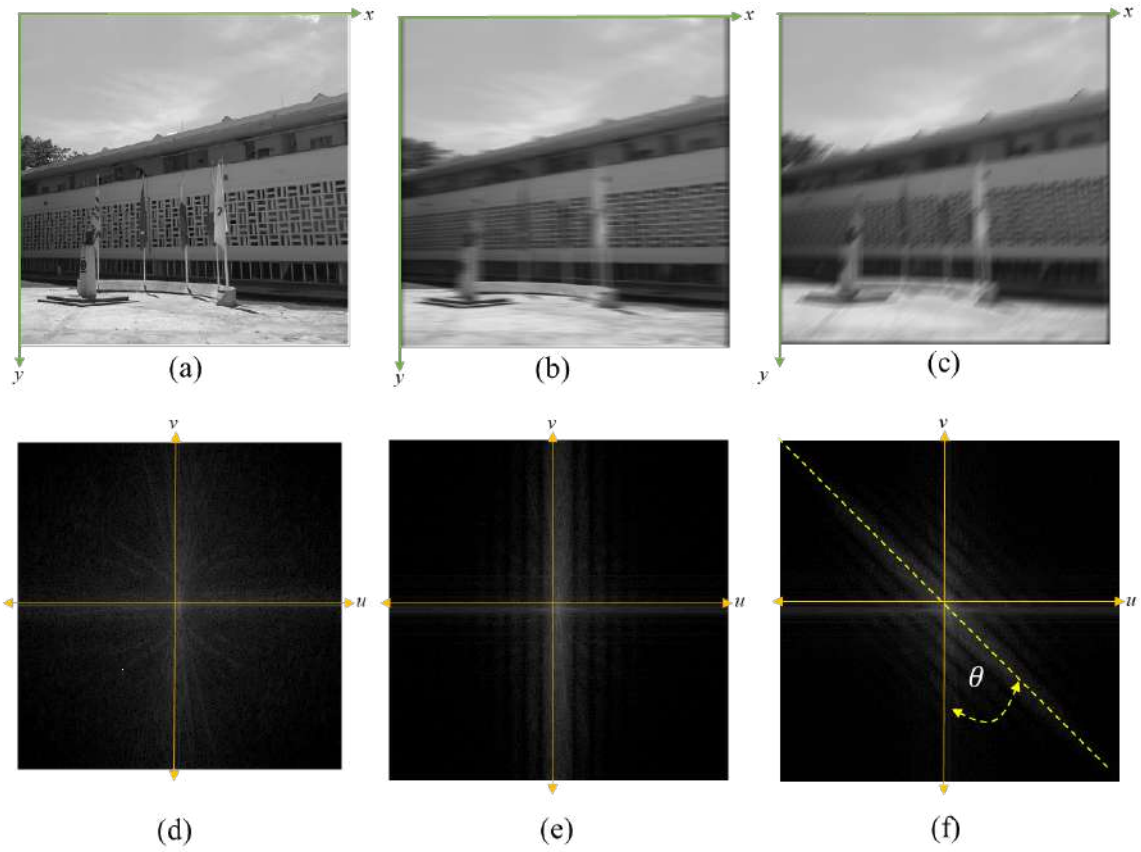

Figure 5.1: Angle estimation of a building image at several motion blur angles. (a) No blurred building image. - (b) Motion blurred building image at 0. - (c) Motion blurred building image at 45. - (d) DFT Power spectrum of image (a). - (e) DFT Power spectrum of image (b). - (f) DFT Power spectrum of image (c). This images has not been windowed.

perpendicular to the motion. It enables us to find the motion blur angle by estimating the relative position of either the dark or bright zones of the rippling pattern, but this needs to be windowed to soften the rapid change in image's edges, which produces undesired brighter lines along the center of the power spectrum pattern as seen in Fig.5.1. In contrast, the DCT power spectrum is also positioned perpendicular to the motion, but its energy is more concentrated than DFT as shown in Fig.5.2(e) and 5.1(e), respectively. DCT ripples are better defined and easier to trace in frequency.

5.1.3 Velocity from Linear Motion Blur

Our proposal to calculate the relative velocity of a moving object from a single linear motion blur image is based on the pinhole camera model introduced in [Lin and Li(2004a), Lin and Li(2004b), Lin(2005)] (See Fig.5.3).

Assuming that the angle between the image plane (1) and the motion direction (2) is θ, the displacement of the point object (3) is d in a exposure time interval T, we can obtain Eq.5.1 and 5.2 from the lower and upper triangle depicted in Fig.5.3:

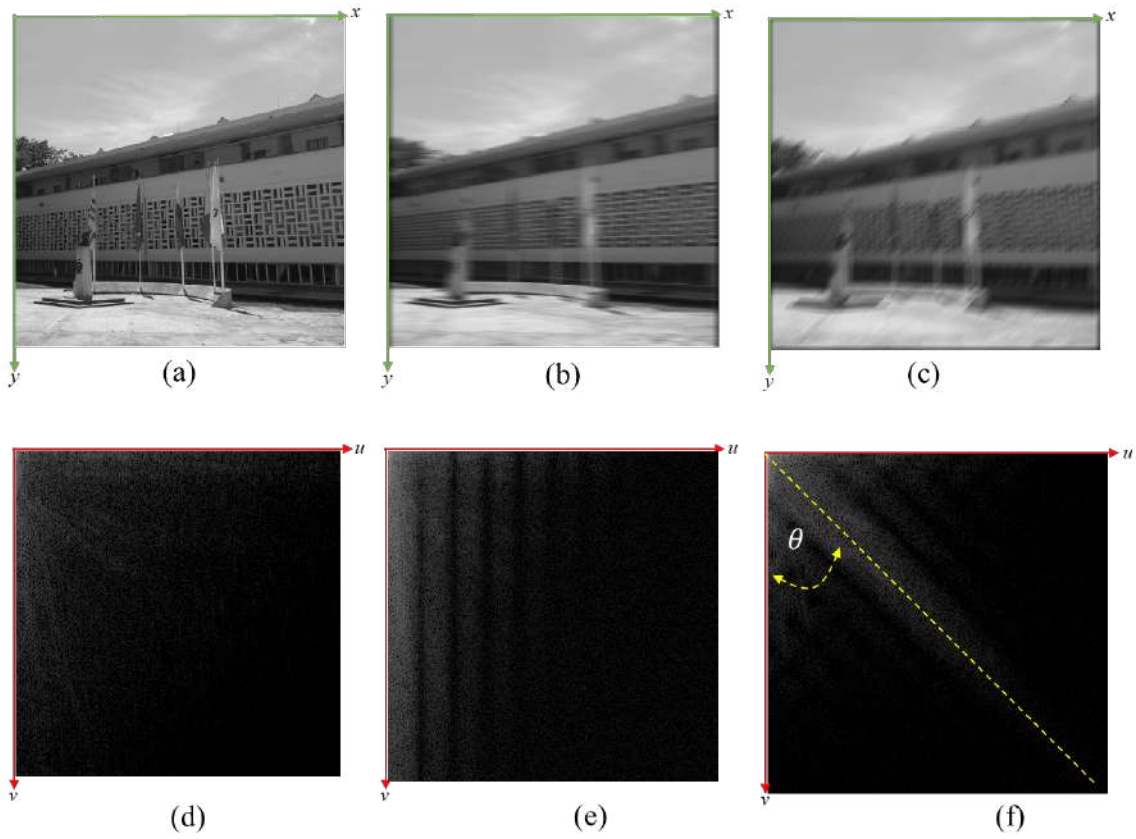

Figure 5.2: Angle estimation of a building image at several motion blur angles. (a) No blurred building image. - (b) Motion blurred building image at 0. - (c) Motion blurred building image at 45. - (d) DCT Power spectrum of image (a). - (e) DCT Power spectrum of image (b). - (f) DCT Power spectrum of image (c).

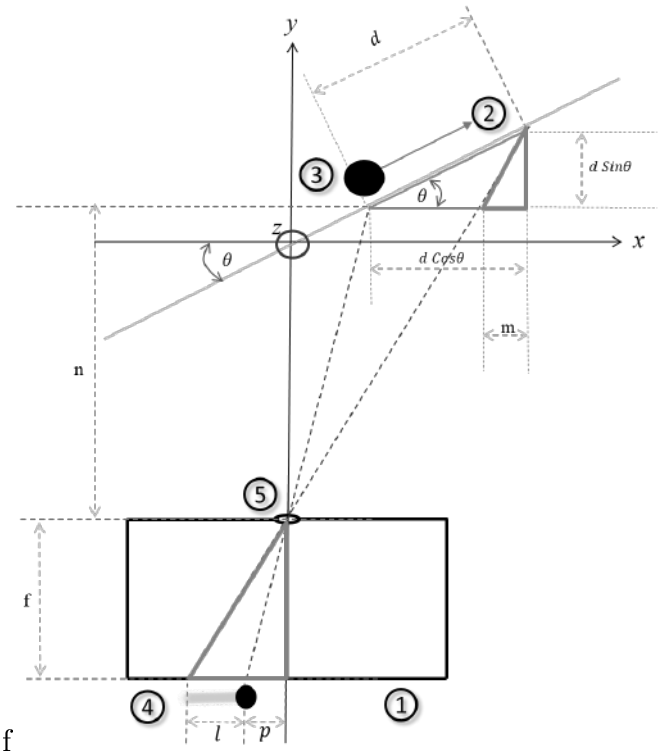

If

Figure 5.3: Upper view of camera model for point object speed estimation using blur length.

$$\frac{f}{p+l} = \frac{d\ \sin(\theta)}{m} \tag{5.1}$$

$$\frac{d\ \cos(\theta) - m}{l} = \frac{s}{f} \tag{5.2}$$

Where l is the length of the Motion blur (4) on the image plane and d represents the distance from axis Y to the final position. Additionally, n is the perpendicular distance from the Pinhole (5) to the starting point of the Moving object, and f is the camera focal length. In order to eliminate the emerging variable m, we plug Eq.5.1 into 5.2 and solve d as shown in Eq.5.3 (See Fig.5.3).

$$d = \frac{nl}{f\ \cos(\theta) - (p+l)\ \sin(\theta)} \tag{5.3}$$

Assuming the motion velocity of the point object is constant along the trajectory, we can state Eq.5.4:

$$v = \frac{d}{T} \tag{5.4}$$

$$v = \frac{nl}{T\left[f\ \cos(\theta) - (p+l)\ \sin(\theta)\right]} \tag{5.5}$$

Now writing Eq.5.5 in terms of the pixel size S_x of the digital camera, which can be obtained from the camera specifications or the camera calibration process, to obtain Eq.5.6:

$$v = \frac{nLS_x}{T\left[f\ \cos(\theta) - S_x(P+L)\ \sin(\theta)\right]} \tag{5.6}$$

P and L, in capital letters, are the distances from the vertical axis, both measured in pixels.

If the image plane and the motion direction are parallel, then $\theta = 0$. In this case, Eq.5.6 can be simplified to Eq.5.7:

$$v = k\frac{L}{T} \tag{5.7}$$

The term $k = \frac{nS_x}{f}$ is a scaling factor that can be obtained using the Zhang calibration method [Zhang(2000), Strobl et al.(2006)Strobl, Sepp, Fuchs, Paredes, and Arbter].

5.2 DISCRETE COSINE TRANSFORM PROPOSAL

We used the principle introduced in 4.3.2 for velocity estimation. Therefore, in this case, we used the DCT instead of the DFT as shown in Eq.5.8. The proposed pseudo-Cepstral analysis (PCeps) improved the signal's energy compaction and increased noise tolerance [Hassanein and Rudko(1984)].

$$PCeps = DCT\left\{\log \mid DCT\left\{I(x,y)\right\} \mid\right\} \tag{5.8}$$

Even though this method was used before only form length estimation of the PSF, we extended its usability as part of the variables used to calculate velocity.

5.2.1 DCT Algorithms

As mentioned earlier, these algorithms first were introduced in 4.3.5 for length and angle estimation. Algorithm 5.1 and Algorithm 5.2 are the modified versions for angle and speed estimation using actual motion blurred images, respectively.

Algorithm 5.1 Algorithm for direction estimation.

1. Set camera exposure time T.
2. Convert motion blurred image to Grayscale if needed.
3. Apply 2D Discrete Cosine Transform to Motion blurred image .
4. Calculate logarithm of 2D DCT spectrum obtained in (3).
5. Binarize DCT Spectrum image (4) using a 0.9 threshold.
6. Apply Radon Transform to thresholded DCT spectrum in (5).
7. Locate maximum Radon peak to find Velocity Direction Angle.

Algorithm 5.2 Algorithm for speed estimation.

1. Set camera exposure time T.
2. Take a single picture from a fixed parallel distance.
3. Convert motion blurred image to Grayscale, if needed.
4. Rotate motion blurred image (3) using estimated motion blur angle.
5. Apply 2D Discrete Cosine Transform to rotated image in (4).
6. Obtain logarithm of 2D DCT spectrum (5).
7. Collapse and average 2D DCT spectrum (6) along 1D X axis.
8. Obtain 1D logarithm of collapsed 2D DCT spectrum (7).
9. Apply 1D Discrete Cosine Transform to (8).
10 Motion blur length L is the lowest peak location in (9).
11. Perform camera calibration to find the scaling factor k.
12. Calculate speed using $v = k\frac{L}{T}$.

5.3 MATERIALS AND METHODS

5.3.1 Complete Rig set-up

The slider and camera set-up to take the pictures were employed in a controlled environment, so ambient light, distance to pattern poster, minimum and maximum exposure time of camera, slider velocity, camera aperture, platform tilt, and belt driven motor slider angle were known. The images were taken from a point of view parallel to the pattern poster and the camera slider motion line. An adjustment arm was used to set the camera angle (See Fig.5.4). Angle and Length of the PSF allow calculation of the relative velocity of the camera system as described later.

5.3.2 The Camera

We used a Color Basler acA2000-165um USB 3.0 camera with the CMOSIS CMV2000 CMOS sensor at 2 MP resolution for the experiments [Basler(2017)]. This camera permitted control of the image resolution, the external hardware trigger, the exposure time, the gain, while providing us with precise specifications of focal length, pixel size, and sensor size. Furthermore, it has interchangeable C- mount lenses. All these are needed to ensure laboratory controlled conditions. Even though the camera can capture up to 165 frames per second, we only used one frame to evaluate velocity.

5.3.3 The lens

The camera did not have any built-in lens, so we decided to use a Ricoh lens FL-CC0814A-2M [Ric(2017)]. Some of its main characteristics are: C-mount, 2/3" image circle, F1.4 - F16.0 iris, and a 100 mm working distance. It is usually used for classic machine vision applications.

5.3.4 Camera calibration

We performed a camera calibration process to compute the scaling factor k. Some variables, such as the perpendicular distance n from camera to poster, the pixel size Sx and the focal

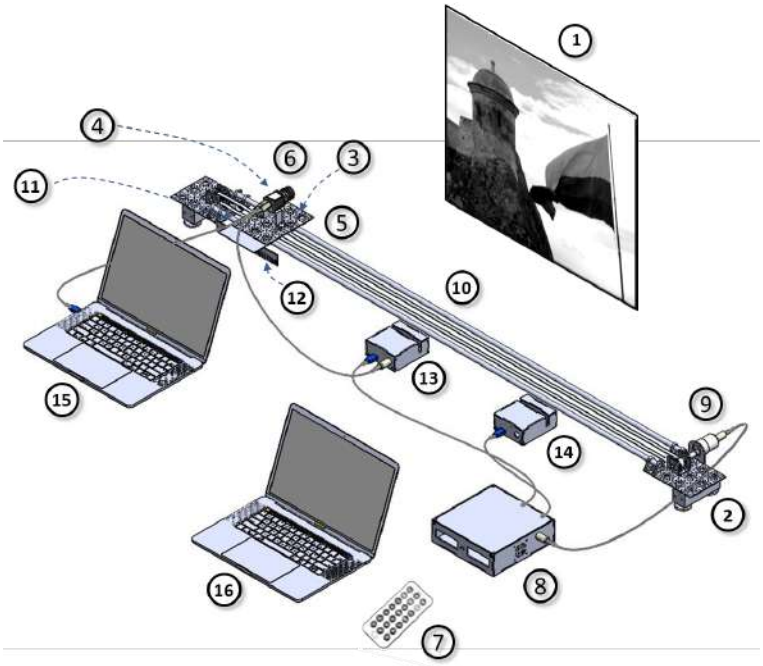

Figure 5.4: Complete rig setup to capture motion blur images using the Motor Belt Driven Camera Slider. (1) Pattern Posters, (2) Two Leveling Rubber Feet, (3) Bubble Level, (4) Digital Pitch Gauge, (5) Camera Sliding Carriage Platform, (6) Camera, (7) Remote control, (8) The Controller, (9) PWM Driven Motor, (10) Stainless Steel Rods, (11) Low Friction Linear Bearings, (12) Laser-Cut Toothed Steel Sheet, (13) Camera Trigger, (14) Limit switch, (15) Image Capture Computer, and (16) Data Analysis Computer.

length f, are needed to calculate the relative speed of the camera using Eq.5.6. We decided to try a different approach. Instead of measuring the values proposed by Lin et al. [Lin and Li(2004a), Lin(2005), Lin and Li(2004b)] and Mohammadi and Taherkhanil [Mohammadi and Taherkhani(2013)], the proposed technique required the camera to take only once 20 reference digital pictures of a planar like-checkerboard pattern, shown at a few different positions, to obtain the intrinsic and the extrinsic camera parameters. As previously mentioned, this strategy is based on the Zhang's calibration method [Zhang(2000),Strobl et al.(2006)Strobl, Sepp, Fuchs, Paredes, and Arbter].

5.3.5 The slider

We made our own 185cm long Motor Belt driven camera slider. Most of its parts are made of aluminum. Figure 5.4 presents all the parts included to operate the capture system. Also, we used five different Pattern Posters (1) located at a 121-cm fixed parallel distance from the rig. Figure 5.6 shows all five pattern posters used to carry out the experiments. Two Leveling Rubber Feet (2) with threaded studs were set under each one of the two-rod insertion supports. Additionally, a Bubble Level (3) and a Digital Pitch Gauge (4) were mounted on the Camera Sliding Carriage Platform (5) as well as the Camera (6), respectively, to measure any needed angle. We set the constant speed of the Sliding Carriage Platform, using a Remote control (7), among 10 possible preset speeds. The Controller (8), powered the PWM (Pulse-Width Modulation) Driven Motor (9), which drove a toothed belt to pull the camera platform. Pitch,

(a) Camera . (b) Complete Rig Setup.

Figure 5.5: Rig setup to take the actual motion blur images at ten different preset velocities.

yaw, and roll rotations were considered to achieve linear motion and set the Camera position. After this, the Platform slipped on the two oiled stainless Steel Rods (10) which lay on four Low Friction Linear Bearings (11). The Sliding Platform also had an Laser-Cut Toothed Steel Sheet attached (12) to it, used to to take a single picture when its first tooth reached the Slotted Optical Switch Sensor of the Camera Trigger (13), so as to measure and send the obstruction time per each tooth to the Controller. The Limit switch (14) is an emergency stop that halts the Sliding Platform, also it can be done by using the built-in remote control.

When the camera is shot by the the Camera Trigger, the digital image (snapshot) is sent to the Image Capture Computer (15) through the wiring.

Finally, we compared the results obtained from a single motion blur image to the actual speed value calculated by the wireless (Bluetooth) Data Analysis Computer (16). Figure 5.5 presents the actual rig setup used to carry out the experiments to generate spatially invariant motion blur images in the laboratory.

5.3.6 The images

We used a set of five images taken from five different posters for this study as shown in Fig.5.6. All color pictures were taken from a fixed distance (121cm), cropped at 512×512 pixels for image size, then converted to 8-bit grayscale following recommendation 601 from the International Telecommunication Union [bt6(2017)].

5.3.7 Direction estimation method

The Hough in frequency (DFT Hough) [Tiwari et al.(2014)Tiwari, Singh, and Shukla], Radon in frequency (DFT Radon) [Deshpande and Patnaik(2012)], and our DCT-Radon and DCT Hough proposed algorithms were implemented to carry out the angle experiments to estimate the Mean Absolute Error of each method. All five images were actual motion blur degraded at different angles from 0° to 90°, at a one-degree interval, with the same $V9$ preset speed (See

(a) University. (b) Bus. (c) UTP. (d) City. (e) Flag.

Figure 5.6: Pattern posters used to carry out the direction and speed experiments.

Table 5.1). We took five pictures for each angle to obtain a total of 2250 sample motion blur images (90 angles $\times$ 5 images per angle $\times$ 5 posters) for angle estimation experiments.

5.3.8 Speed estimation method

The Autocorrelation Function (ACF) in space [Yitzhaky and Kopeika(1997), Yitzhaky and Stern(2003)], 1D Cepstrum [Krahmer et al.(2006)Krahmer, Lin, McAdoo, Ott, Wang, Widemann, and Wohlberg, Tiwari and Shukla(2013), Tiwari et al.(2014)Tiwari, Singh, and Shukla] and our DCT proposal of a modified Pseudo Cepstrum were tested using the five pattern posters to estimate motion blur length L in laboratory conditions.

The exposure time T and the camera aperture of the lens' diaphragm were set at 100 ms and $F/4$, respectively. We calculated the speed using Eq.5.7. with a scaling factor $k = 0.7789\,\text{mm/pixel}$. The slider and the camera were flat across the surface, presenting zero degrees of tilt.

As mentioned before, the slider had 10 different preset speeds listed in Table 5.1. Even though the slider speeds are repeatable and close to the those shown in Table 5.1, we used each individual reading of the Controller to assess the error between its actual value and the image based value.

We took 10 pictures for each preset speed, to obtain a total of 500 sample motion blur images (10 speeds$\times$10 images per speed$\times$5 images) for speed estimation experiments.

Index	Speed (m/s)	Index	Speed (m/s)
V0	0,2243	V5	0,4674
V1	0,2871	V6	0,5109
V2	0,3454	V7	0,5329
V3	0,3935	V8	0,5444
V4	0,4303	V9	0,6021

Table 5.1: Preset Speeds of the Motor Belt Driven Camera Slider.

5.4 EXPERIMENTAL RESULTS

5.4.1 Angle Estimation Results

Initially, we calculated angle (Motion direction) using a classic DFT Hough approach and our alternative DCT Hough. Mean Absolute Error for angle estimation was plotted for both Hough methods as seen in Fig.5.7. DCT Hough Mean Absolute Error was lower than DFT Hough MAE for the majority of angles plotted. In addition, Fig.5.9 revealed that data dispersion around its mean value for DCT Hough method was smaller than the DFT Hough approach for angle estimation.

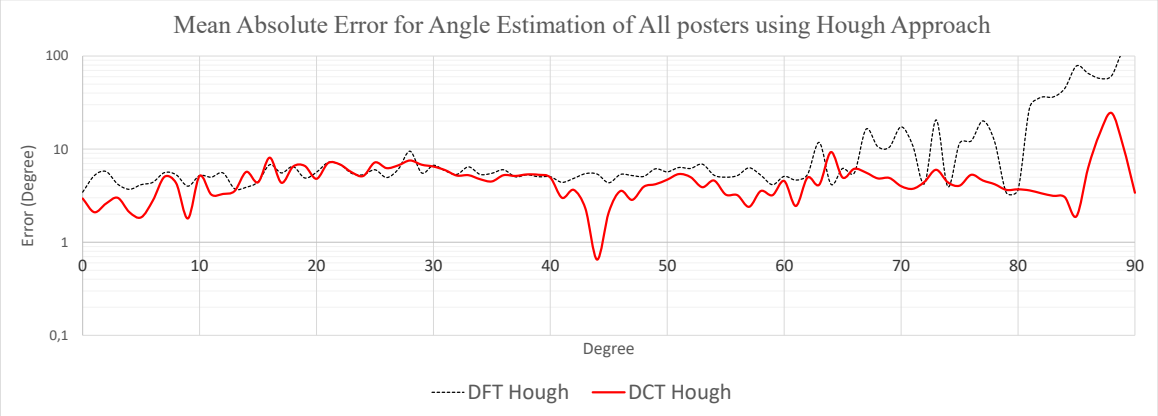

Figure 5.7: Mean Absolute Error for Angle Estimation of All posters using DFT and DCT Hough Approaches.

However, as seen in Fig.5.8, our DCT radon method was even better than the DFT Radon method for angle estimation. DCT approaches for angle estimation had smaller MAE than its DFT competitors.

We plotted only the DCT approaches for angle estimation to compare them. Figure 5.9 shows that the DCT Radon method for angle estimation was almost always under the DCT Hough curve.

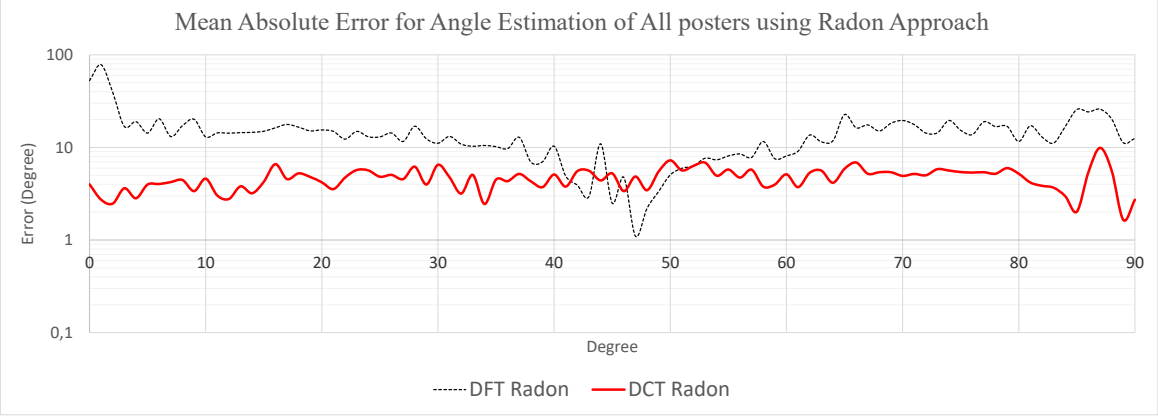

Figure 5.8: Mean Absolute Error for Angle Estimation of All posters using DFT and DCT Radon Approaches.

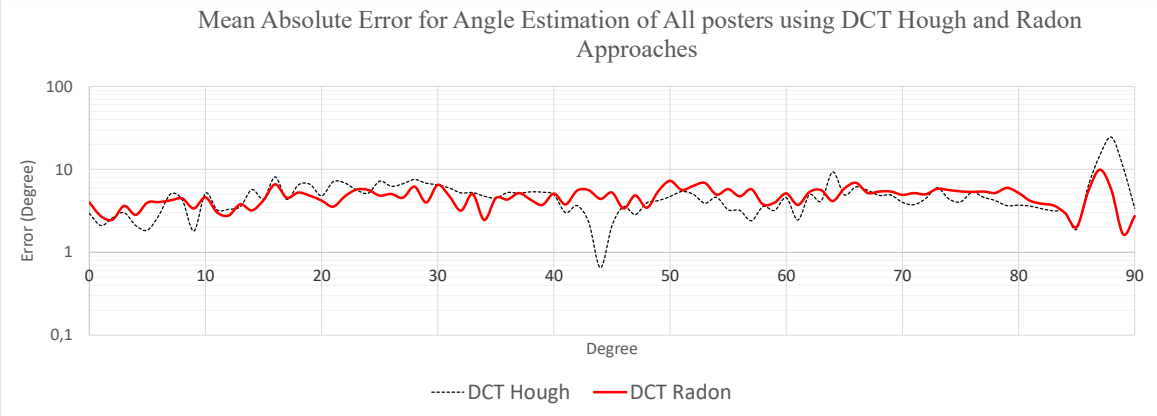

Figure 5.9: Mean Absolute Error for Angle Estimation of All posters using using DCT Hough and Radon approaches.

Finally, the boxplot chart in Fig.5.10 and Table5.2 sum up the result of all methods used for angle estimation. Each box presents minimum, percentile 0.25, mean, percentile 0.75 and maximum value. The shortest column is the DCT Radon method, among all angle estimation methods. The DCT method also had a narrower data dispersion between 1.65° and 9.9° degrees, and a smaller mean absolute angle error of 4.65° degrees.

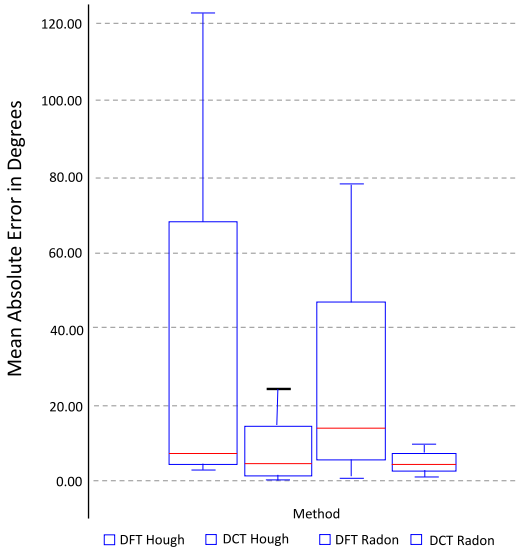

Figure 5.10: Boxplot: Absolute Error for Angle Estimation Methods of DFT Hough, DCT Hough, DFT Radon and our DCT Radon.

5.4.2 Speed Estimation Results

Every pattern poster from Fig.5.6 was located at 121cm from the camera, the same we did for angle estimation. Figure 5.14 shows the results we obtained using all posters shown in Fig.5.6. We can see that the DCT Radon approach to estimate the relative speed of the camera had the lowest Mean Relative Error compared to all the other methods tested.

Finally, we obtained a mean plot for all five posters used to perform the experiments at each speed, as seen in Fig.5.14, for all methods evaluated. The DCT Pseudo Cepstrum approach is

Method	Min	Q_1	Mean	Q_3	Max
DFT Hough [Tiwari et al.(2014)Tiwari, Singh, and Shukla]	3.4	5.03	12.86	7.05	122.95
DFT Radon [Deshpande and Patnaik(2012)]	1.10	10.25	14.36	16.83	78.25
DCT Radon	1.65	3.83	4.69	5.43	9.09
DCT Hough	0.65	3.36	4.88	5.39	24.45

Table 5.2: Absolute Error for Angle Estimation Methods in Actual Images in degrees.

Method	Min	Q_1	Mean	Q_3	Max
Spatial ACF [Yitzhaky and Stern(2003)]	77.39	77.75	83.27	84.36	106.14
DFT 1D Ceps [Tiwari and Shukla(2013)]	78.97	87.00	88.29	91.15	92.21
DFT Radon [Deshpande and Patnaik(2012)]	52.48	57.88	100.79	131.01	209.15
DCT PseudoCeps	2.69	4.37	5.15	5.37	9.03

Table 5.3: Relative Error speed Estimation Methods in Actual Images (Percentual).

lower at all speeds and its absolute mean error is always below 9.03%. The boxplot chart in Fig.5.11 and its Table 5.3 sum up the results obtained in speed experiments. As seen in the box for the DCT method to calculate the speed, this approach has less data dispersion (between 2.69% and 9.03%) in its Relative Error.

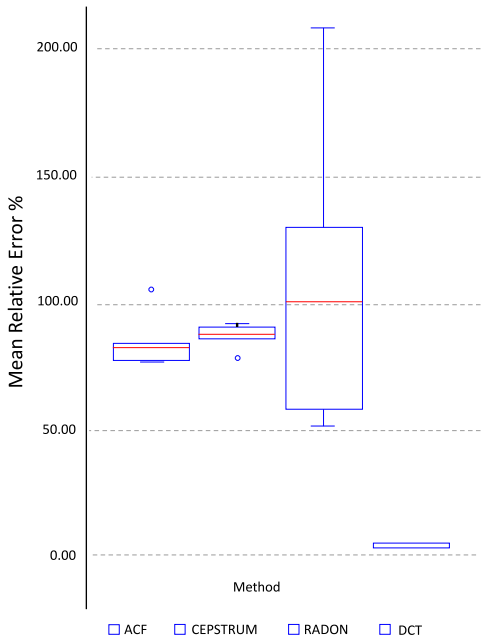

Figure 5.11: Boxplot: Relative Error for Speed Estimation Methods of ACF, DFT Cepstrum, DFT Radon, and our DCT Pseudo Cepstrum.

5.4.3 Correlation evaluation

The correlation matrix was evaluated to find the relationship between the error and some image characteristics such as energy, entropy, homogeneity, contrast, brightness, and correlation. These were plotted using all the actual poster images. As seen in the results shown in Fig.5.12, error is inversely proportional to the entropy and the brightness of the image. On the other hand, as presented the Pearson coefficient, there exists a strong correlation between the speed and the error.

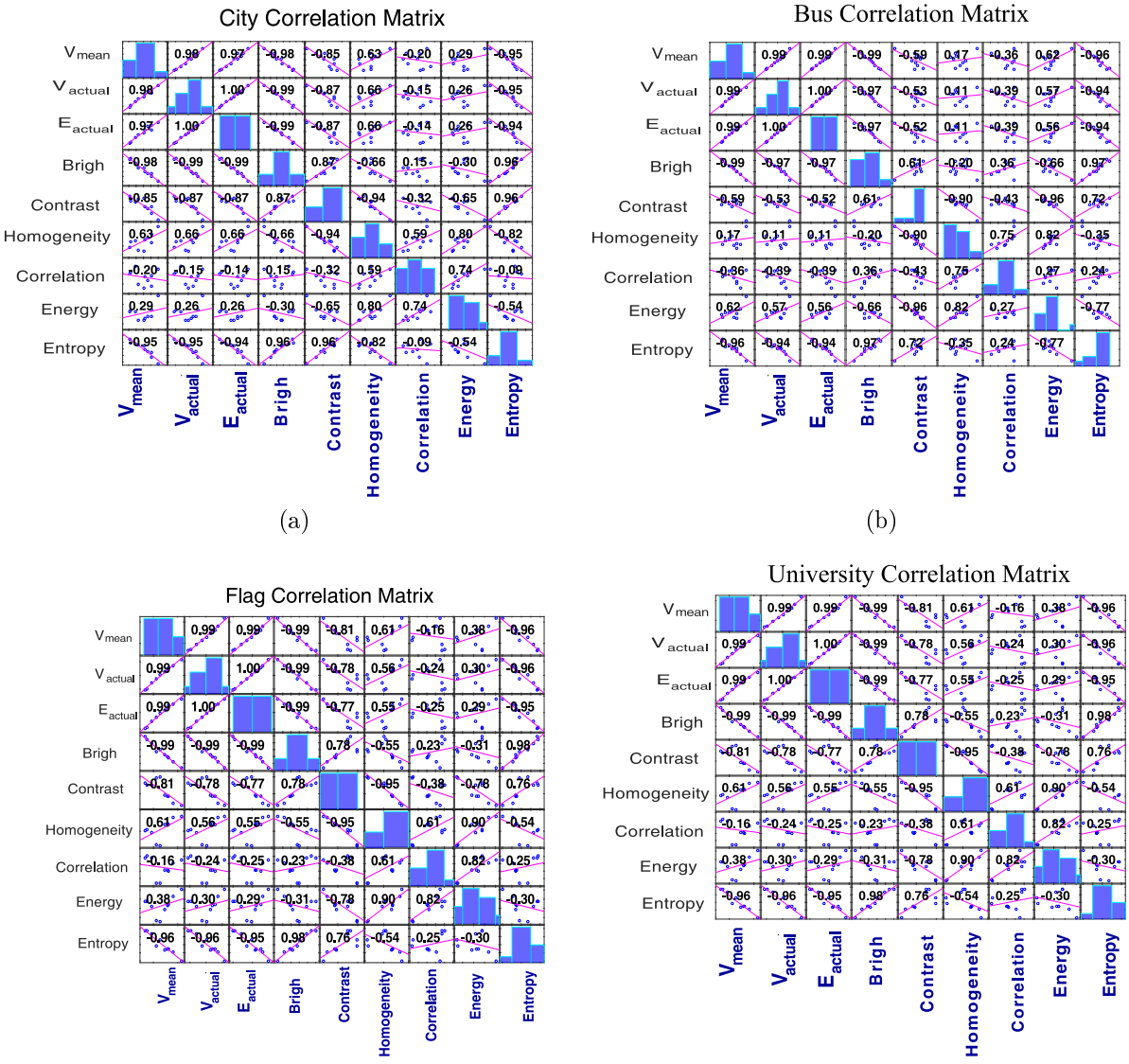

Figure 5.12: Correlation matrix for (a) City, (b) Bus, (c) Flag, and (d) University. All plots show a strong relationship between the Error and the image Entropy.

5.4.4 Repeatability and Reproducibility Analysis

Repeatability is the change that is perceived when the same operator measures the same component many times, using the same measurement system, under the same conditions. A

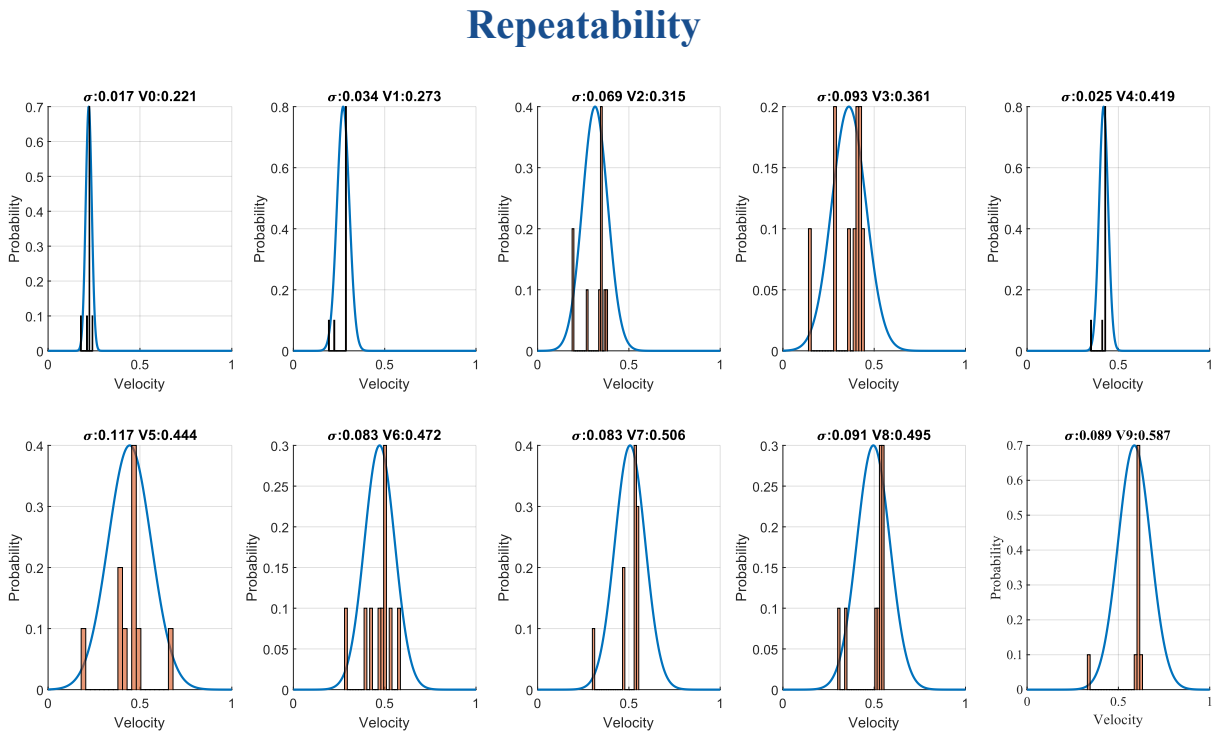

Figure 5.13: Repeatability analysis for each velocity measurement. All they had small variantion as shown in their histograms.

small variability of measurements is an assured sign of the repeatability. Also, Reproducibility is the variation that is observed when different operators measure the same part many times, using the same measurement system, under the same conditions [Zanobini et al.(2016)Zanobini, Sereni, Catelani, and Ciani]. In this research, Repeatability analysis was carried out for each velocity under the same condition as described earlier. The result are presented in Fig.5.13. All 10 repeated measurements for each out of 10 velocities had a small variation in their standard deviation. Additionally, Fig.5.10 and Fig.5.11 provide more information about the repeatability for all methods evaluated, including DCT Radon and DCT PseduCepstrum approaches.

Unfortunately, the experiments used only one camera, so reproducibility could not be evaluated as expected.

5.5 DISCUSSION

Even though Yoshida et al. worked earlier with DCT to estimate blur parameters, they did not estimate either angle or speed from a single linear motion blur. These are quite different from our Pseudo Cepstral proposal for length estimation and the proposed DCT Radon for angle estimation. Furthermore, even though other researchers have studied the way to calculate velocity from a single linear motion blur image, the aforementioned reviewed studies have not reported the use of a controlled environment and Type B standard uncertainty estimation for the velocity evaluation.

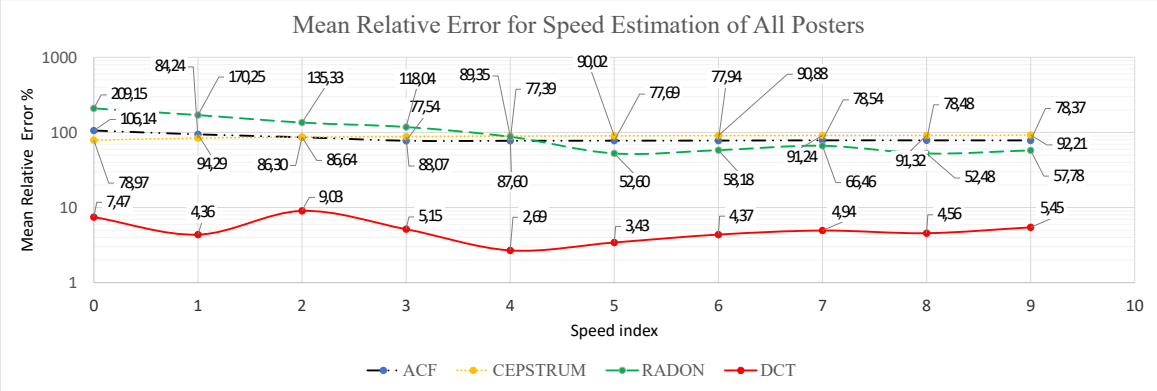

Figure 5.14: Mean Relative Error for all Posters using different methods to estimate speed at 121cm from the camera.

5.6 CONCLUSIONS

Our DCT Radon for angle estimation and DCT Pseudo Cepstrum for length estimation are the best methods to calculate the relative velocity of a camera. Mean Absolute Error for DCT Radon was narrower than evaluated competitors to estimate motion direction. Its Absolute Errors for angle were between 1.6° degrees and 9.06° degrees and its mean value was 4.66° degrees. Note that its closest rival was also DCT Hough (See Fig.5.10). Moreover, for speed estimation, the DCT Pseudo Cepstrum was once again the winner. Its Relative Error was between2.69% and 9.06% , and its Mean Relative Error was 5.15. Though ACF also had good results, its Relative Error was more disperse than the DCT approach for Speed estimation (See Fig.5.11). The DCT approach for velocity estimation is more accurate than the classic DFT method. IEEE Transactions on Instrumentation and Measurement published the results of this chapter as shown in [Cortes-Osorio et al.(2018)Cortes-Osorio, Gomez-Mendoza, and Riano-Rojas].

Chapter 6

ACCELERATION ESTIMATION

Vision-based measurement (VBM) systems are starting to become popular as an affordable and a capable alternative for scientific and engineering applications. When cameras are used as instruments, motion blur usually emerges as a recurrent and undesirable image degradation which actually contains kinematic information dismissed. This chapter presents an alternative approach to estimate relative acceleration from an actual uniformly accelerated motion blur image using homomorphic mapping to extract the characteristic Point Spread Function of a degraded image to train a machine learning regression model. A total of 125 uniformly accelerated motion blur pictures were taken in light and distance controlled environment at 5 different accelerations in a range between $0.64\text{m}/s^2$ and $2.4\text{m}/s^2$. Ensembles of Trees, Gaussian Processes (GPR), Linear, Support Vector Machine (SVM), and Tree Regression and 19 variants were evaluated to predict the acceleration. The bests RMSE result was $0.2553\text{m}/s^2$ using Linear regression with a Prediction Speed of 470 observation per second. Finally, the proposed method is a valid alternative for the estimation of the acceleration for invariant motion blur when additive noise is not dominant.

6.1 INTRODUCTION

Vision-based measurement (VBM) systems use cameras as an instrument [Shirmohammadi and Ferrero(2014)]. This emerging trend is starting to become popular as an affordable and a capable alternative for many applications such on-road vehicle detection, tracking, and behavior understanding [Beauchemin et al.(2012)Beauchemin, Bauer, Kowsari, and Cho], robotics [Motta et al.(2001)Motta, de Carvalho, and McMaster], physics [Wahbeh et al.(2003)Wahbeh, Caffrey, and Masri], biology [Karimirad et al.(2014)Karimirad, Chauhan, and Shirinzadeh] and engineering [Park et al.(2010)Park, Lee, Jung, and Myung].

The present work introduces a method to calculate acceleration from an actual uniformly accelerated motion blur image using homomorphic mapping to extract the characteristic Point Spread Function of the degraded image to train a machine learning regression model with a set of known instances and responses. It considers the motion angle equal to zero, even though the constant acceleration is obtained from an inclined slider. Acceleration measurements are highly used in control [Luh et al.(1980)Luh, Walker, and Paul], transportation [Hoberock(1977)], robotics [Lepetič et al.(2003)Lepetič, Klančar, Škrjanc, Matko, and Potočnik], physics [Sironi and Spitkovsky(2011)], sports bio-mechanics [Ohgi(2002)], geology [Xu et al.(2013)Xu, Liu, and Li], and technical [Sawicki et al.(2003)Sawicki, Wu, Baaklini, and Gyekenyesi] and medical

[Hozumi et al.(2000)Hozumi, Yoshida, Akasaka, Asami, Kanzaki, Ueda, Yamamuro, Takagi, and Yoshikawa] diagnostics.

Displacement, velocity, and acceleration are kinematics quantities related through time. It means that it is possible to obtain one from the other one just by integration or differentiation . The differential of displacement is called velocity, and the differential of velocity is acceleration. Conversely, the integral of acceleration is velocity and, if velocity is integrated, displacement is obtained [Vijayachitra and Krishnaswamy(2005)]. In a real-world application, integration is widely used due to beneficial noise attenuation. Differentiation, on the contrary, amplifies noise. Consequently, this makes acceleration all the more suitable to obtain other kinematic quantities when initial conditions are known.

There are fundamentally two classes of acceleration measurement techniques: direct and indirect measurements. The first one uses sensors, such as accelerometers, and the second one calculates acceleration from other variables, such as speed and position, using a differentiator circuit or a computational algorithm [Ovaska and Valiviita(1998)]. The ongoing proposal is, therefore, an indirect measurement approach.

6.1.1 Acceleration model for linear motion blur

The Point Spread Function (PSF) has a relevant role in the image formation theory. All optical systems have a specific PSF which intrinsically describes the degradation process of the image during its formation. For this reason, the nature of the PSF can contain information about the acceleration process.

Its nature can classify blur as Optical, Mechanic and Medium Induction blur [Chan and Shen(2005b)]. This study only considers the mechanic blur which occurs when the relative velocity among the different objects in the scene and the camera are relatively large compared to the exposure time of light sensors, so that the resulting recorded image is distorted [Lin and Li(2004a), Gunturk(2012)].

There are some approaches to obtain the PSF from a linear motion blur image. Som [Som(1971)] introduced a formulation for the Point Spread Function in the presence of accelerated motion. Even though this was actually research about image formation on light-sensitive emulsion film during its exposure, it has been a reference for some modern research due to its visionary usability in digital image processing.

Some authors have concluded that uniform acceleration causes less degradation to image compared to uniform velocity [Qi et al.(2005)Qi, Zhang, and Tan, Yitzhaky and Stern(2003), Yitzhaky et al.(1998)Yitzhaky, Mor, Lantzman, and Kopeika]. Partially, for this reason, it is more difficult to estimate the acceleration than the speed. Fig.6.2 shows the degradation process for both cases.

Equation 6.1 is the Point Spread Function model of linear uniformly accelerated motion:

$$h(x) = \begin{cases} \frac{1}{T(v_0^2 + 2\,a\,x)^{\frac{1}{2}}} & 0 \leq \mid x \mid \leq L \\ 0 & \text{otherwise} \end{cases} \tag{6.1}$$

Where a, v_o, x and T are the values of the uniform acceleration, the initial velocity, the displacement and the exposure time interval, respectively. Figure 6.1a shows the Point Spread Function for constant velocity, and Fig.6.1b for constant acceleration. Notice that Eq.6.1 becomes into Eq: 6.2 when $a = 0$ which corresponds to uniform velocity. The product Tv_o is equal to L, the blur length. Additionally, the Fourier Transform of both PSFs are depicted

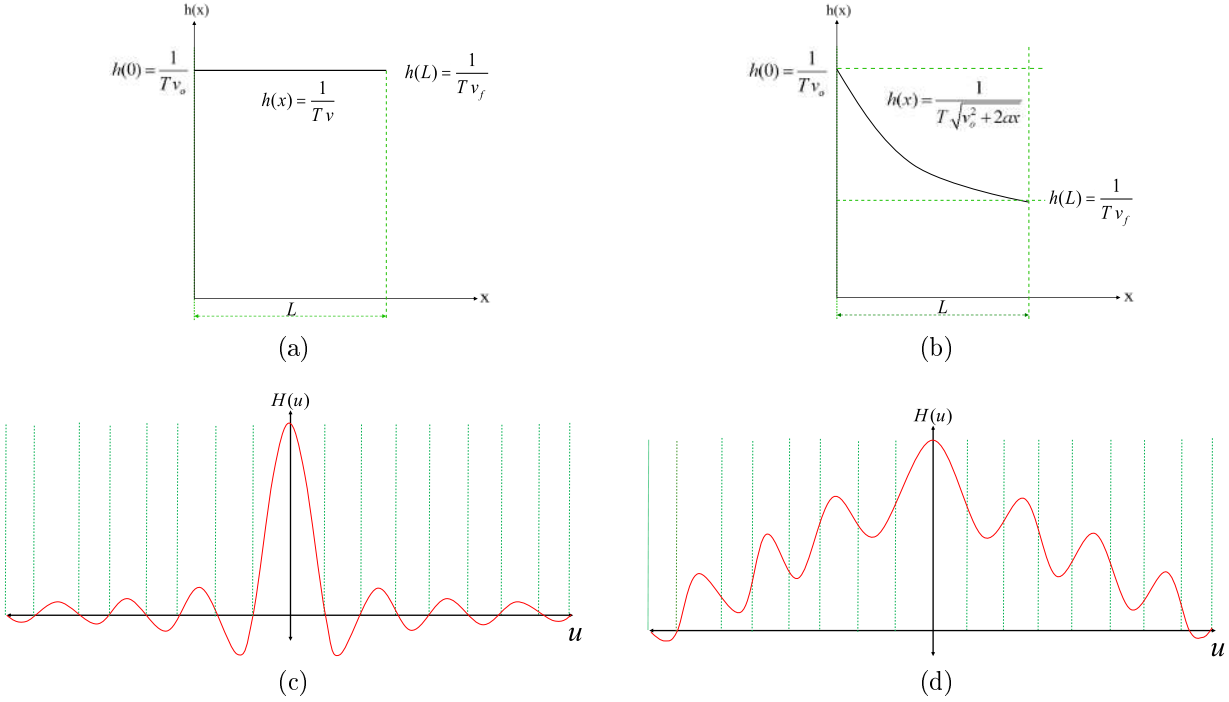

Figure 6.1: Point Spread Function for: (a) uniform velocity and (b) uniformly accelerated motion. Fourier Transform of : (c) the PSF of Uniform velocity shown in (a) and (d) Fourier Transform of uniformly accelerated motion shown in (b). These are only ilustrative examples.

in Fig.6.1c and Fig.6.1d, respectively. Notice that constant acceleration causes some blurring of the Fourier Transform of the PSF that makes difficult its extraction due to the decrement of zeros.

$$h(x) = \begin{cases} \frac{1}{Tv_o} & 0 \leq \mid x \mid \leq L \\ 0 & \text{otherwise} \end{cases} \tag{6.2}$$

6.1.2 PSF extraction for linear motion blur

Cannon [Cannon(1974)] introduced a method to restore a blurred image using nonlinear homomorphic filtering. It had the constraint of needing a set of statistically similar images to the blurred image under consideration. Finally, they concluded that their method was not wholly fruitful restoring all classes of blurred images and had some constraints. This method was not used to estimate any kinematic quantities, but it is widely related due to its usability to extract the Point Spread Function as an implicit source of characteristics.

Chen et al. [Chen et al.(1996)Chen, Nandhakumar, and Martin] pointed out in their paper that motion blur is an important visual cue for motion perception, but the usability of motion blur has been in widely neglected in image analysis research. In their study, they established a computational model that estimated image motion from motion blur information using both simulated and real blur. In their actual experiments, they used a camera mounted on an rail. They concluded that motion-from-blur was an additional tool for motion estimation, although they emphasized that a rigorous general proof was not presented in their study.

Yitzhaky and Kopeika [Yitzhaky and Kopeika(1997)] proposed a method to identify motion blur parameters which characterize the Point Spread Function (PSF). Their identification approach was based on the idea that image characteristics along the direction of motion are different from those in any other directions. They carried our experiments using blurred images that were generated by vibrating a chemical shaker horizontally and manually by the motion of the camera.

Yitzhaky and Stern [Yitzhaky et al.(1998)Yitzhaky, Mor, Lantzman, and Kopeika] proposed a method to estimate the Point Spread Function from a single interlaced frame from a video image. They denoted that when relative motion between the interlacing camera and the scene occurs during imaging, two distortion types degrade the image: the edge "staircase effect" due to shifted appearances of objects in successive fields, and blur due to scene motion during each interlaced field exposure. They assumed that the motion in each interlaced field was spatially invariant. Their method proposed to estimate the Point Spread Function of each field independently assuming constant velocity or acceleration for restoration. Even though this approach was promising, it demanded interlaced recorded images.

Yitzhaky et al. [Yitzhaky et al.(1999)Yitzhaky, Milberg, Yohaev, and Kopeika] analyzed and compared some direct methods such as homomorphic filtering for the restoration of motion blurred images. They claimed that the basic homomorphic concept is to convert the convolution process into addition and treat the transformed problem with conventional linear filtering techniques. Their approach was used to restore original uniformly accelerated motion blurred images. They concluded that due to the direct methods are relatively fast and easy to implement, they have practical importance in digital image restoration. Other authors have also used homomorphic filtering for image restoration recently as shown in [Benameur et al.(2012)Benameur, Mignotte, and Lavoie, Mattausch and Goksel(2016), Janwale and Lomte(2017)].

Perez and Rodriguez [Pérez Huerta and Rodriguez Zurita(2005)] presented the mathematical modeling for the restoration of motion blur images at constant velocity and acceleration. Also, they carried out actual experiments by using an air-rail carrier in the laboratory. One small white point painted beside a black letter, stuck on the carrier, was used to trace the Point Spread Function for its reconstruction.

Raskar [Raskar et al.(2006)Raskar, Agrawal, and Tumblin] proposed a method using a pseudo-random binary sequence so that the motion blur itself preserved decodable details of the moving object. They stated that their method simplified the corresponding image deblurring process, even though it is not fully automatic as users must specify the motion by roughly outlining this modified blurred region. They used an external liquid-crystal shutter on the lens of the digital camera for on-off control of light and exposure code. The authors concluded that the coded sequence is easy to implement, but requires camera manufacturers implement the binary switching feature directly on a sensing chip because it is not still available in any camera as a primary feature.

6.1.3 Kinematic quantities from vision-based approaches

Lin et al. [Lin and Li(2004a), Lin(2005)] proposed a method to estimate the speed of moving vehicles from single still images based on motion blur analysis for traffic law enforcement. The speed of the moving vehicle was calculated according to imaging geometry, camera parameters, and the estimated blur parameters. They reported results of less than 10% error for highway vehicle speed detection.

Celestino and Horikawa [Celestino and Horikawa(2008)] suggested an approach to measure the speed of a vehicle using a motion blur analysis. It was intended for inspection of a speedometer of automotive vehicles. The speed was determined by analyzing the characteristics and regularities contained in a single blurred image of a simulated road surface. They reported results of less than 10% error. They compared the image analysis results to ground truth values using a toothed wheel, a hall sensor, and an oscilloscope.

Pazhoumand-dar et al. [Pazhoumand-Dar et al.(2010)Pazhoumand-Dar, Abolhassani, and Saeedi] carried out their experiments for speed estimation using a toy car. They stated, in their paper, that the actual speed of the vehicle was an approximation. Furthermore, according to their report, only 10 images were used to evaluate their proposed algorithm.

Rezvankhah et al. [Rezvankhah et al.(2012)Rezvankhah, Bagherzadeh, Moradi, and Member] described a velocity estimation technique based on motion blur images using an air hockey puck. The proposed approach was implemented with an actual air hockey table, using two different cameras.

Taherkhani and Mohammadi [Mohammadi and Taherkhani(2013)] presented a speed measurement method of spherical objects using a single motion blur image taken in front of a still background. They estimated their method error by comparing it to a video-based approach. The actual speed was calculated by measuring the distance traveled between two fixed locations divided by the time difference. Other multi-frame video strategies have been used in [Luvizon et al.(2017)Luvizon, Nassu, and Minetto, Wang(2016), Kruger et al.(1995)Kruger, Enkelmann, and Rossle, Litzenberger et al.(2006)Litzenberger, Kohn, Belbachir, Donath, Gritsch, Garn, Posch, and Schraml].

Cortés-Osorio et al. [Cortes-Osorio et al.(2018)Cortes-Osorio, Gomez-Mendoza, and Riano-Rojas] presented in a previous study an alternative method for the estimation of velocity from a single linear motion blurred image. They used the Discrete Cosine transform to extract the PSF of the actual motion blur images as a basis to measure the blue extent L which is related to actual displacement. It was used in combination with the exposure time T to estimate the speed.

Li et al. [Li et al.(2008)Li, Du, Zhang, and Wang] introduced a cell segmentation and competitive survival model (CSS) merged with and into the standard techniques of particle image velocimetry (PIV). They used the algorithm with real and synthetic particle images and compared to particle correlation velocimetry and recursive PIV approaches.

Alternatively, Sederman et al. [Sederman et al.(2004)Sederman, Mantle, Buckley, and Gladden] introduced a magnetic resonance imaging (MRI) technique for measurement of velocity vectors and acceleration in a turbulent flow.

McCloskey et al. [McCloskey et al.(2012)McCloskey, Ding, and Yu] used code exposure for accurate reconstruction of motion blur images. They used statistical blur estimation providing accurate motion estimates for constant velocity, constant acceleration, and harmonic rotation in real images. They captured accelerated motion images using a toy car on an tilted track, where gravity provided acceleration. The camera was rotated so that the motion turned up almost horizontal. They validated their motion estimation method by the quality of the deblurred results. Their study was based on [Agrawal et al.(2009)Agrawal, Xu, and Raskar].

Weems et al. [Leifer et al.(2011)Leifer, Weems, Kienle, and Sims] evaluated the feasibility of multi-point, non-contact, acceleration measurement, a high-speed, precision videogrammetry system assembled from commercially available components and software. They used three scan CCD cameras at 200 frames per second to carried out the measurements. Finally, they concluded that their results are comparable to those obtained using accelerometers. In addition, Liu and

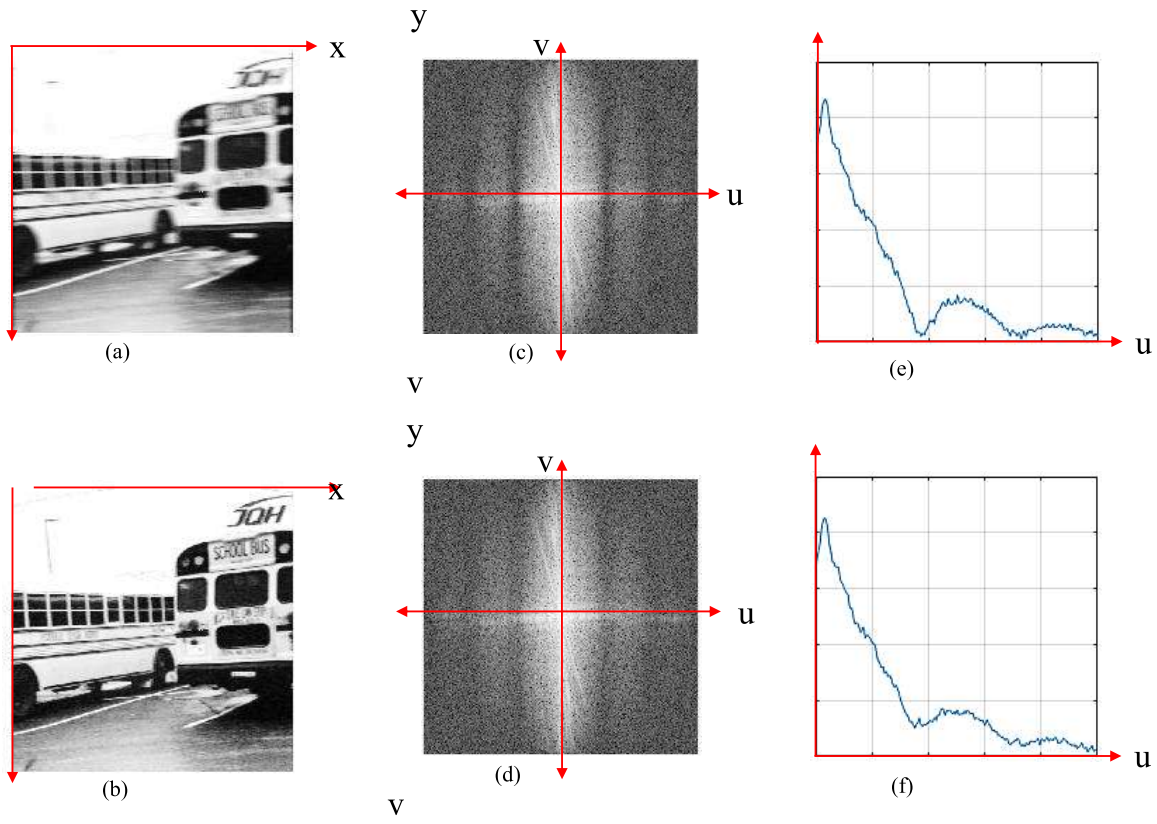

Figure 6.2: Differences between a degraded image with uniform motion blur and uniformly accelerated motion blur. (a) Invariant Motion blurred image due to constant velocity. Blur is evident. (b) Invariant Motion blurred image due to constant acceleration. Blur is minor. (c) Modulation Transfer Function of image shown in (a). (d) Modulation Transfer Function of image shown in (b). (e) Collapsed MTF on u-axis of (c). (f) Collapsed MTF on u-axis of (d).

Katz [Liu and Katz(2006)] described a non-intrusive technique for measuring the instantaneous spatial pressure distribution over a sample area in a flow field using Particle Image Velocity (PIV). This is a well-known vision-based method for speed and acceleration estimation based on optical flow method using two images taken at a high frame rate. Some additional studies in PIV for acceleration measurement are introduced in [Chu et al.(2018)Chu, Wolfe, and Wang, Chen et al.(2016)Chen, Li, Zhao, Huang, and Guo].

6.1.4 Related machine learning works

Dong et al. [Dong et al.(2010)Dong, Song, Wang, Zeng, and Wu] used Support vector machines (SVM) regression to predict water flow velocity based on an improved hydrodynamic model. They stated, in their paper, that no publications were available regarding using SVM to predict marine environment elements related to hydrodynamic. Even though they asserted that their approach was not completely successful as expected, it was promising and useful for future research.

Genc et al. [Genç and Dağ(2016)] suggested a method for the determination of velocity profile in small streams by employing powerful machine learning algorithms such as artificial neural networks (ANNs), support vector machines (SVMs), and k-nearest neighbor algorithms (k-NN). These comparative results revealed that k-NN algorithms overcome the other regression

alternatives evaluated.

We organized the remainder of this chapter as follows. Section 6.2 introduces the proposal to acceleration estimation using Machine Learning and the PSF as a source if characteristics. Then, Section 6.3 presents the rig set-up, and the experiments carried out to estimate the acceleration from a single uniformly accelerated motion blur image. After, Section 6.4 depicts the results obtained in the experiments by comparing different regression approaches and metrics. Finally, Section 6.5 contrast the results with previous authors and tells about the constraints and benefits of this proposal. Finally, in Section 6.6, draws the most remarkable conclusions.

6.2 ACCELERATION ESTIMATION PROPOSAL

Firstly, $G(x, y)$ is the degraded blur image, $I(x, y)$ is the blur-free image, and $H(x, y)$ represents the degradation kernel (PSF). If noise of any kind is not added and the blur system, it is considered linear and stationary, then the process can be described as seen Eq.6.3:

$$G(x, y) = I(x, y) * H(x, y) \tag{6.3}$$

The product $*$ is the convolution in two dimensions. Additionally, image convolution from Eq.6.3 can be also represented as an integral as shown in 6.4:

$$I(x, y) * H(x, y) = \int_{-\infty}^{+\infty} \int_{-\infty}^{+\infty} I(x', y')H(x - x', y - y')dx'dy' \tag{6.4}$$

Since it is always about finite blur images in space, Eq.(6.4) is defined in the interval $[x_2 - x_1\ ,\ y_2 - y_1]$ and in the rest of its domain is zero. It should be noted that the convolution interval must be much larger than the PSF interval of the blur.
Now, the Discrete Fourier Transform (DFT) is applied on both sides of Eq.6.3 to obtain Eq.6.5 which represents a point-wise multiplication in frequency instead of a convolution in space.

$$G(u, v) = I(u, v)\, H(u, v) \tag{6.5}$$

Equation 6.5 is complex in nature, so it can also be written in polar coordinates using magnitude and angle as seen in Eq.6.6.

$$\mid G(u, v) \mid e^{j\angle G(u,v)} = \mid I(u, v) \mid e^{j\angle I(u,v)} \mid H(u, v) \mid e^{j\angle H(u,v)} \tag{6.6}$$

The preceding relation can be split into magnitude and phase components as shown in Eq.6.7 and Eq.6.8, respectively.

$$\mid G(u, v) \mid = \mid I(u, v) \mid\mid H(u, v) \mid \tag{6.7}$$

$$e^{j\angle G(u,v)} = e^{j\angle I(u,v)} e^{j\angle H(u,v)} \tag{6.8}$$

$$\log \mid G(u, v) \mid = \log \mid I(u, v)\, H(u, v) \mid$$

Only the log magnitude portion of the complex logarithm of the Discrete Fourier transform is used. See Eq.6.9.

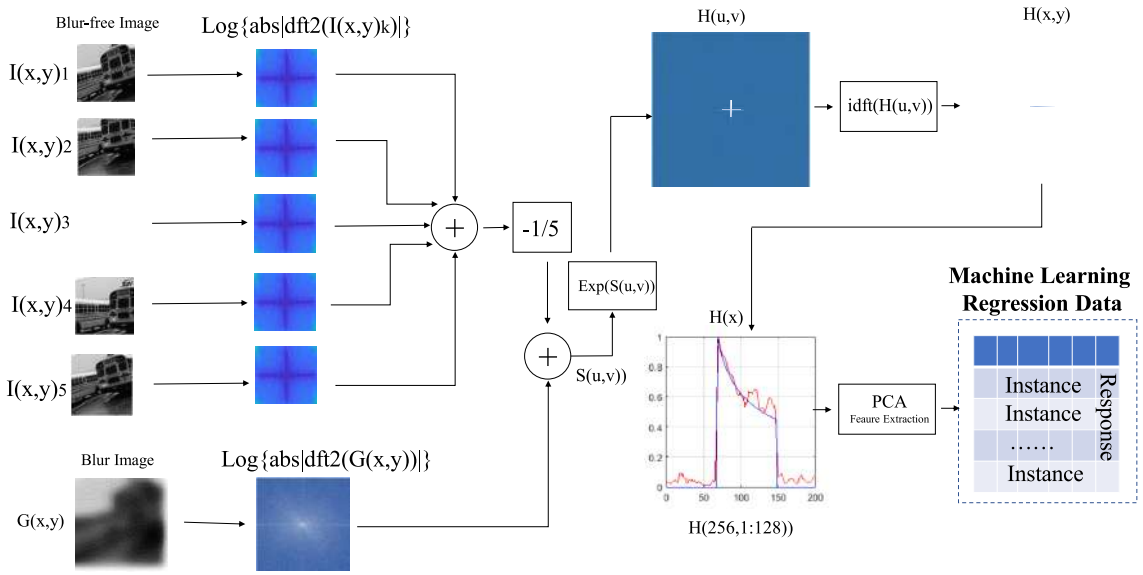

Figure 6.3: Process to estimate acceleration using homomorphic method to extract the PSF and machine learning regression.

$$\log \mid G(u,v) \mid = \log \mid I(u,v) \mid + \log \mid H(u,v) \mid \tag{6.9}$$

Although some images can be clearly very different in space, their average log spectrum in frequency usually are very much alike and almost indistinguishable to the naked eye from each other. This allows to use some hypothetical images $I(x,y)_k$ to estimate the prototype clear blur-free image [Cannon(1974)]. Then, it can be written as seen in Eq.6.10. Additionally, the average of the log spectrum for all Q non-degraded background images is used to have an hypothetical blur-free image.

$$\log \mid P \mid = \frac{1}{Q} \sum_{k=1}^{Q} \log \mid I(u,v)_k \mid \tag{6.10}$$

and consequently,

$$\mid H(u,v) \mid \approx \exp \left[\log \mid G(u,v) \mid - \frac{1}{Q} \sum_{k=1}^{Q} \log \mid I(u,v)_k \mid \right] \tag{6.11}$$

$$\mid H(u,v) \mid \approx \exp \left[\log \mid G(u,v) \mid - \log \mid P \mid \right] \tag{6.12}$$

where $\mid H(u,v) \mid$ is the Modulation Transfer Function (MTF) of an arbitrary blur. It can be estimated without knowledge of the image using a set of reference images to generate a prototype average log spectrum.

Finally, we can find the Inverse Fourier Transform ($iDFT$) of $H(u,v)$ to obtain $H(x,y)$, the PSF.

$$h(x,y) = iDFT(H(u,v)) \tag{6.13}$$

Even though the classic approach for the PSF estimation of an image uses images statistically close to generate the Prototype average log spectrum, this research used 5 still background images that can be used as the clear image to estimate the MTF.

Figure 6.3 presents the proposed method for the estimation of the acceleration using homomorphic filtering and machine learning regression. Five blur-free images $I(x,y)_k$ are taken to the fixed background with the camera at rest. it helps reduce additive noise in some way, subtracting the average of a set of hypothetical blur-free images. Consecutively, the (MTF) is obtained for each of the 5 images and then averaged, summing and dividing them by 5. It generates a prototypeblur-free background $log \mid P \mid$ which is subtracted from the MTF of the motion blurred image $\log \mid G(u,v) \mid$ to obtain the output $S(u,v)$. Later, the exponential function is used to remove the logarithm. It allows to obtain the Optical Fourier Transform $H(u,v)$ of the blurred image that leads to the Point Spread Function $H(x,y)$ in two-dimensions using the inverse Fourier Transform. Due to the motion is only in the horizontal axis, the actual PSF is also in one dimension $H(x)$ can be obtained from the central horizontal line of the PSF $H(x,y)$. Prior to training, the instances are space-reduced using PCA to avoid redundancy. Finally, a set of uniformly accelerated motion blur images of known acceleration is used for training.

6.3 MATERIALS AND METHODS

The experiments presented in this section were carried out to estimate acceleration from a single uniformly accelerated motion blur image using homomorphic filtering to extract the PSF, and machine learning to predict the actual Response. Firstly, all parts of the rig set-up are introduced to give a more precise description of the procedure. Then, an overview of the machine learning methods used is presented, and finally, the evaluation metrics are described for the regression methods assessed.

6.3.1 The Rig set-up parts

Here describes the materials and the laboratory equipment needed in the experiments. Some of these were specifically constructed for this study.

6.3.2 The slider

A 185-cm-long aluminum slider was constructed for previous speed experiments, as shown in [Cortes-Osorio et al.(2018)Cortes-Osorio, Gomez-Mendoza, and Riano-Rojas], and slightly modified for acceleration. Figure 6.5 presents all the parts included to operate the capture system. Five different pattern Posters (1) were used (one at a time), located at a 171-cm fixed parallel distance from the rig. Figure 6.4 shows all five pattern posters used to carry out these acceleration experiments. Two Leveling Rubber Feet (2) with threaded studs were set under each one of the two-rod insertion supports. Additionally, a Digital Pitch Gauge (3) was mounted on the Camera Sliding Carriage Platform (4), to measure the tilt angle, as well as the Camera (5), respectively, to measure any needed angle. Constant acceleration of the Sliding Carriage Platform was set by raising an end of the slider to one of the 8 possible preset angles of acceleration marked on the Lifting Base (6), however, only five were used (A1, A2, A4, A5, and A7) listed in Table 6.1. The Controller (7) read the date from sensor in (11). The

(a) University. (b) Bus. (c) UTP. (d) City. (e) Flag.

Figure 6.4: Pattern posters used to carry out the acceleration experiments.

camera Platform was pulled manually to the upper position of Lifting Base and then released to slip freely on the two oiled stainless Steel Rods (8) which lay on four Low Friction Linear Bearings (9). The Sliding Platform also had an Laser-Cut Toothed Steel Sheet attached (10), used to to take a single picture when its first tooth reached the Slotted Optical Switch Sensor of the Camera Trigger (11), to measure and send the obstruction time per each tooth to the Controller (7). When the camera was activated by the Camera Trigger pulse, the digital image (snapshot) was sent to the Image Capture Computer (12) through the USB 2.0 wiring. Finally, the result obtained from a single motion blur image were compared to the actual acceleration value estimated by the wireless (Bluetooth) Data Analysis Computer (13). Figure 6.6 presents the actual rig setup used to carry out the experiments to generate uniformly accelerated motion blur images in the laboratory.

6.3.3 The computers

The motion blur image capture and processing computer was a 64 bit desktop computer, Core I3 processor, 2GB of RAM. Additionally, a 64 bit laptop computer, AMD A3 processor, 2GB of RAM was used for data analysis of acceleration received from the controller system. Both had Windows 7 operating system and were running Matlab 2017b.

6.3.4 The images

The experiments were carried out in a controlled environment. A digital scientific camera (Basler acA2000-165um USB 3.0) [Basler(2017)] was used to take the pictures, the Artificial white light from led panel lamps was about 255 Lux, the distance to pattern poster was set at 171 cm, the maximum exposure time of camera was 100ms, the slider acceleration was between $0.6\text{m}/s^2$and $2.40\text{m}/s^2$, and the aperture of the lens' diaphragm (Ricoh lens FL-CC0814A-2M) [Ric(2017)] was set at F/4.

The images were taken for five different pattern posters as shown in Fig.6.4. Then, they were cropped at 512×512 pixels for image size and converted to 8-bit grayscale following recommendation 601 from the International Telecommunication Union [bt6(2017)]. The posters were shot from a point of view parallel to the pattern poster and the camera slider motion line. This experiments considered the angle of motion at zero degrees. Although the camera slided on inclined plane platform, motion blur was horizontal with respect to the camera angle. The pattern posters were not rotated, so at naked eye, these looked crooked. See Fig.6.5 to find each element described.

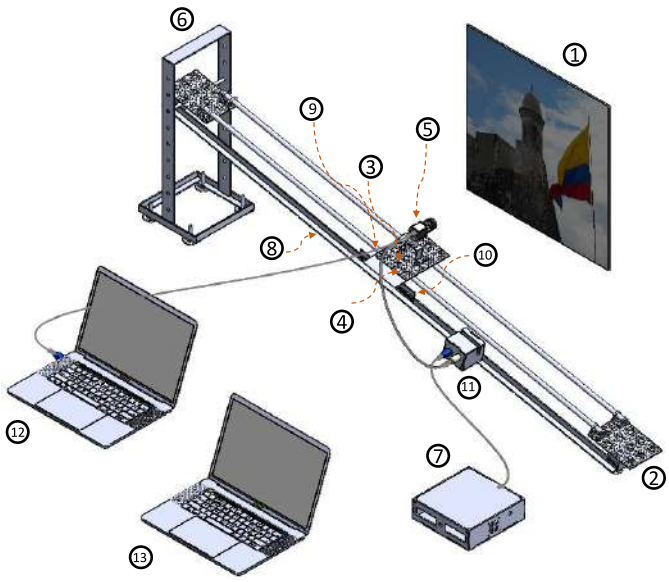

Figure 6.5: Complete rig setup model to capture uniformly accelerated motion blur images. (1) Pattern Poster, (2) Leveling Rubber Feet, (3) Digital Pitch Gauge, (4) Camera Sliding Carriage Platform, (5) Camera, (6) Lifting Base, (7) Controller, (8) Stainless Steel Rods, (9) Low Friction Linear Bearings, (10) Laser-Cut Toothed Steel Sheet, (11), Camera Trigger, (12) Image Capture Computer, and (13) Data Analysis Computer.

6.3.5 PCA feature extraction

Feature extraction is a relevant topic in signal processing mostly due to the high dimensionality of data and its redundancy [Izquierdo-Verdiguier et al.(2014)Izquierdo-Verdiguier, Gomez-Chova, Bruzzone, and Camps-Valls]. Principal Component Analysis (PCA) is a classical statistical approach widely used for feature extraction in pattern recognition and computer vision [Bouwmans et al.(2018)Bouwmans, Javed, Zhang, Lin, and Otazo]. In this study, PCA feature extraction is used to reduce redundant data from the extracted PSF. The multidimensional space was transformed from 125 to 76 characteristics.

6.3.6 Machine Learning Regression

Five different approaches were used to predict the acceleration from the Point Spread Function data of actual motion blurred images observed. Ensembles of Trees, Gaussian Processes (GPR), Linear, Support Vector Machine (SVM), Tree Regression and their variations were evaluated as presented in Table 6.2.

6.3.7 Regression Model Evaluation

The metrics used to evaluate the regressions were Root Mean Square Error (RMSE), R-Squared, Mean Squared Error (MSE), Mean Absolute Error (MAE), Prediction Speed in observation per second, Training Time in seconds, and R-Squared (Coefficient of Determination). Also Predicted vs Actual, Residuals Plot, and Response Plot were employed for the best three approaches.

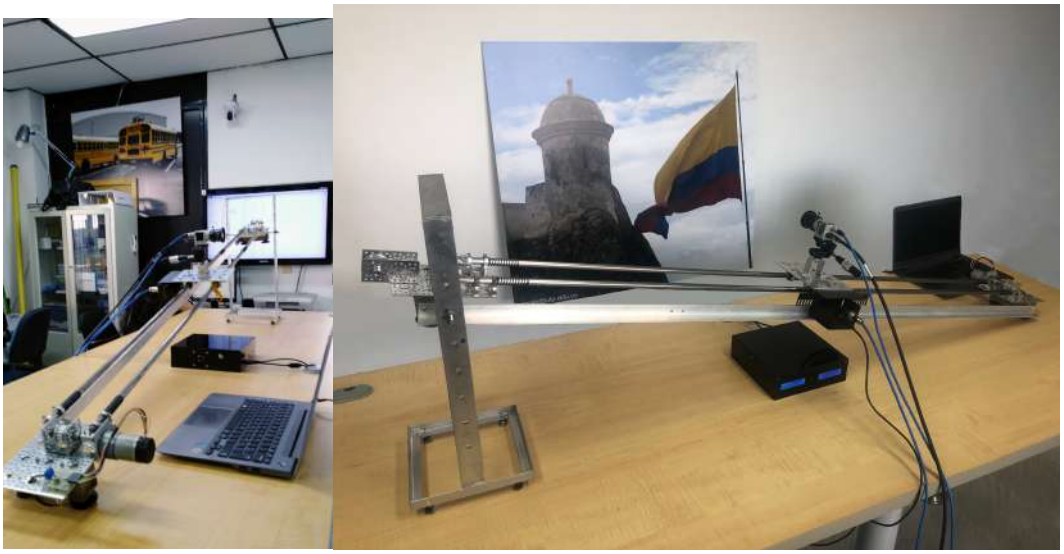

(a) (b)

Figure 6.6: Actual rig setup to generate uniformly accelerated motion blur images.

6.4 EXPERIMENTAL RESULTS

Five pictures were taken for each preset accelerations, to obtain a total of 125 sample motion blur images (5 accelerations × 5 images per acceleration × 5 image poster) for acceleration estimation experiments using machine learning.

Index	Angle (Degree)	Acceleration (m/s^2)
A0	15°	2.4630 ±0,0285
A1	13.3°	2.1782 ±0,0233
A2	10.1°	1.5416 ±0,0161
A3	7.9°	1.2292 ±0,0130
A4	4.5°	0.6448 ±0,0074

Table 6.1: Preset accelerations of the camera slider with its uncertainty.

Even though the slider accelerations were repeatable and close to the those shown in Table 6.1, we used each individual reading of the Controller to assess the error between its actual value and the vision-based value.

6.4.1 The instrument calibration

The system of uniformly accelerated motion had an Arduino Nano microcontroller, which was responsible for measuring the time it took to block each of the teeth of the Toothed Steel Sheet used. Its operation consisted of allowing to slide the Camera Carriage Platform on the Steel Rods at five different angles, which produced different accelerations depending on the height. The angles and their accelerations in Table 6.1.

The calibration was performed by measuring the acceleration with both the controller system and with the Phywe Cobra4 Sensor-Unit 3D-Acceleration (±2g and Resolution of 1mg) standard

instrument using the Cobra4 Wireless-Link [GmbH(2018)] to transmit the acceleration data. The combined uncertainty and the sensitivity coefficients of the variables were calculated to obtain the total expanded uncertainty of the measurements.

6.4.2 The data acquisition results

Five folds were used for the validation of all regression models proposed. Table 6.2 shows the results for the basic evaluated regression models and their variants. Even though only five different main approaches were evaluated, each one had a subset of variants, for a total of 19. The bests RMSE results were GPR (Matern 5/2) and Linear (Linear) with 0.2547 m/s^2 and 0.2553 m/s^2, respectively. On the other hand, Linear regression is simpler to code and faster, in terms of observation per second, than its closer competitors. Linear regression, GPR (Matern 5/2) and SVM (Quadratic) were able to perform 470 obs/s, 530 obs/s and S 540 obs/s, respectively. See table 6.2.

Additionally, Predicted vs Actual Plot, Residuals Plot, and Response Plot were plotted for the best five RMSE results of each regression model. Residuals Plot for GPR (Matern 5/2), Linear (Linear), and SVM (Quadratic) in Figs.6.7b, 6.8b, and 6.9b, respectively, allowed to find out that the acceleration residuals trend to change their sign value, from negative to positive, when acceleration is upper 1.4 m/s^2.

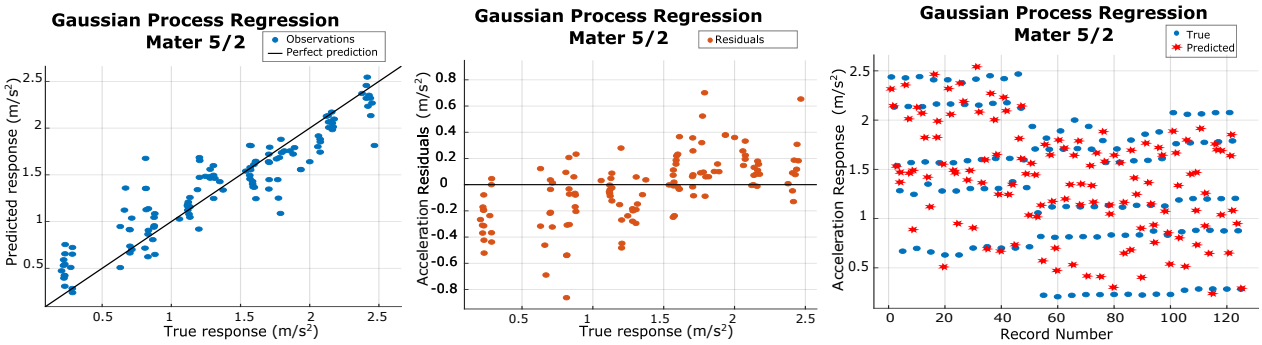

(a) (b) (c)

Figure 6.7: Matern 5/2 Gaussian Process Regression Results. (a) Predicted vs Actual Plot for Gaussian Process Regression Matern 5/2, (b) Residuals Plot for Gaussian Process Regression Matern 5/2, and (c) Response Plot for Gaussian Process Regression Matern 5/2.

In addition, Acceleration Residuals are smaller in all cases when acceleration is above 1.0 m/s^2. In consequence, this makes linear regression more suitable for real-time applications. Finally, it can be seen that all plots for Gaussian Process Regression (Mater 5/2), in Fig.6.7, and Linear Regression, in Fig.6.8, are almost identical.

Boosted Trees method was the best approach for Ensembles of trees. However, its results are not the best when compared to the other approaches. See Fig.6.10. Similarly, Trees method, and its variant called Medium, did not give satisfactory results as shown in Fig.6.11 and Table 6.2.

Regression Models		RMSE (m/s^2)	R-Squared	MSE (m/s^2)^2	MAE(m/s^2)	Prediction Speed (Obs/s)	Training Time (s)
Ensembles of Trees	Bagged Trees	0.4124	0.60	0.1701	0.3396	420	1.7598
	Boosted Trees	0.3507	0.71	0.1230	0.2452	480	1.8514
GPR	Exponential	0.3187	0.76	0.1016	0.2501	460	1.4044
	Matern 5/2	*0.2547*	*0.85*	*0.0649*	*0.1921*	*530*	1.373
	Rational Quadratic	0.2553	0.85	0.0652	0.1924	530	1.6424
	Squared Exponential	0.2553	0.85	0.052	0.1924	470	1.5473
Linear	Interactions Linear	0.3371	0.74	0.1136	0.2378	65	12.716
	Linear	*0.2553*	*0.85*	*0.0652*	*0.1978*	*470*	1.5175
	Robust Linear	0.2558	0.85	0.0654	0.1993	470	1.7325
	Stepwise Linear	0.2956	0.80	0.0874	0.2251	490	17933
SVM	Coarse Gaussian	0.6607	-0.02	0.4366	0.5669	510	1.0678
	Cubic	0.3256	0.75	0.106	0.2764	540	1.0563
	Fine Gaussian	0.4611	0.51	0.2126	0.3532	480	1.0486
	Medium Gaussian	0.5243	0.36	0.2749	0.4265	500	1.0921
	Linear	0.3747	0.67	0.1404	0.3043	500	1.0779
	Quadratic	*0.2843*	*0.80*	*0.0866*	*0.2446*	*540*	1.804
Trees	Coarse tree	0.6327	0.07	0.4003	0.5279	570	0.9837
	Fine tree	0.4915	0.44	0.2416	0.3202	540	1.0379
	Medium tree	*0.4604*	*0.51*	*0.2112*	*0.3416*	*540*	1.0037

Table 6.2: Machine learning results using Ensembles of Trees, Gaussian Processes (GPR), Linear, Support Vector Machine (SVM), and Tree Regression and their variants.

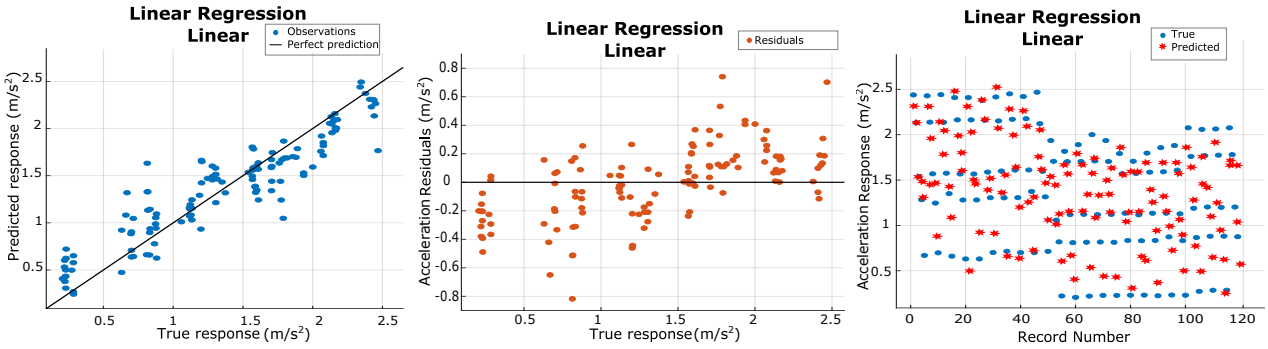

(a) (b) (c)

Figure 6.8: Linear Regression Results. (a) Predicted vs Actual Plot for Linear Regression, (b) Residuals Plot for Linear Regression, and (c) Response Plot for Linear Regression.

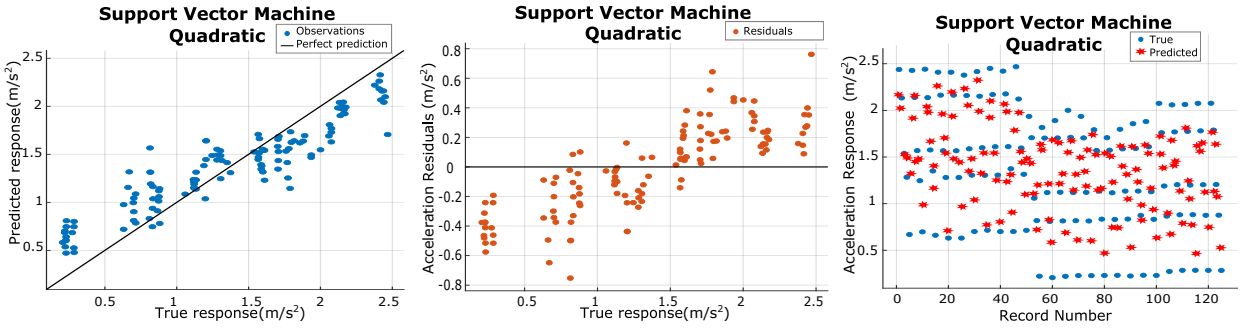

(a) (b) (c)

Figure 6.9: Quadratic Regression SVM Results. (a) Predicted vs Actual Plot for SVM Quadratic Regression, (b) Residuals Plot for SVM Quadratic Regression, and Response Plot for SVM Quadratic Regression.

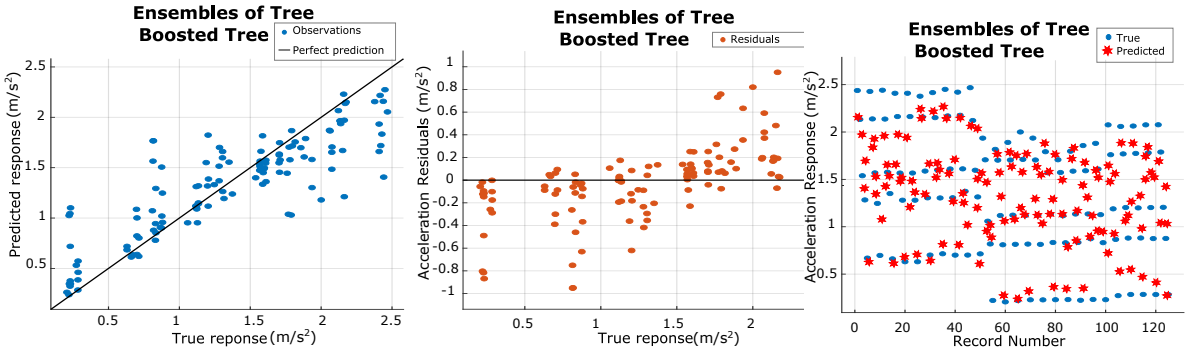

(a) fig:Booted-Ensembles-of-Ensembles-PvR (b) fig:Booted-Ensembles-of-Ensembles-Residuals (c) fig:Booted-Ensembles-of-Ensembles-Response

Figure 6.10: Boosted Ensembles of Trees Regression Results. (a) Predicted vs Actual Plot for Boosted Tree Regression, (b) Residuals Plot for Boosted Tree Regression, and (c) Response Plot for Boosted Tree Regression.

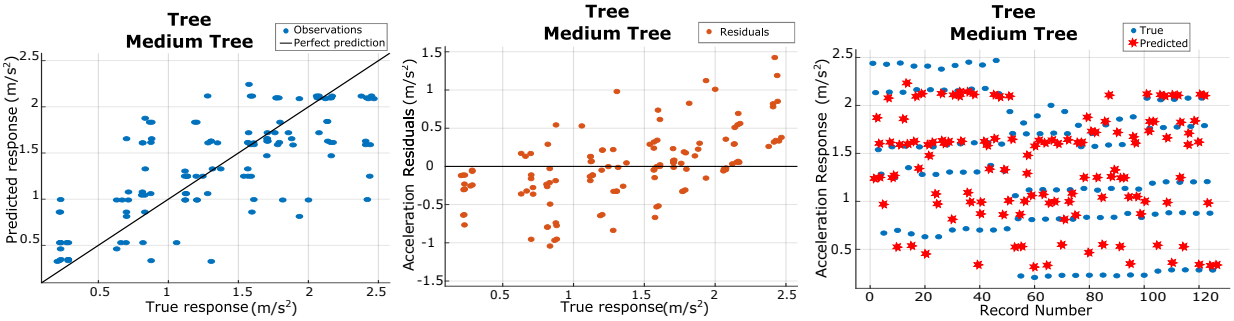

(a) (b) (c)

Figure 6.11: Medium Tree Regression Results. (a) Predicted vs Actual Plot for Medium Tree Regression, (b) Residuals Plot for Medium Tree Regression, and Response Plot for Medium Tree Regression.

6.5 DISCUSSION

Even though there are some studies to estimate the speed using vision-based measurement (VBM), only a few of them are for the measurement of acceleration, as we could determine in published scientific literature consulted. Likewise, there is no evidence of similar studies that estimate acceleration from a motion blurred image.

Some approaches have been introduced to measure the acceleration, and all they need at least two consecutive image frames to calculate it [Li et al.(2008)Li, Du, Zhang, and Wang,Sederman et al.(2004)Sederman, Mantle, Buckley, and Gladden,Liu and Katz(2006)]. Additionally, others also use high speed or multiple cameras [Komiya et al.(2011)Komiya, Kurihara, and Ando,Leifer et al.(2011)Leifer, Weems, Kienle, and Sims]. These make classical solutions more expensive and bulky.

This alternative method based on blur has benefits. Motion blur is usually an undesirable degradation that occurs, but it is possible to take advantage of it. It allows to use degraded images instead of dismissing them to calculate the acceleration. Besides, this approach can be used with low-cost cameras, instead of high-speed cameras that are more expensive.

Likewise, the proposed method has some constraints. One is it needs a set of blur-free images, however, in some cases, it is easy to obtain from the fixed background. Noise is another limitation in this proposal. When the noise is dominant instead of the blur, the extraction of the PSF can fail and therefore the estimation of the acceleration.

6.6 CONCLUSIONS

Machine learning model successfully estimates with some degree of accuracy relative acceleration from a single motion blurred image using homomorphic filtering to extract the characteristics of the Point Spread Function (PSF) which depends on initial velocity, acceleration and exposure time parameters as shown in Eq.6.1.

The proposed method is a valid alternative for the estimation of the acceleration for invariant motion blur. The best machine learning methods were GPR (Matern 5/2) and Linear (Linear) with 0.2547 m/s^2 and 0.2553 m/s^2 absolute error, respectively. GPR (Matern 5/2) and Linear regression were able to perform 530 obs/s and S 470 obs/s, respectively. Finally, the best

results are obtained when acceleration is above $1.0\,\mathrm{m}/s^2$. It makes these method an alternative approach that can be used in real-time applications.

Chapter 7

LENGTH ESTIMATION IN SPACE-VARIANT BLUR

7.1 INTRODUCTION

In this chapter, we introduce a proof of concept to ensure that spatially variant motion blur also allows estimating blur length using the proposed DCT method. As mentioned in the previous chapter 5, blur length L and exposure time T are needed to calculate relative speed from invariant motion blur images. To perform length estimation only the appropriate segmentation of the motion blurred area is required. However, there exist some constraints to consider.

Variant motion blur occurs when the camera is located in a fixed place, the background is sharp, and an object is moving in front of the camera during the exposure time. When all that happens, the central problem is how to estimate the speed of a single object using a partially blurred image. We introduce a set of synthetic experiments to evaluate the tolerance of the proposed DCT method to estimate blur length using a partial linear motion blurred image.

7.1.1 Variant Blur

As mentioned earlier, blur is the image region that is not completely distinguished due to the significative vanishing of sharp details and edges. This can be seen through the reduction of high frequency content in the image.

Motion blur can also be classified into two categories depending on spatial distribution on image: spatially invariant motion blur, in which the trace is generated in the same direction and length over the full image, and spatially variant motion blur, characterized by different motion blur directions and lengths on the image (See Fig.7.1).

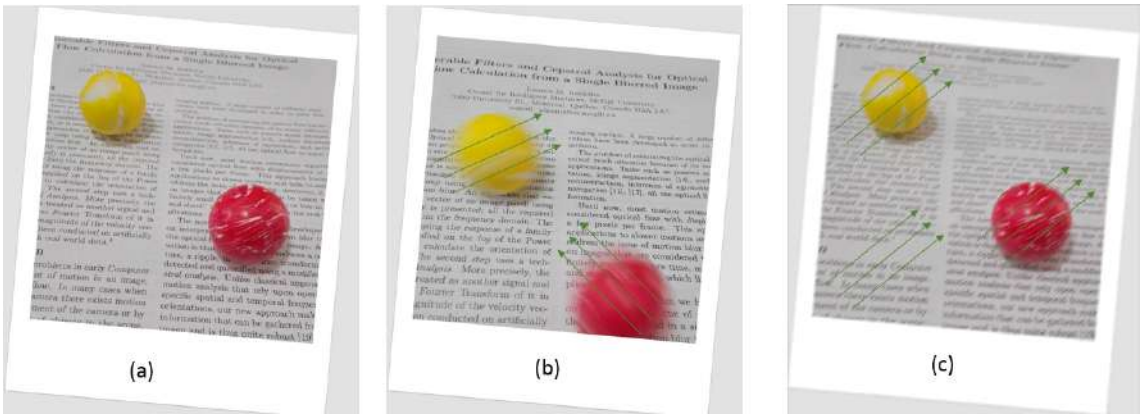

Figure 7.1: (a) Blur-free image (b) is a spatially variant motion blurred image and (b) is a spatially invariant motion blurred image .

Assuming a static and a distant scene, and ignoring the effects of defocus and lens aberration at each point, Motion blur can be modeled through Eq.7.1, where $I(x, y)$ is the blur-free image, $g(x, y)$ is the blur image and $n(x, y)$ is the additive process noise present on the image [Rajagopalan and Chellappa(2014)].

$$g(x,y) = \int\int I(\alpha,\beta)h(x-\alpha, y-\beta)d\alpha d\beta + n(x,y) \tag{7.1}$$

From Eq.7.1, the case when the PSF does not change at each position in the entire image, so that $h(x-\alpha, y-\beta) = h(\alpha, \beta)$, it is called spatially Invariant Point Spread Function. Conversely, if the function varies in space, then it is called a spatially Variant Point Spread Function *[Lin and Li(2004b), Šorel and Flu(2008)]* (See Eq.7.2).

$$g(x,y) = \int\int f(\alpha,\beta)h(x-\alpha, y-\beta, \alpha, \beta)d\alpha d\beta + n(x,y) \tag{7.2}$$

This work only considers the mechanic blur that happens when the corresponding speed among the distinctive elements in the setting and the camera are relatively large compared to the exposure time. Then, the distortion acquired by the image is called motion blur [Lin and Li(2004a), Gunturk(2012)] [Chan and Shen(2005a)]. The Point Spread Function $h(x, y)$ of any blur kernel has to satisfy three constraints, namely [Bovik(2010)]:

- $h(x, y)$ cannot take negative values due to the physics of the underlying image formation process.
- $h(x, y)$ is real-valued because images are real-valued.
- Energy is neither absorbed nor generated during the image formation process. For spatially continuous blurs, $h(x, y)$ is constrained to satisfy Eq.7.3.

$$\int_{-\infty}^{+\infty}\int_{-\infty}^{+\infty} h(x,y)dxdy = 1 \tag{7.3}$$

(a) (b)

Figure 7.2: Segmentation for real images based on Zhou algorithm [Zhou and Zhang(2018)]. (a) Variant motion blur image with fixed background and vehicles in motion. (b) Segmentation result of image shown in (a).

7.1.2 Segmentation Approaches

There are some approaches to segmenting spatially-varying blur images whose background scene is sharp, and the front object is moving. Some methods are based on optical flow, such as [Sengar and Mukhopadhyay(2017)], and others in features [Liu et al.(2008)Liu, Li, and Jia, Zhou and Zhang(2018)]. These are not discussed extensively in this work because it is not the core part of the study. Nonetheless this, we introduce some aspects that have to be considered when segmenting spatially variant motion blur in an image to estimate the relative speed of the moving object. Fig.7.2 depicts an example of motion blur segmentation using the algorithm proposed by [Zhou and Zhang(2018)]. Note that segmentation edge of the window is sharp.

When a specific motion blurred area is segmented, appears undesirable artifacts such as lines at the center of the MFT of the image due to the sharp cutoff of the window in space. This segmentation window has correctly defined edges that also introduce leakage. Unfortunately, these artifacts cannot be removed entirely, but reduced by applying an appropriate window function to the full image or the segmented blurred area edges. This effect is perfectly visible in the Cosine Transform domain as shown in Fig.7.3. We highlight that all segmentation methods, in the scientific literature we reviewed, do not consider smoothed filter edges.

7.2 MATERIALS AND METHODS

These synthetic experiments evaluated how tolerant was the proposed DCT method to estimate length using a variant motion blur image. In this case, the background was assumed to be sharp, and the moving object was synthetically blurred at a constant linear speed. The Baboon image was used from The USC-SIPI image database (University of Southern California - Signal and Image Processing Institute) [sip(2017)]. Additionally, the image size selected was 256×256 pixels with 8 bits/pixel depth and converted to grayscale following recommendation 601 from the International Telecommunication Union [bt6(2017)]. Matlab 2018b and its image processing

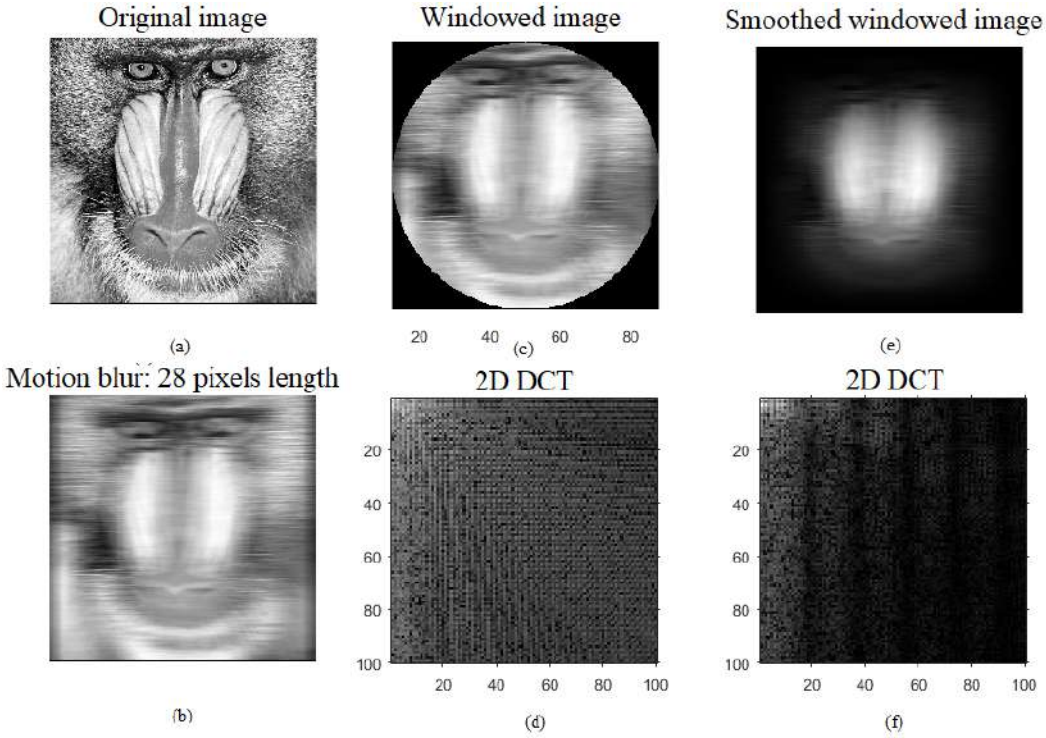

Figure 7.3: Simulation of motion blur image segmented using a sharp and smoothed window. (a) blur-free image, (b) Uniformly motion blur image, (c) Sharp windowed image, (d) DCT of sharp windowed image, (e) Smoothed windowed image using Hanning and (f) DCT of smoothed windowed image.

toolbox were used to carry out the experiments. Baboon was synthetically linear motion blurred with the length of 5 to 90 pixels at zero degrees (horizontally).

Subsequently, the image was segmented using a Hanning window of 256×256 pixels and consecutively, the height was reduced in steps at values of 128, 64, 32, 16, 8, and 2 pixels. The width was fixed to 256 long in all cases.

7.3 EXPERIMENTAL RESULTS

Figure 7.3 depicts the simulation results of the motion blur Baboon segmented using a sharp and a smoothed window. Additionally, Fig.7.3(a) and 7.3(b) present a blur-free image and a blurred image, respectively. Similarly, Fig.7.3(c) is a sharp circular windowed image of 256×256 pixels and its Discrete Cosine Transform is shown in 7.3(d). Notice this one does not have the lines that usually motion blur adds to the transformation whose separation is inversely proportional to the blur length. In contrast, Fig.7.3(e) shows the Baboon image applying a Hanning window of the same size. Conversely, the results are much better. In this case, the Cosine Transform pattern is clearer and finer. The lines added by motion blur motion are visible to the eyes as seen in Fig.7.3(f).

When the length of blur was evaluated using the sharp segmentation window, the results were the worst. In all cases, the Relative Error was above 100% as shown in Fig.7.4.

On the other hand, when the Hanning window was used, the Relative error results were below 2%, as as it is evident in Fig.7.5.

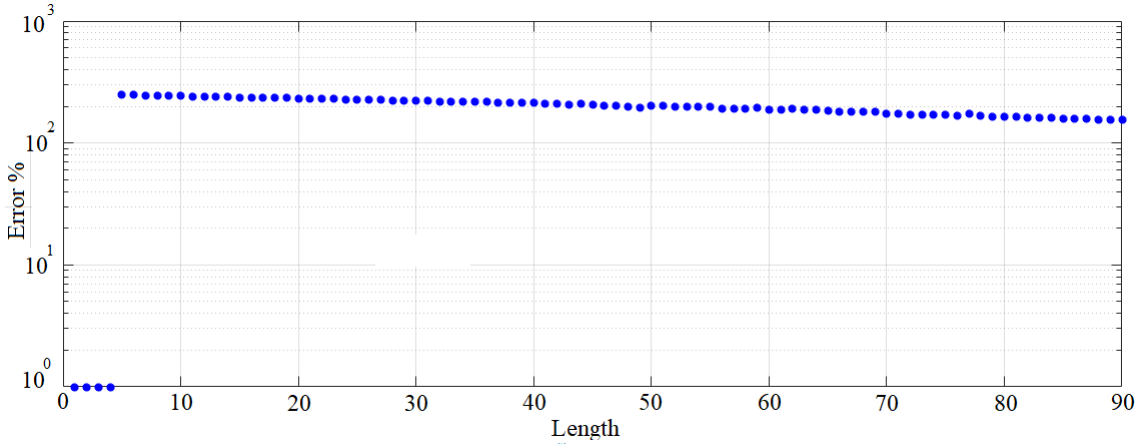

Figure 7.4: Blur segmentation with a 256x256 sharp cut-off window. The Relative Error is plotted between 5 to 90 pixel long.

-

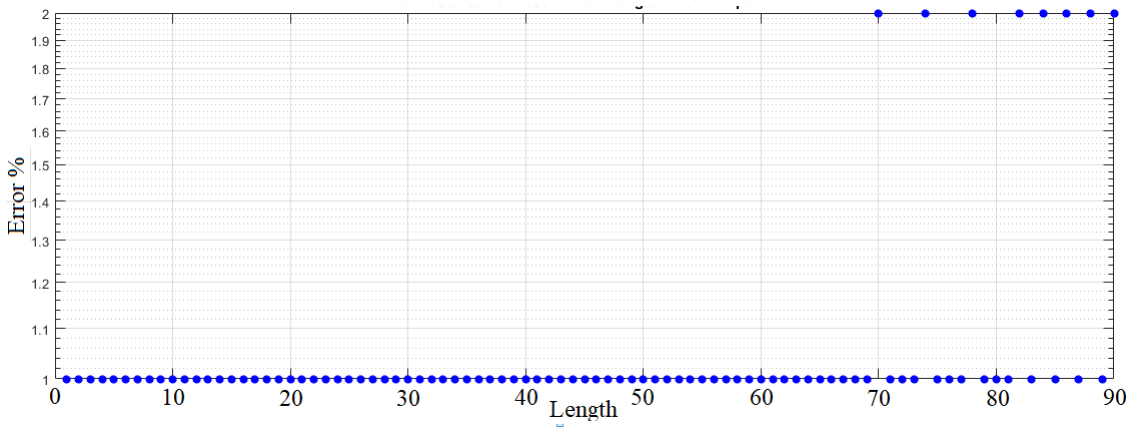

Figure 7.5: Blur segmentation with a 256x256 Hanning window. The Relative error is plotted between 5 to 90 pixel long.

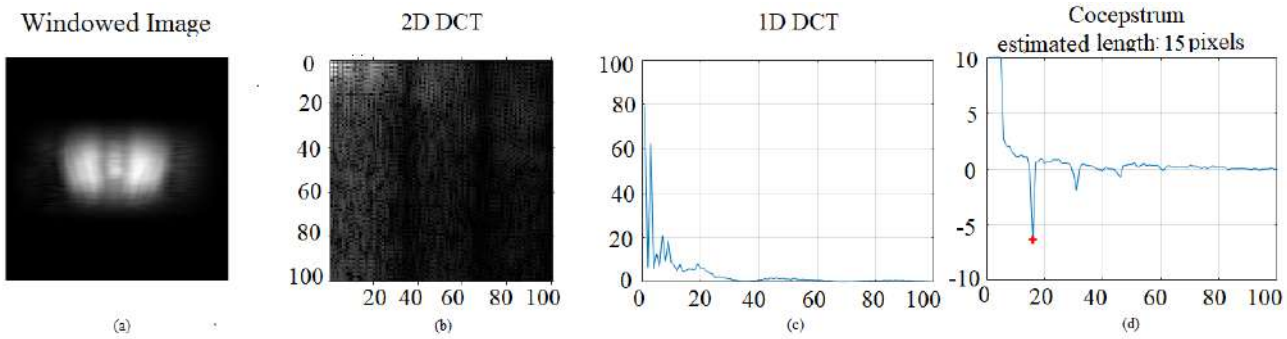

Figure 7.6: Blur segmentation with a 128x256 Hanning window. The figures were captured at 15 pixels blur length. (a) windowed image, (b) Discrete Cosine Transform of Windowed image shown in (a), (c) 1D collapsed version of the Discrete Cosine Transform shown in (b), and the blur length estimation using the. proposed DCT algorithm.

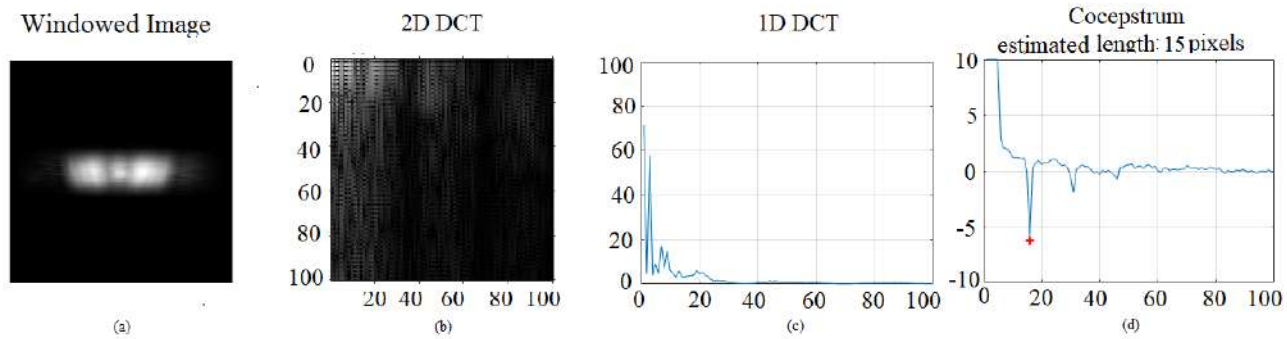

Figure 7.7: Blur segmentation with a 64x256 Hanning window. The figures were captured at 15 pixels blur length. (a) windowed image, (b) Discrete Cosine Transform of Windowed image shown in (a), (c) 1D collapsed version of the Discrete Cosine Transform shown in (b), and the blur length estimation using the proposed DCT algorithm.

As a conceptual reference, Fig.7.6, Fig.7.7, Fig.7.8, Fig.7.9, Fig.7.10, Fig.7.11, and Fig.7.12 show the Baboon image segmented with some Hanning windows of different sizes from 128 to 2 pixel height assuming a constant width of 256 pixels. In all these figures the line pattern added by the linear motion blur is easily visible.

Figure 7.13, from Table 7.1, plots the relative Error when the Hanning window was set at a 256 width, and its height was in the range from 128 to 2 pixels. Notice that the height of the window did not affect significantly the Relative Error. Even the windows were narrow, the motion blur length was estimated accurately. We obtained the best results when the height of the window was above 16 pixels; in these cases, the relative Error was below 6.75%.

In addition, we also evaluated the effect of the window width concerning the relative error. We set the window height at 256 pixels and then, the window width was modified from 10 to 250 in steps of 10 pixels using fixed blur lengths from 10 to 90 in steps of 10 pixels. Figure 7.14, Fig.7.15, and Fig.7.16 show the bar chart for $L = 90$, $L = 60$, and $L = 30$ pixels as examples. These bar charts were made for all blur length given in Table 7.2.

Figure 7.17 plots Table 7.2. This curve depicts the relation between the blur length and the minimum window width. We applied curve fitting using a line equation. The result displayed that the error was tolerant while the width of the window was twice the blur length.

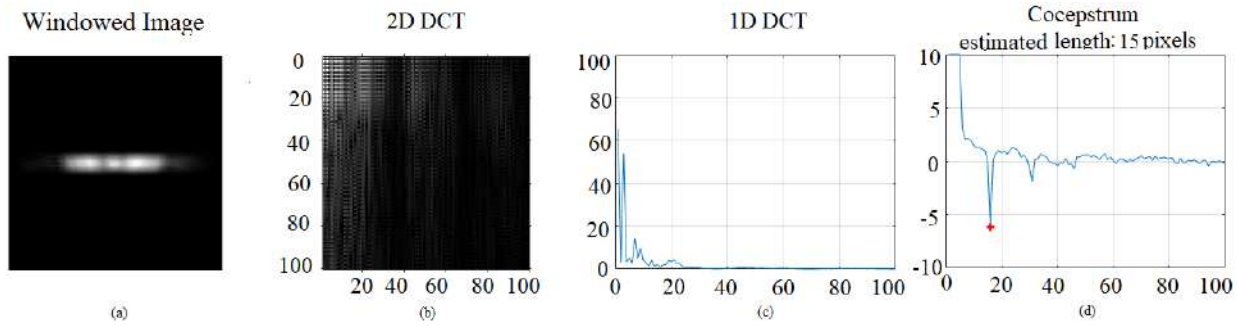

Figure 7.8: Blur segmentation with a 32x256 Hanning window. The figures were captured at 15 pixels blur length. (a) windowed image, (b) Discrete Cosine Transform of Windowed image shown in (a), (c) 1D collapsed version of the Discrete Cosine Transform shown in (b), and the blur length estimation using the . proposed DCT algorithm.

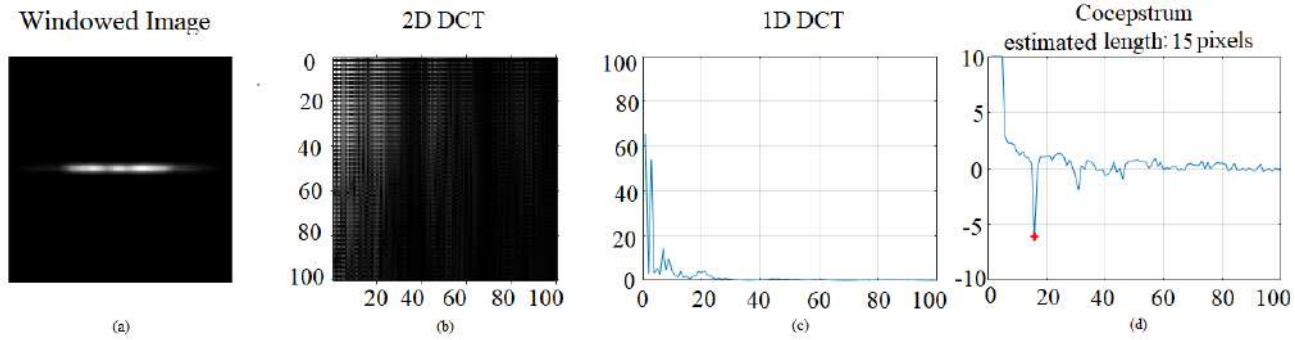

Figure 7.9: Blur segmentation with a 16x256 Hanning window. The figures were captured at 15 pixels blur length. (a) windowed image, (b) Discrete Cosine Transform of Windowed image shown in (a), (c) 1D collapsed version of the Discrete Cosine Transform shown in (b), and the blur length estimation using the. proposed DCT algorithm.

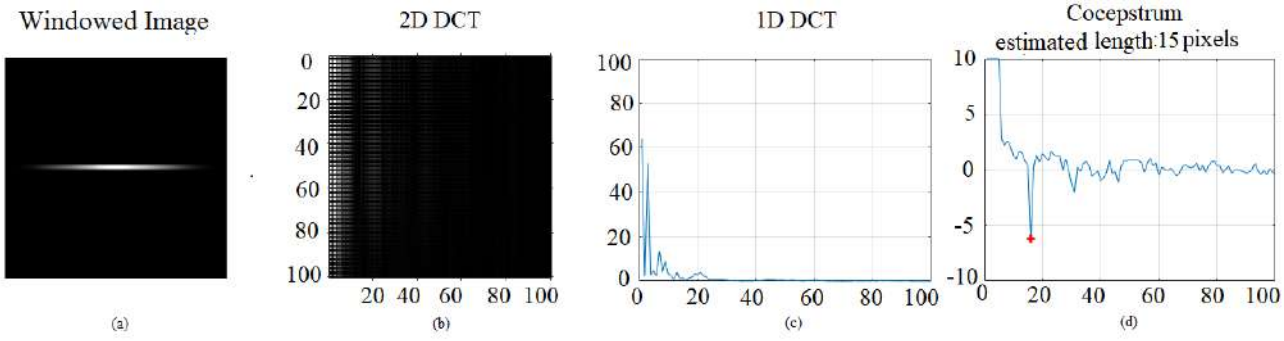

Figure 7.10: Blur segmentation with a 8x256 Hanning window. The figures were captured at 15 pixels blur length. (a) windowed image, (b) Discrete Cosine Transform of Windowed image shown in (a), (c) 1D collapsed version of the Discrete Cosine Transform shown in (b), and the blur length estimation using the. proposed DCT algorithm.

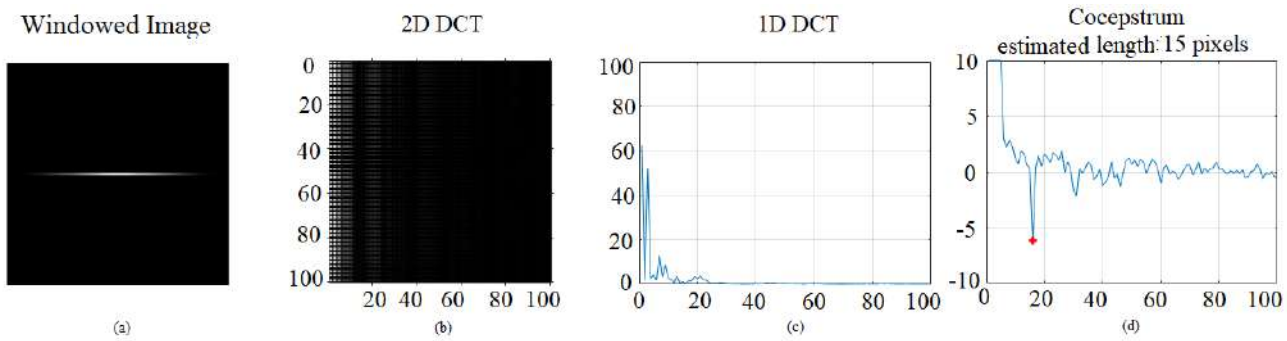

Figure 7.11: Blur segmentation with a 4x256 Hanning window. The figures were captured at 15 pixels blur length. (a) windowed image, (b) Discrete Cosine Transform of Windowed image shown in (a), (c) 1D collapsed version of the Discrete Cosine Transform shown in (b), and the blur length estimation using the. proposed DCT algorithm.

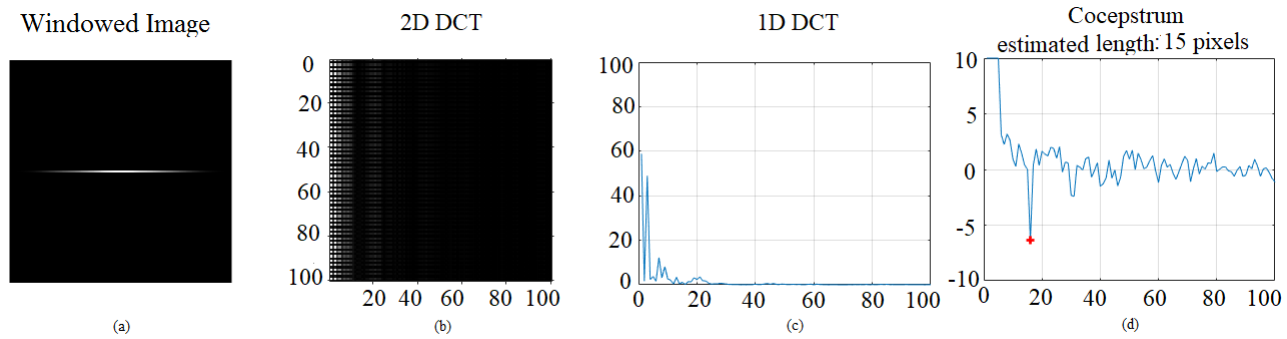

Figure 7.12: Blur segmentation with a 2x256 Hanning window. The figures were captured at 15 pixels blur length. (a) windowed image, (b) Discrete Cosine Transform of Windowed image shown in (a), (c) 1D collapsed version of the Discrete Cosine Transform shown in (b), and the blur length estimation using the. proposed DCT algorithm.

Window height (Pixels)	Relative Error (%)
256	0.09
128	0.10
64	1.95
32	2.10
16	6.75
8	14.41
4	30.14
2	33.29

Table 7.1: Mean error vs pixel height. The error increases as the window height decreases.

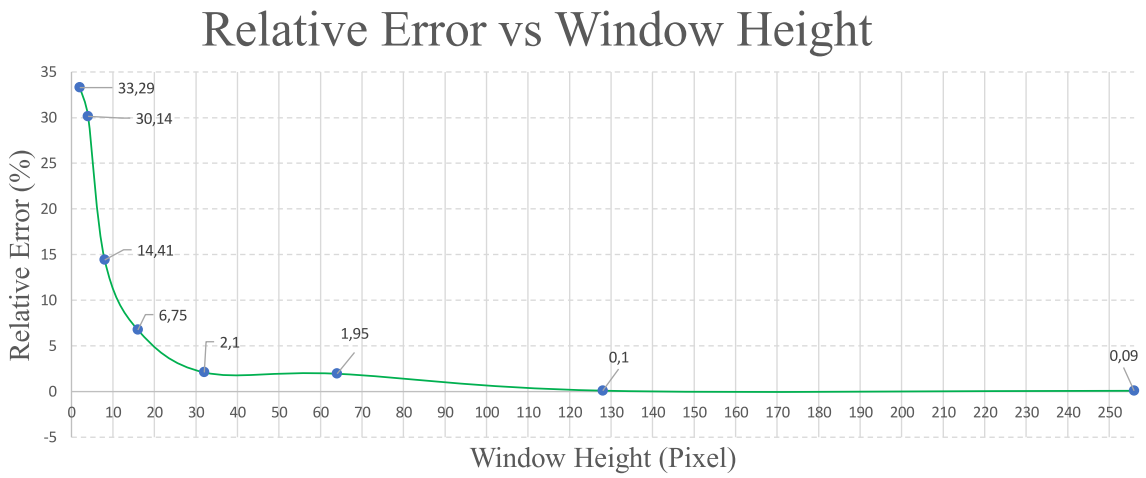

Figure 7.13: Blur segmentation with a variable height window. The relative error curve is plotted using a fixed 30 pixels blur length.

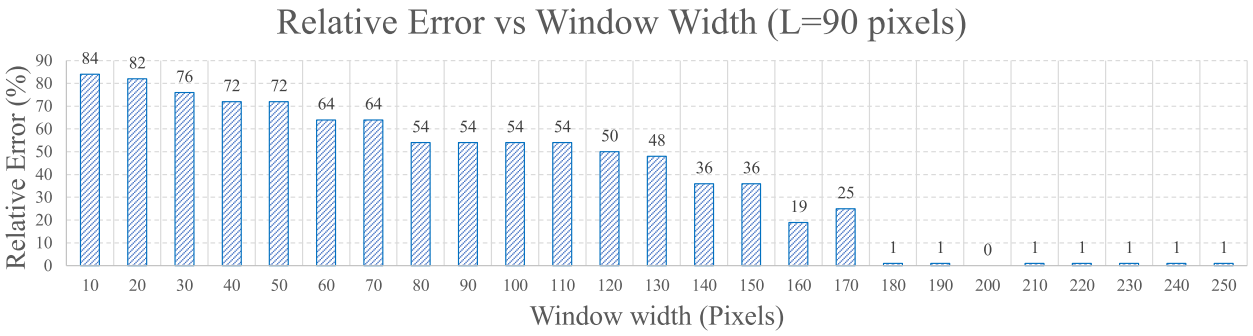

Figure 7.14: Relative error vs a variable window width for a blur length of L=90 pixels. The minimum error of 1% is obtained when the window width is 180 pixels. Notice that the minimum error occurs at 180 pixels.

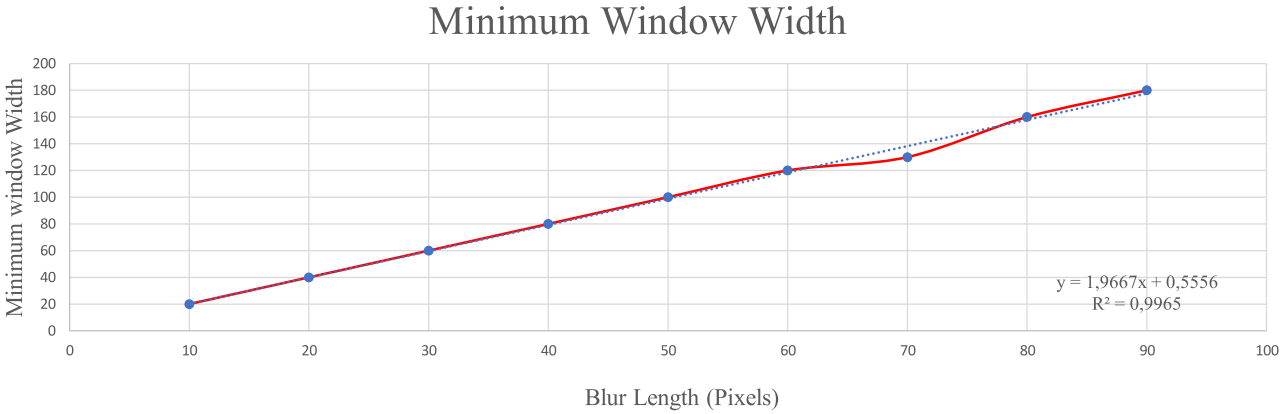

Figure 7.17: Window width that produces minimum error. The window width must be at least the double of the of the blur length.

Blur length (Pixels)	Minimum window width (Pixels)	Relative Error (%)
90	180	1
80	160	0
70	130	1
60	120	0
50	100	0
40	40	0
30	60	0
20	40	0
10	20	0

Table 7.2: Window width that produces minimum error for from 90 to 10 blur-length.

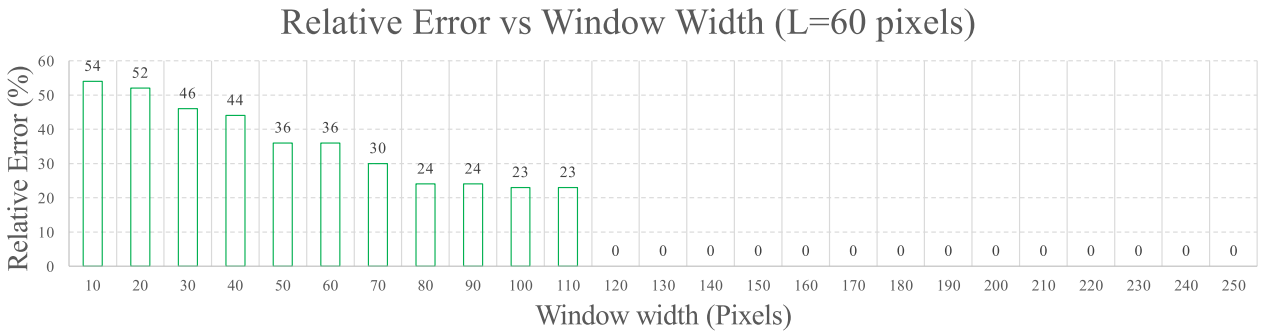

Figure 7.15: Relative Error vs a variable window width for a blur length of L=60 pixels. The limit error of 0% is obtained when the window width is 130 pixels. Notice that the minimum error occurs in 120 pixels.

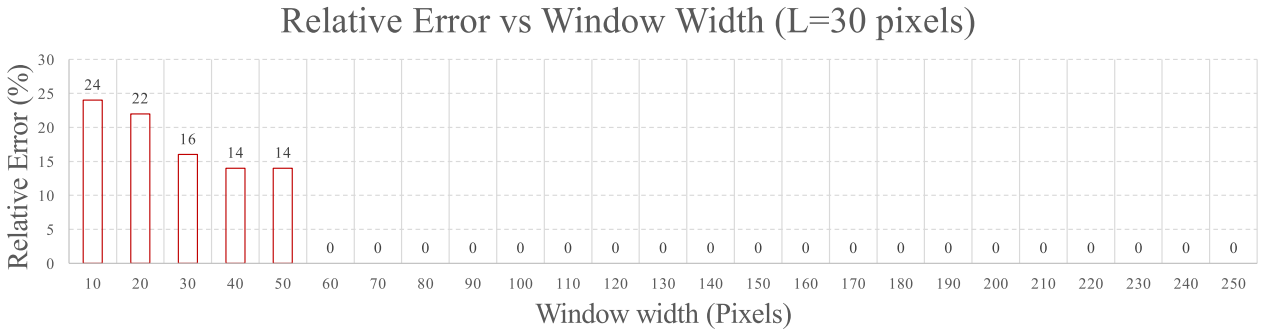

Figure 7.16: Relative Error vs a variable window width for a blur length of L=30 pixels. The minimum error of 0% is obtained when the window width is 60 pixels. Notice that the minimum error occurs in 60 pixels.

7.4 DISCUSSION

Even though other authors have studied blur segmentation, we did not find anyone intended for the estimation of kinematic quantities such as velocity and acceleration. From this perspective, this proof of concept is promising and novel, although it needs further research to be entirely conclusive since until now it has been used only for the estimation of the PSF parameters.

7.5 CONCLUSIONS

The use of a smoothed segmentation window is a viable solution to estimate the blur length when blur is space-variant. Even though these experiments are not entirely conclusive, they provide some hints about how to implement it. There are some well-known algorithms for blur segmentation, but all they need to be modified to eliminate its sharp cut-off edges that add artifacts to the Discrete Fourier pattern (MFT). This proof of concept only considered the Hanning window to smooth the edges of the segmentation window, but we must explore some supplementary alternatives. Additionally, it is worth to notice that the segmentation window is usually an irregular shape which, introduces another challenge to fit the smoothed window in an irregular shape.

It is evident that the smoothed segmentation window in space must be longer (at least twice) than the blur length to estimate the length successfully. As far as we evaluated it, this proposal is only valid for uniformly linear motion blur images, that is to say, images blurred at a constant speed. Also, we have found that the height of the segmentation window is not a critical aspect, as long as the blur length is completely covered.

This proof of concept considered the motion direction at zero degrees. Consequently, angle estimation must be also evaluated using a similar approach.

Chapter 8

ELECTROMECHANICAL SLIDER

This chapter introduces the design and the construction of an electromechanical slider that allows obtaining the instantaneous speed and acceleration of a platform that holds a scientific camera to take photos for the study of linear motion-blurred images. The system was calibrated concerning a standard instrument for the estimation of the uncertainty and the error. The development of the system is split into the following steps: the design and construction of an aluminum electromechanical slider built with a mobile platform that moves at constant speed, the speed calibration of the mobile platform using the Guide for estimation of measurement uncertainty, the design and construction of the electromechanical aluminum slider with a mobile platform that slides at constant acceleration and its calibration also applying the Guide for estimation of measurement uncertainty. The maximum uncertainties were $0.031\,m/s$ and $0.029\,m/s^2$ for speed and acceleration, respectively. The developed system is an electromechanical apparatus that allows moving a platform along with a pair of parallel stainless rods. Its low uncertainty permits the measurement of the instantaneous speed and the acceleration for the study of motion blurred images in a controlled environment.

8.1 INTRODUCTION

In the area of digital image processing, it is common to find different types of degradations that affect its analysis, such as lens aberrations, light diffraction, atmospheric disturbances and motion blurring (Motion Blur). The latter is caused by the relative movement between the camera and observed object, the hand's tremor, or the displacement of the capture system during the exposure time. One of the areas of study of motion blurring is the estimation of its point spread function (PSF) in order to reconstruct the image. This PSF is known as the transfer function of the optical system and is responsible for blurring [Cortés-Osorio et al.(2018)Cortés-Osorio, López-Robayo, and Hernández-Betancourt].

In the paper presented by Klyuvak et al. in [Klyuvak et al.(2018)Klyuvak, Kliuva, and Skrynkovskyy], they carried out the estimation of the PSF of an object and its background to then perform a reconstruction of the image. On the other hand, in [Zhang et al.(2018)Zhang, Zhu, Sun, Wang, and Zhang], they carried out a method for the estimation of the PSF from their parametric modeling. The authors used it to reconstruct the original images with few "artifacts". The fundamental problem of this type of work is that motion blurring was done synthetically, that is, that a mathematical function was used to generate it. Those mentioned above causes

the lack of some real optical phenomena on the captured images such as noise and other lens light distortion. Another area of study of motion blurring is the estimation of speed from an image using the PSF parameters. Lin and Li in [Lin and Li(2004a)] and [Lin and Li(2005)] presented a methodology to calculate the speed of a moving object from a single blurred image. The authors stated that they obtained results of less than 10% for speed. However, they did not mention additional information about the system they used to capture and measure the speed of the moving object. Based on the work of Lin and Li, in [Mohammadi et al.(2010)Mohammadi, Akbari, et al.] Mohammadi et al. used the frequency domain to know the PSF and thus estimate the blur parameters. In this way, the researchers reported an error in the estimation of the speed below 8.5%. Unlike Lin and Li in [Lin and Li(2004a)], Mohammadi used an actual vehicle that ran at 40 km/h. The problem with this approach was that the authors did not provide any evidence of meteorological analysis to rely on the real speed of the car. Due to the above, it is evident that, in state of the art, the estimates of kinematic quantities from motion-blurred images is a trending topic, but the reviewed proposals of the different researchers fail to provide certainty of their results since they were not explicit regarding the metrological procedures used.

Although today there are already systems that allow knowing the speed and acceleration of objects, there is no commercial system capable of capturing images and at the same time making known their speed or acceleration values due to the lack of a comprehensive capture and measurement system for the study of blurry images. This work shows the design and construction of a mechatronic slider for capturing images with spatial invariant blur that allows knowing the instantaneous speed and acceleration at the point where the image is taken.

Mechatronic systems or robotic systems are used today both in industry and academia for the development of new technologies. In 2013 R. Jiménez, F.A. Espinosa and D. Amaya [Moreno et al.(2013)Moreno, Valcárcel, and Hurtado] of the Military University Nueva Granada, in Colombia, implemented the control of a humanoid robot using machine vision that replicated human movements. in that reseach they used an anthropomorphic motion capture system based on the Kinect device to perform the movement imitative of a Bioloid robot. In [Contreras Parada et al.(2014)Contreras Parada, Peña Cortés, and Riaño Jaimes], Contreras et al. designed and built a robotic module for the classification of some fruits, using a robotic arm with 5 degrees of freedom and artificial vision for the recognition of the fruits. Subsequently, Gallo et al. from the University of Ibagué they carried out the design and construction of an electromechanical prototype that allowed emulating the movements of the human arm with a total of 13 degrees of freedom. The final prototype had five fingers with two degrees of freedom each, wrist turning movement, elbow flexion, and full shoulder movement [Gallo Sánchez et al.(2016)Gallo Sánchez, Guerrero Ramírez, Vásquez Salcedo, and Alonso Castro]. In 2017 Londoño, Cortés (Author of this tesis) and Fernandez [Londoño et al.(2017)Londoño, Cortes, and Fernández] built a low-cost electromechanical system for teaching rectilinear movement in a laboratory environment. These previous works are evidence that electromechanical systems have essential applications in academia for the teaching of fundamental physics and research.

In the market, there are different slider systems with constant speed for image capture. In [Slider(2017.)], [EVO.(2017)] there are two motorized sliders with belt and stepper motors. Hhowever, these systems do not have repeatability for different speeds because they are usually controlled through a potentiometer, its range of speeds is limited and the maximum speed reached is not sufficient for the study of the present work. Therefore, some authors have

developed their systems for the study of images with uniform blur. In 2005 J. Pérez and G. Rodríguez [Pérez Huerta and Rodriguez Zurita(2005)] presented a study of the restoration of images blurrred by uniform linear motion and uniformly accelerated motion; in their work they reported the use of a frictionless air-rail to capture the images. Schuon and Diepold [Schuon and Diepold(2009)] conducted a study that compared algorithms for restoring synthetically blurred images and images with real blur. In order to test the algorithms in unfocused images, they built a capture prototype. They used a rail to guide the movement and a stepper motor. When the camera reached a constant speed, images were captured with a constant exposure time of 100ms. In 2010 Y. Ding, S. McCloskey, and J. Yu [Ding et al.(2010)Ding, McCloskey, and Yu] investigated the analysis of the blur with Flutter Shutter camera for nonlinear motion; in their research, they used of a motion system to capture images. In their paper, they stated that the camera and the captured image were fixed. They also mention that they used several speeds controlled by changes in the voltage. For constant accelerations they made use of gravity, throwing an object that pulled the mobile. Dwicahya et al. in [Dwicahya et al.(2018b)Dwicahya, Ramadijanti, and Basuki] they proposed a method to detect the speed of a moving object, for this they developed their device and compared the theoretical results with the values given by the system for speed. The mechanism developed by the researchers attained speeds of up to 33km/h, but they did not perform any calibration. They were not clear regarding the methodology they used to build the instrument and had problems with the regular use of the model. Finally, it is noteworthy that the researchers who have designed the equipment developed in the scientific literature did not estimate its uncertainty and its error. The present manuscript differs, among other aspects, by the severity in the calibration for the estimation of the uncertainty, error measurements, and little dispersion of speed and acceleration data of the constructed system.

Kinematics is the study of motion without taking into account the condition that causes it. Some kinematic quantities are displacement, trajectory, speed, and acceleration, among others [Beggs(1983)]. The assembled prototype allowed us to estimate the kinematic quantities that were present during the motion.

8.2 METHODOLOGY

Due to there are no devices on the market that allow knowing the speed and acceleration of the moving camera, there was a need to construct a controlled slider for the study of uniformly motion blur images. In every electromechanical system, it is necessary to have a set of requirements for the mechanical system, since it is capable of supporting the mass of the camera, the displacements, the efforts and other physical factors that occur with the whole system. For the development of this, the following design requirements were taken into account:

- It must reach speeds up to $0.65\,m/s$.
- Its Fraction should be minimum.
- The slider platform must support, at least the mass, of the Basler acA2000-165 um scientific camera.
- It must have, at lest, ten different speeds and five accelerations.
- The speeds and accelerations must be constant and repeatable.

For a better understanding to the reader about the development of the electromechanical system, the information will be presented as follows: mechanical system design, electronic system design, and speed system calibration, then presented, in the same order, for the design corresponding to acceleration.

8.2.1 Electromechanical design for speed

The principle of a linear encoder was used for speed estimation. It is possible to estimate the speed at each instant, knowing each change between the position and the time interval. For this, the instrument has a set of tooth strips made using laser cutting, which was called encoders. Each one has a quantity of 13 teeth of equal width. Thanks to the known width of each tooth ($\triangle x$), it is possible to determine the displacement of the moving object in an interval with the sum of all $\triangle x$. Additionally, the system saves the time it took for each tooth to pass over the barrier sensor ($\triangle t$). Like displacement, the sum of all $\triangle t$ determines the time it took for the object to pass over the entire measured interval. Finally, if the relationship between x and t is directly proportional, the points generate a straight line, the slope of this line being the velocity of the object in the measured interval. The relationship between $\triangle t$ and $\triangle x$can be seen in Fig.8.1 .

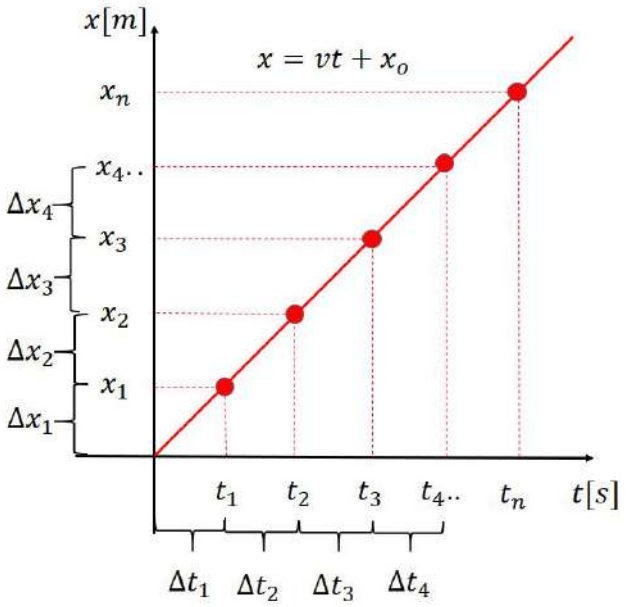

Figure 8.1: Time versus distance plot for constant speed.

Mechanical design

While it was possible to build magnetic or pneumatic levitators to reduce friction, they added instability in the axes of rotation of the mobile platform where the camera was located. Additionally, they were also out of the economic reach of the present work. Finally, a mechanical assembly of two $12\,mm$ diameter robs with linear bearings with reduced friction, and a toothed

belt driven by a DC motor with 10 preset speeds was proposed. Based on the above, the design is shown in Fig. 8.2.

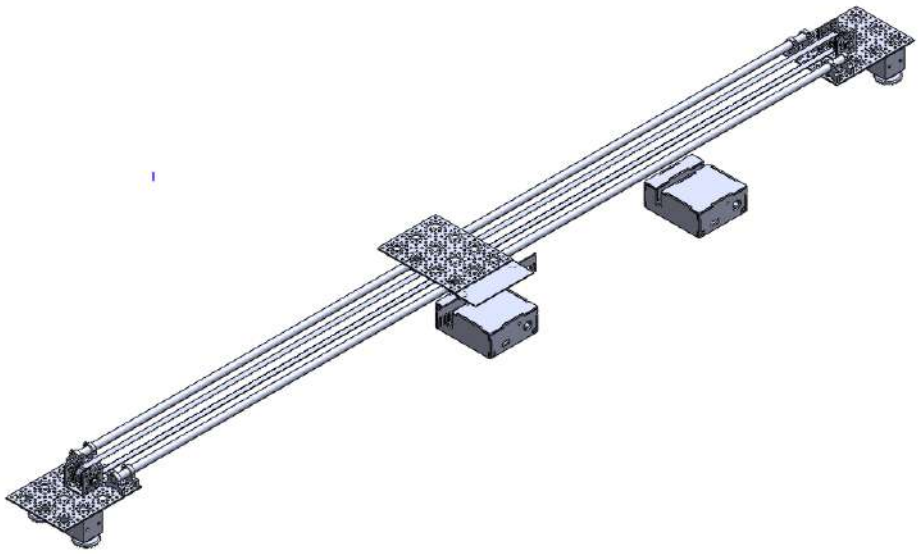

Figure 8.2: Mobile platform on the 12mm rods with the encoder support.

For the selection of the DC motor, two aspects were taken into account; the linear speed and needed torque to move the mobile platform. Starting from the required linear speed of $0.650\,m/s$, the radius of the pinion of $0.012\,m$ and using Eq.8.1 the requiered rpm were calculated.

$$rpm = \frac{v}{r}\frac{60}{2\pi} \tag{8.1}$$

$$rpm = \frac{0.65\,m/s}{0.012\,m}\frac{60}{2\pi} = 517.253\,rpm$$

Where v is the speed and r is the radius of the pinion. The engine selected was the Pololu 37Dx68L, this has a maximum torque of $6\,kg$ - cm and 500 RPM, which is enough to pull the camera mass and to support the aluminum platform. Although the selected mmotor does not reach the revolutions calculated, it was used because, at the time of the development of this work, it was the closest to the calculated value and no other motors were found, of recognized and reliable brands, over 500 RPM with the needed torque.

Electronic design

This section introduces the electronic design of the control, measurement, and trigger stages. Fig.8.3 depics the schematic diagram of the general slider control unit.

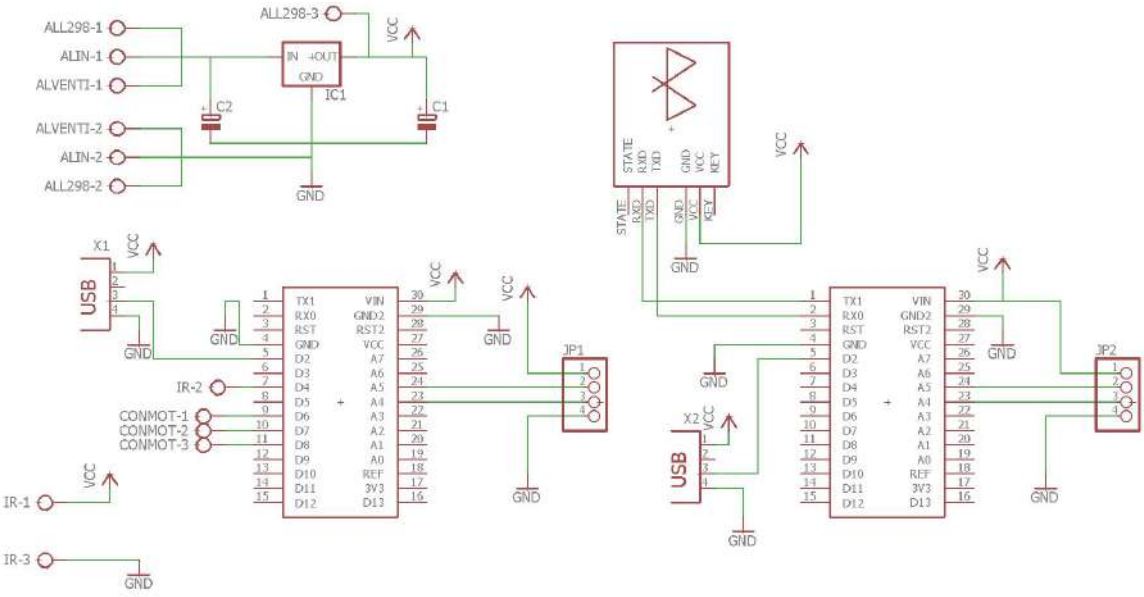

Figure 8.3: Schematic diagram of the general control system.

Speed control system

To control the different speeds, an ATmega 328P was used. It was programmed through the Arduino environment. This microcontroller was chosen to perform speed control because it has counters and timers assisted by a Quarzo crystal that provides high accuracy, in addition to its agile programming. The system accepts commands through a remote control through an infrared sensor; once the command arrives, the microcontroller generated a PWM (Pulse-Width Modulation) value for each of the speeds, which in turn connected with the L298N power controller, that was responsible for sending the pulse to the motor. The principle of a linear encoder was used for speed estimation. It was possible to calculate the speed at each instant, knowing each change between the position and the time interval. For this, the instrument had a set of tooth strips made using laser cutting, which was called encoders. Each one had 13 teeth of same widt. Additionally, the microcontroller displayed on a 16×2 LCD (Liquid Crystal Display) the ID identifier of each of the speeds.When the system detected that the mobile platform passed through the limit switch, it deactivated the PWM signal immediately to slow down the advance and prevent the camera from colliding with the end of the system.

Time measurement system

A circuit was designed with the barrier sensor "SHARP GP1A57HRJ00F", in order to perform the time measurement. The sensor was selected due to its rapid response time to the change of state (Low-High and High-Low), which is $0.5us$. Additionally, it had a 10mm slot, which allowed the encoder to pass without this collision with the horseshoe-shaped sensor. To measure the time it took for each tooth on the barrier sensor (Low output) and the time that was not covered (High output), the ATmega 328P microcontroller was used again, taking advantage of the simplicity of timer programming and precision in the time concerning other microcontrollers evaluated. It should be noted that the use of this second microcontroller facilitates programming and avoids errors in time reading without representing a significant increase in the cost of implementation.

The microcontroller in the control unit was responsible for measuring the time (in microseconds) that each tooth took in high and low. At the end of the measurement, the time value was sent via the Bluetooth module (HC- 05) towards the computer system to perform the speed estimation. When the horseshoe sensor detected an encoder tooth (Low Output), the output went to the camera's trigger to capture the image. An identical stop control circuit was implemented at the end of the run. Fig. 8.4 shows the schematic diagram of the tooth detection circuit.

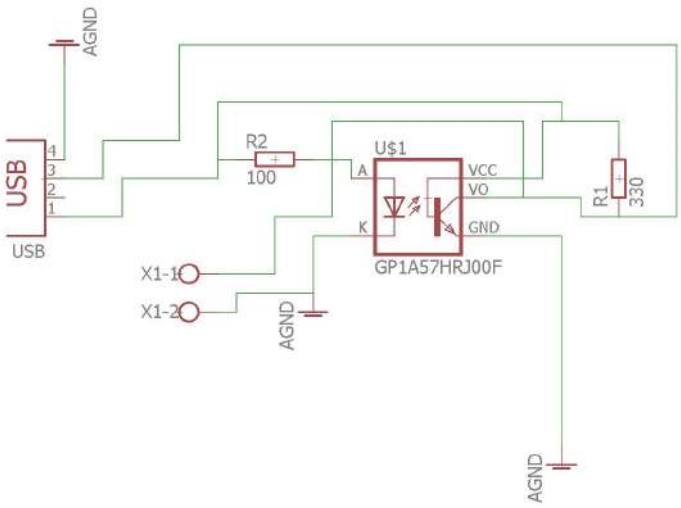

Figure 8.4: Schematic diagram of the pin detection circuit.

User interface

The system was responsible for controlling the speeds, sending the pulse to the camera's trigger and measuring the time it took for each encoder tooth to pass through the horseshoe sensor. Up to this point, estimation of the speed of the object has not been carried out; this was done in order not to overload the microcontroller with tasks that could prevent a correct recording of time. A GUIDE (graphical user interface) was designed in MATLAB 2016a to estimate the speed of the object. This program recorded the time data sent by the control unit and computed them with the distance information of each of the teeth that had been previously calibrated. Fig. 8.5 shows the interface in MATLAB 2016a.

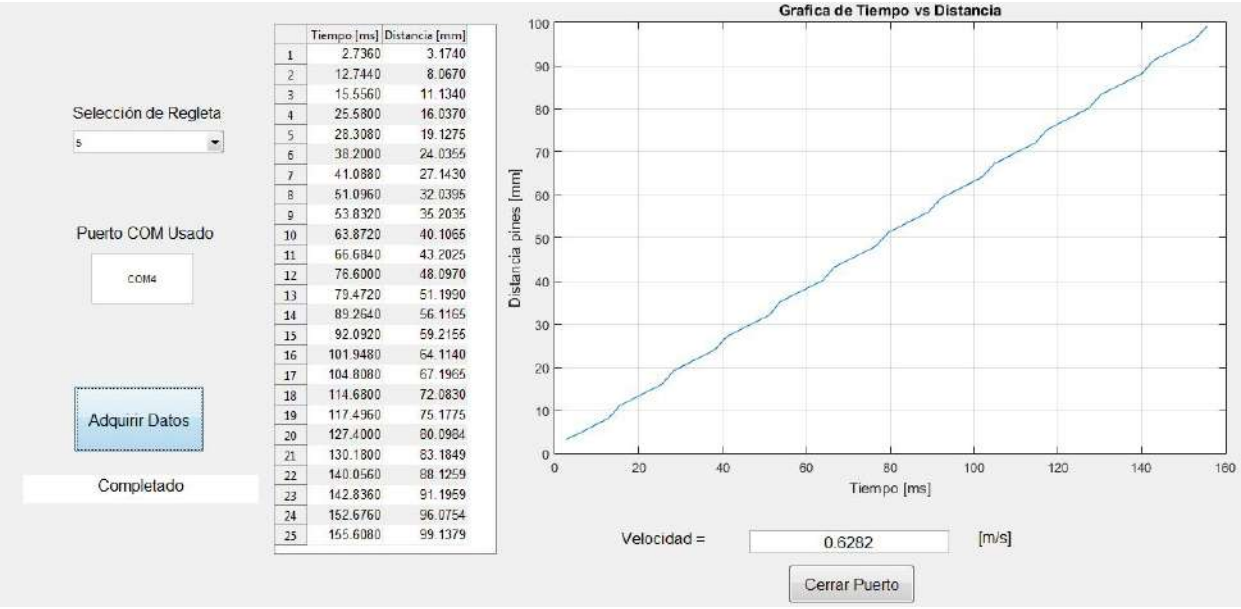

Figure 8.5: Matlab Interface for speed estimation.

As the distance of each encoder tooth was known and the time it took to pass each tooth through the horseshoe sensor, the speed was calculated from a linear regression of the set of points (t, x). The result of the linear regression generated the equation of the line, in the end, the slope was the estimated average velocity of the moving platform, as explained in the section "Electromechanical design for speed".

Speed calibration

The mobile platform that holds the camera represents a fundamental part of the system since its speed is the aim of the study when working with motion blurred-images. For this reason, a calibration procedure was developed, in order to know the uncertainties of the system speeds through an indirect measurement procedure.

Distance calibration

It is necessary to know the distance of the teeth because the encoder represents the displacement of the object over the measured interval. For this, the calibration was performed in order to find the corresponding width uncertainty of each tooth ($\triangle x$). The width of each tooth and the width of each slit of each encoder were measured with the 6-inch digital vernier caliper "RM813 Ubermann". The procedure was performed 20 times for each encoder. Fig. 8.6. shows the encoder set of the measuring system.

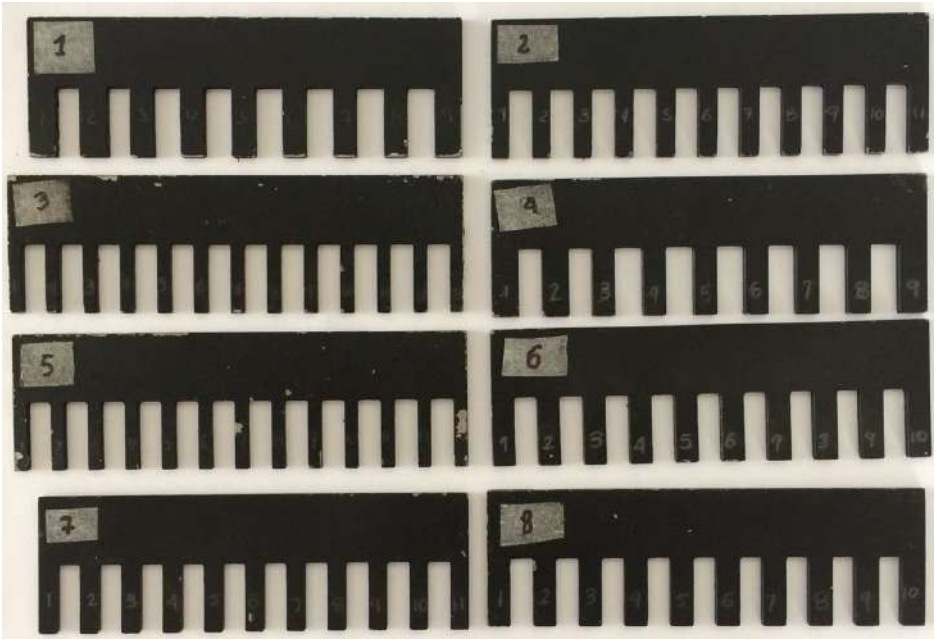

Figure 8.6: Set de encoder del sistema de medida.

The uncertainty was estimated through direct measurements, taking into account the required steps to be followed by the GUM (Guide for estimation of measurement uncertainty) [Schmid et al.(2000)Schmid, Lazos, et al.]. Therefore, the sources of uncertainty shown in Fig. 8.7 were identified.

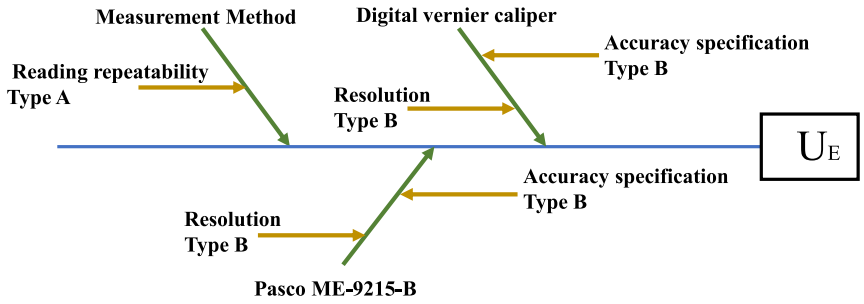

Figure 8.7: Sources of measurement uncertainty in the calibration process.

Type A uncertainty for distance was then estimated from Eq.8.2:

$$U_A = \frac{\sigma}{\sqrt{N}} \tag{8.2}$$

Where σ is the standard deviation of the data set and N the number of measurements. Then the type B1 uncertainty was calculated using Eq.8.3.

$$U_{B1} = \frac{clase\ exactitud\ \times\ lectura\ instrumento}{2\sqrt{3}} \tag{8.3}$$

The datasheet delivers the accuracy class of the manufacturer of the digital vernier caliper. Next, type B2 uncertainty was calculated from Eq.8.4.

$$U_{B2} = \frac{Resolución\ del\ equipo}{2\sqrt{3}} \tag{8.4}$$

The resolution of the equipment is given by the datasheet of the manufacturer of the digital vernier caliper. Then, the combined uncertainty was calculated from Eq.8.5.

$$U_c = \sqrt{U_A^2 + U_{B1}^2 + U_{B2}^2} \tag{8.5}$$

Finally, the expanded uncertainty was estimated from Eq.8.6 with a coverage factor of $k = 1.65$ with a rectangular distribution.

$$U_E = kU_c \tag{8.6}$$

Speed calibration

The procedure for this calibration was carried out through the calculation of uncertainty for indirect measurements recommended by the GUM. Since the indirect measurement to be analyzed is speed (x/t), the variables of distance and time are available. Due to the time consuming that took to calibrate each speed with each encoder independently, a calibration tooth with a 25.2 mm width was designed for the distance measurement (Δx). Then the distance calibration procedure was performed for the calibration tooth of Fig. 8.8.

Figure 8.8: Calibration slit for time.

Two sensors were used For the measurement of time (Δt). The system recorded 20 measurements of the time it took to cross the calibration tooth through the sensors for each of the ten speeds. Finally, a comparison was made between the standard instrument "Digital timer with Infra-Red (IR) barrier Pasco - ME-9215B" (sensor 1) and the system measurement (sensor 2). Fig.8.9. shows the general outline of the calibration in the laboratory.

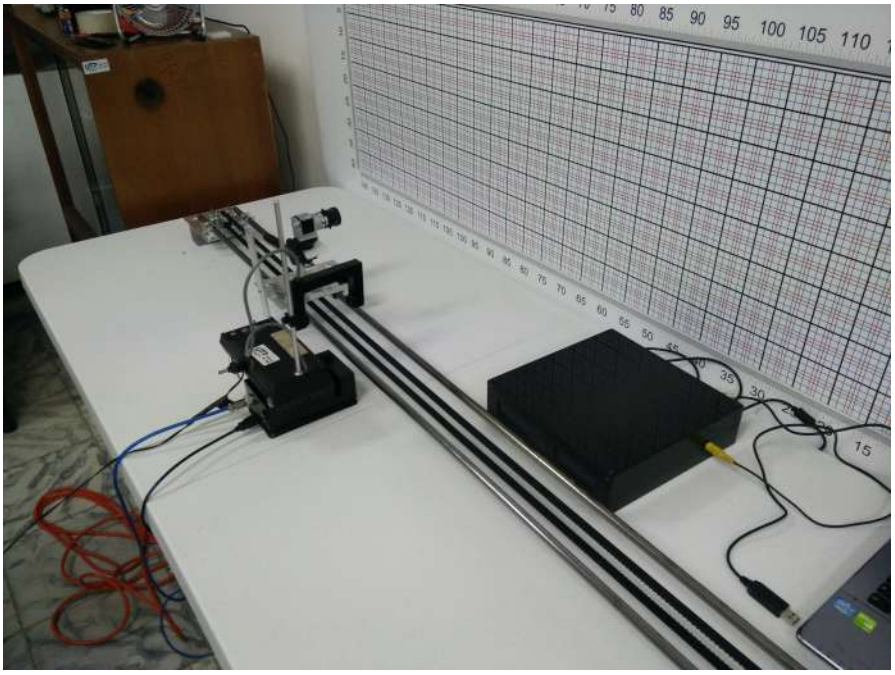

Figure 8.9: Time measurement with the standard instrument and the designed system.

Firstly, the speed calibration procedure was performed. First, type A uncertainty was estimated for the time from Eq.8.2. Next, type B1 uncertainty was calculated using Eq.8.3. Unlike distance calibration, the accuracy class is expressed by 8.7.

$$accuracy\ class = \frac{(E_c - E_p)}{E_p} 100 \tag{8.7}$$

Where Ec is the equipment reading and Ep is the reading of the standard instrument. Then the type B2 uncertainty was estimated from Eq.8.4 with a resolution of the equipment $= 1 \times 10^{-6}$since the system delivers time measurements of the order of microseconds. Then the combined uncertainty was estimated using Eq.8.5. As the speed calibration was performed through indirect measurements, the sensitivity coefficients presented in Eq.8.9 and Eq.8.10 were estimated for each of the ten preset speeds. These coefficients were estimated from the function of uniform rectilinear motion velocity presented in Eq.8.8.

$$v = \frac{x}{t} \tag{8.8}$$

Where x is the distance, t is the time, and v is the speed.

$$C_t = \frac{\partial f}{\partial t} = \frac{\partial}{\partial t}\left(\frac{x}{t}\right) = -\frac{x}{t^2} \tag{8.9}$$

$$C_x = \frac{\partial f}{\partial x} = \frac{\partial}{\partial x}\left(\frac{x}{t}\right) = \frac{1}{t} \tag{8.10}$$

Then the total uncertainty was estimated from Eq.8.11 with the sensitivity coefficients and the combined uncertainty of the distance $(u_c^2(x))$and the time $(u_c^2(t))$ of each velocity with the tooth of calibration.

$$U_c(t) = \sqrt{C_t^2 u_c^2(t) + C_x^2 u_c^2(x)} \tag{8.11}$$

Once the total uncertainty was estimated, the dominant distribution criterion was used; in this case, U_1 was called the standard uncertainty for time, and U_R was the combination of the remaining uncertainties as shown in Eq.8.12 and Eq.8.13.

$$U_1 = \sqrt{C_t^2 u_c^2(t)} \tag{8.12}$$

$$U_R = \sqrt{C_x^2 u_c^2(x)} \tag{8.13}$$

As shown, Eq.8.14 is the relationship between U_1 and U_R, which determines the type of distribution. A ratio of less than 0.3 was obtained; therefore, the procedure was followed with a rectangular distribution.

$$\frac{U_R}{U_1} = \frac{\sqrt{C_x^2 u_c^2(x)}}{\sqrt{C_t^2 u_c^2(t)}} \tag{8.14}$$

Finally, the expanded uncertainty was estimated from Eq.8.6 with a coverage factor of $k = 1.65$ with a rectangular distribution.

8.2.2 Electronic design for acceleration

Mechanical design

With a few modifications in the mechanical system, it was possible to go from constant speed to constant acceleration using the inclined plane principle. The main idea was to raise one end and let the mobile platform move freely along the rails. The belt and engine were decoupled so as not to exert forces on the mobile platform. In order to raise one of the ends of the mechanical system, the lifting support shown in Fig. 8.10 was designed, which allowed changing the angle of inclination of the system, ranging between 2.9°and 15°.

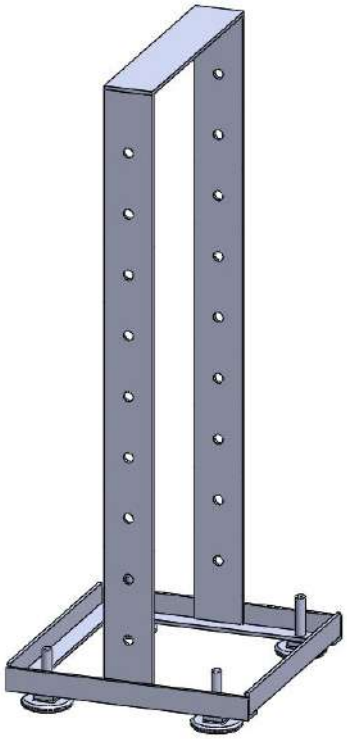

Figure 8.10: View of the lifting support.

When raising the entire system, there was an inconvenience to measure the pulses. the sensor boxes laid down on the laboratory table, so an L-profile was needed to hold the pulse measurement system boxes. Fig. 8.11 shows the final design, and an L-shaped profile is visible from end to end.

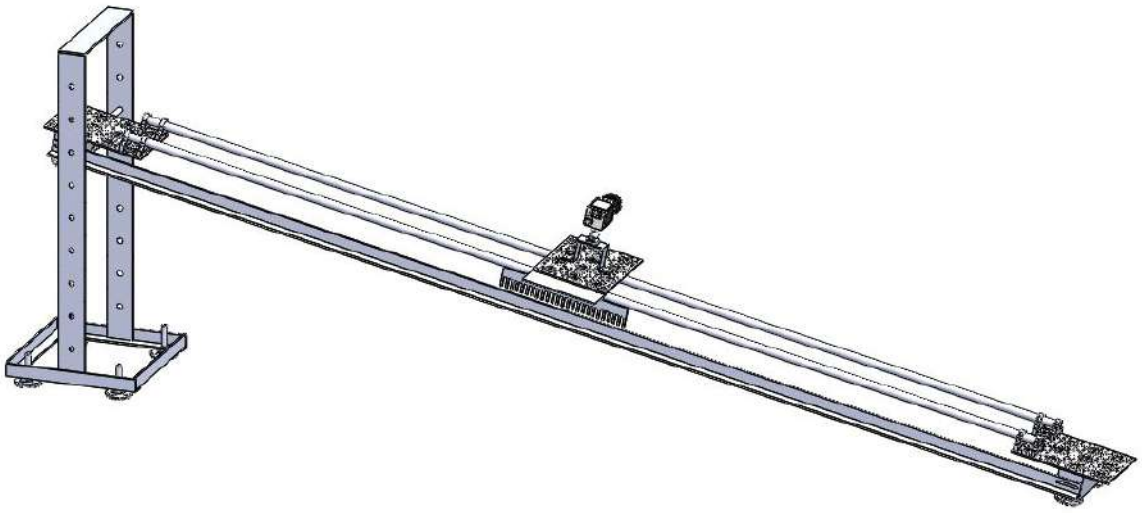

Figure 8.11: Final design of the constant acceleration mechanical system.

Electronic design

A new design of the pulse circuit was made decreasing its size, making it lighter to be attached to the L-profile. Therefore, only a change in the size of the printed circuit is perceived as seen in Fig. 8.12, leaving 6 cm of high by 6 cm wide.

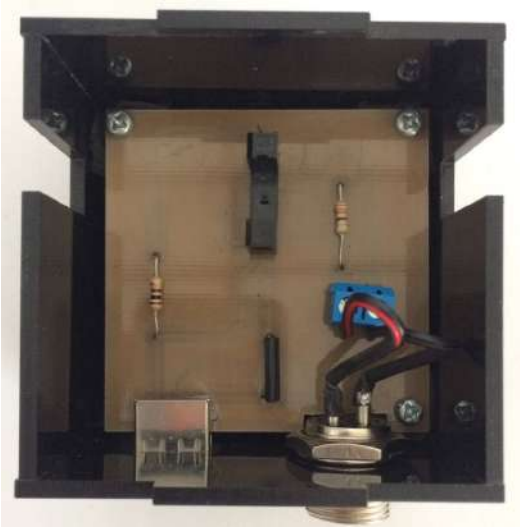

Figure 8.12: Tooth and slit width detector circuit for acceleration measurement.

User interface

The graphical user interface was modified, allowing us to choose in which way to work, speed, or acceleration. In the case of acceleration, a polynomial regression of order two is performed in which the term that accompanies the variable squared corresponds to 1/2 of the acceleration of the mobile platform and the term that accompanies to t is the initial system speed as seen in Fig. 8.13.

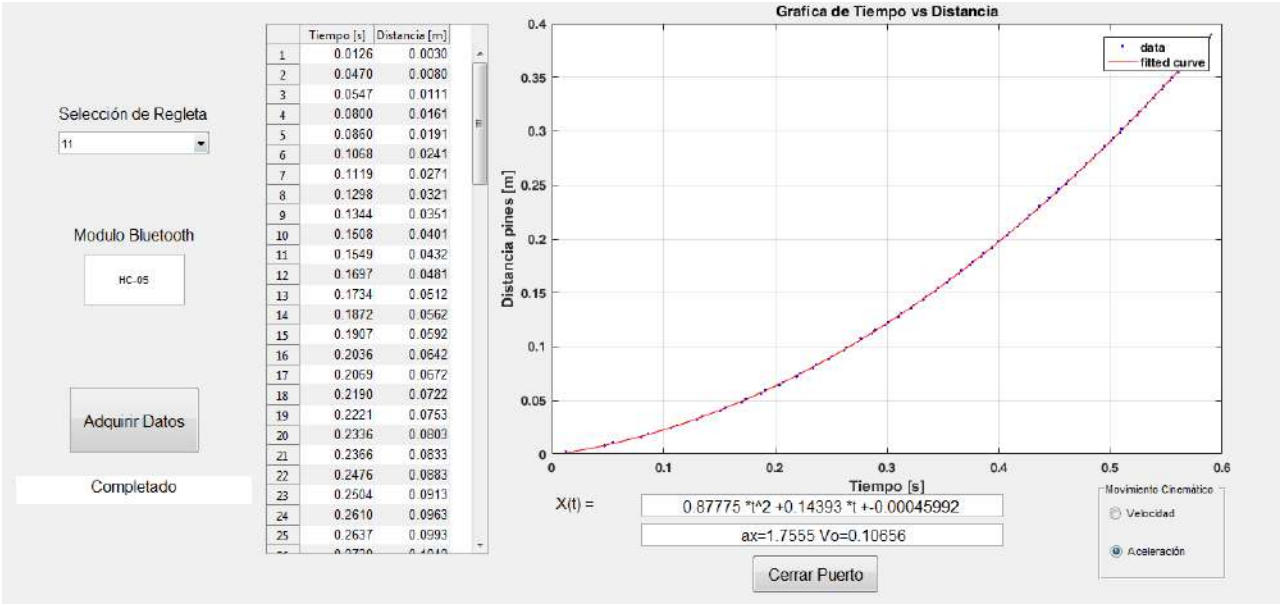

Figure 8.13: User interface for acceleration estimation in MATLAB.

Acceleration calibration

Two sensors were used to take acceleration measurements, which took 20 acceleration measurements according to the angle of inclination (from 2.9° to 15°). Subsequently, a comparison was made between the standard instrument "Phywe Cobra 4 Acceleration" (sensor 1) and the system measurement (sensor 2). Finally, the same direct measurement calibration procedure was performed with a standard instrument seen in the "Distance calibration" section.

8.3 RESULTS

Las Fig. 8.14 y 8.15 show the system in machined aluminum for the platforms, pinions, and fasteners, in addition to 12mm 1045 calibrated steel for the displacement shafts. All printed circuit boards were made in the laboratory with a CNC prototyping machine. Similarly, the acrylic boxes were designed using SolidWorks and cut using a laser. A toothed belt with a 0.2-inch neoprene pitch with fiberglass reinforcement cords was used for the traction system. The sprockets used were 16 teeth with the same belt pitch and a diameter of 1.25 in.

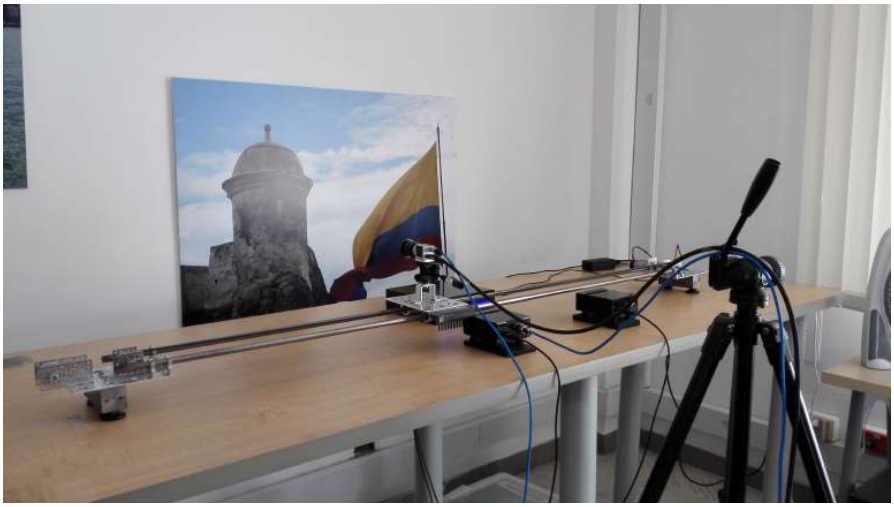

Figure 8.14: Actual electromechanical speed system.

Figure 8.15: Actual alectromechanical acceleration system.

Table 8.1 shows the first 5 teeth and indentations of encoder 5 with their respective average measurements and uncertainties.

Indicador	$X = x \pm U_E[mm]$
tooth 1	3.174±0.035
Slit 1	4.893±0.038
tooth 2	3.067±0.035
Slit 2	4.908±0.036
tooth 3	3.091±0.035
Slit 3	4.908±0.035
tooth 4	3.108±0.036
Slit 4	4.897±0.037
tooth 5	3.164±0.107
Slit 5	4.903±0.036

Table 8.1: Value of some encoder pins with their corresponding uncertainty.

Table 8.2 shows the results of the calibration for each of the 10 speeds.

Index	$V = V \pm U_E[m/s]$
0	0.173±0.012
1	0.229±0.016
2	0.324±0.019
3	0.395±0.022
4	0.457±0.023
5	0.500±0.025
6	0.533±0.027
7	0.573±0.028
8	0.591±0.028
9	0.666±0.031

Table 8.2: Speed value with its corresponding uncertainty.

The results of the calibration of each of the 8 accelerations are shown in the Table 8.3.

Indicador	Ángulo	$a = a \pm U_E[m/s^2]$
1	15°	2.463± 0.029
2	13.3°	2.178± 0.023
3	11.5°	1.863± 0.012
4	10.1°	1.541± 0.016
5	7.9°	1.229 ±0.013
6	6.1°	0.942± 0.009
7	4.5°	0.644± 0.007
8	2.9°	0.351± 0.004

Table 8.3: Acceleration value with corresponding uncertainty.

8.4 CONCLUSIONS

The developed system corresponds to an electromechanical system that allows moving a platform along with a pair of parallel steel rods that support a digital camera. The calibrated slider was assembled to take motion blur photos used to estimate velocity and acceleration from a single image as part of a this study. The final construction of the system was calibrated resulting in uncertainties of $0.173 \pm 0.012\, m/s$ and $0.351 \pm 0.004\, m/s^2$ for speed and acceleration, respectively. The system is reliable for the study of uniform and accelerated linear motion. The system can measure instantaneous speed and acceleration through encoders and sensors, it can also be used for the teaching uniform rectilinear motion and the inclined plane. In the study carried out in [Cortés-Osorio et al.(2018)Cortés-Osorio, López-Robayo, and Hernández-Betancourt], it was possible to take images with uniform blurring with this instrument, and consistent results were obtained in terms of the estimated velocity values. In summary, the speeds in the study using digital image processing were consistent (error less than 5%) with those thrown by the electromechanical system. The results of use are evidenced in the work presented by Cortés Osorio et al. in [Cortes-Osorio et al.(2018)Cortes-Osorio, Gomez-Mendoza, and Riano-Rojas] where it was used to evaluate a novel method for estimating the speed of an object from a single linear motion blur image. It is proposed as future work, increase the maximum speed of the

mobile platform up to $1.5\,m/s$ and expand the range of speeds to 20; this is achieved by changing the motor and increasing the length of the rods, mainlly. This brings new challenges, such as the implementation of the braking system and the heat treatment of the steal rods to reduce buckling. This chapter was published by IngeCuc Journal and it is available in [Cortes-Osorio et al.(2020)Cortes-Osorio, Muñoz Acosta, and López Robayo]

Bibliography

[Gunturk(2012)] X. e. Gunturk, Bahadir Kursat; LI, "Image restoration: Fundamentals and advances," *Pattern Recognition*, 2012.

[Dobeš et al.(2010)Dobeš, Machala, and Fürst] M. Dobeš, L. Machala, and T. Fürst, "Blurred image restoration: A fast method of finding the motion length and angle," *Digital Signal Processing*, vol. 20, no. 6, pp. 1677–1686, 2010.

[Zhou and Zhang(2018)] L. Zhou and Z. Zhang, "Moving objects segmentation and extraction based on motion blur features," *Computers & Electrical Engineering*, vol. 68, pp. 490–498, 2018. [Online]. Available: https://doi.org/10.1016/j.compeleceng.2018.05.003

[Luh et al.(1980)Luh, Walker, and Paul] J. Luh, M. Walker, and R. Paul, "Resolved-acceleration control of mechanical manipulators," *IEEE Transactions on Automatic Control*, vol. 25, no. 3, pp. 468–474, 1980.

[Hoberock(1977)] L. L. Hoberock, "A survey of longitudinal acceleration comfort studies in ground transportation vehicles," *Journal of Dynamic Systems, Measurement, and Control*, vol. 99, no. 2, pp. 76–84, 1977.

[Lepetič et al.(2003)Lepetič, Klančar, Škrjanc, Matko, and Potočnik] M. Lepetič, G. Klančar, I. Škrjanc, D. Matko, and B. Potočnik, "Time optimal path planning considering acceleration limits," *Robotics and Autonomous Systems*, vol. 45, no. 3-4, pp. 199–210, 2003. [Online]. Available: https://doi.org/10.1016/j.robot.2003.09.007

[Sironi and Spitkovsky(2011)] L. Sironi and A. Spitkovsky, "Acceleration of particles at the termination shock of a relativistic striped wind," *The Astrophysical Journal*, vol. 741, no. 1, p. 39, 2011.

[Ohgi(2002)] Y. Ohgi, "Microcomputer-based acceleration sensor device for sports biomechanics," *Memory*, vol. 32, p. 128Mbit, 2002.

[Xu et al.(2013)Xu, Liu, and Li] J. Xu, F. Liu, and D. Li, "Investigation of velocity and acceleration fields on limestone specimen surface under uniaxial compression loads using video images," Beijing, China, 2013, pp. 655 – 660.

[Sawicki et al.(2003)Sawicki, Wu, Baaklini, and Gyekenyesi] J. T. Sawicki, X. Wu, G. Y. Baaklini, and A. L. Gyekenyesi, "Vibration-based crack diagnosis in rotating shafts during acceleration through resonance," in *Nondestructive Evaluation and Health Monitoring of Aerospace Materials and Composites II*, vol. 5046. International Society for Optics and Photonics, 2003, pp. 1–11. [Online]. Available: https://doi.org/10.1117/12.484297

[Hozumi et al.(2000)Hozumi, Yoshida, Akasaka, Asami, Kanzaki, Ueda, Yamamuro, Takagi, and Yoshikawa] T. Hozumi, K. Yoshida, T. Akasaka, Y. Asami, Y. Kanzaki, Y. Ueda, A. Yamamuro, T. Takagi, and J. Yoshikawa, "Value of acceleration flow and the prestenotic to stenotic coronary flow velocity ratio by transthoracic color doppler echocardiography in non-invasive diagnosis of restenosis after percutaneous transluminal coronary angioplasty," *Journal of the American College of Cardiology*, vol. 35, no. 1, pp. 164–168, 2000.

[Stanisavljevic et al.(2000)Stanisavljevic, Kalafatic, and Ribaric] V. Stanisavljevic, Z. Kalafatic, and S. Ribaric, "Optical flow estimation over extended image sequence," in *Electrotechnical Conference, 2000. MELECON 2000. 10th Mediterranean*, vol. 2. IEEE, 2000, pp. 546–549.

[Barron et al.(1994)Barron, Fleet, and Beauchemin] J. L. Barron, D. J. Fleet, and S. S. Beauchemin, "Performance of optical flow techniques," *International journal of computer vision*, vol. 12, no. 1, pp. 43–77, 1994.

[Bab-Hadiashar and Suter(1998)] A. Bab-Hadiashar and D. Suter, "Robust optic flow computation," *International Journal of Computer Vision*, vol. 29, no. 1, pp. 59–77, 1998.

[Ishiyama et al.(2004)Ishiyama, Okatani, and Deguchi] H. Ishiyama, T. Okatani, and K. Deguchi, "High-speed and high-precision optical flow detection for real-time motion segmentation," in *SICE 2004 Annual Conference*, vol. 2. IEEE, 2004, pp. 1202–1205.

[Pinto et al.(2014)Pinto, Moreira, Correia, and Costa] A. M. Pinto, A. P. Moreira, M. V. Correia, and P. G. Costa, "A flow-based motion perception technique for an autonomous robot system," *Journal of Intelligent & Robotic Systems*, vol. 75, no. 3-4, pp. 475–492, 2014.

[Su et al.(2011)Su, Lu, and Tan] B. Su, S. Lu, and C. L. Tan, "Blurred image region detection and classification," in *Proceedings of the 19th ACM international conference on Multimedia*. ACM, 2011, pp. 1397–1400.

[Wu et al.(2012)Wu, Guan, Su, and Zhang] J. Wu, Y. Guan, M. Su, and H. Zhang, "A real-time method for detecting sharp images in visual navigation," in *Robotics and Biomimetics (ROBIO), 2012 IEEE International Conference on*. IEEE, 2012, pp. 884–889.

[Wu et al.(2011)Wu, Ling, Yu, Li, Mei, and Cheng] Y. Wu, H. Ling, J. Yu, F. Li, X. Mei, and E. Cheng, "Blurred target tracking by blur-driven tracker," in *Computer Vision (ICCV), 2011 IEEE International Conference on*. IEEE, 2011, pp. 1100–1107.

[Dai and Wu(2008)] S. Dai and Y. Wu, "Motion from blur," in *Computer Vision and Pattern Recognition, 2008. CVPR 2008. IEEE Conference on*. IEEE, 2008, pp. 1–8.

[Sorel et al.(2009)Sorel, Sroubek, and Flusser] M. Sorel, F. Sroubek, and J. Flusser, "Recent advances in space-variant deblurring and image stabilization," *Springer Science + Business*, pp. pp 259–272, 2009.

[McCloskey et al.(2011)McCloskey, Muldoon, and Venkatesha] S. McCloskey, K. Muldoon, and S. Venkatesha, "Motion invariance and custom blur from lens motion," in *Proc. IEEE Int. Conf. Computational Photography (ICCP)*, Apr. 2011, pp. 1–8.

[Yitzhaky and Stern(2003)] Y. Yitzhaky and A. Stern, "Restoration of interlaced images degraded by variable velocity motion," *Optical Engineering*, vol. 42, no. 12, pp. 3557–3565, 2003.

[Yitzhaky et al.(1998)Yitzhaky, Mor, Lantzman, and Kopeika] Y. Yitzhaky, I. Mor, A. Lantzman, and N. Kopeika, "Direct method for restoration of motion-blurred images," *Journal of the Optical Society of America*, vol. 15, no. 6, pp. 1512–1519, 1998.

[Pérez Huerta and Rodriguez Zurita(2005)] J. Pérez Huerta and G. Rodriguez Zurita, "Image restoration of blurring due to rectilinear motion: constant velocity and constant acceleration," *Revista mexicana de física*, vol. 51, no. 4, pp. 398–406, 2005.

[Loce and Wolberg(1995)] R. P. Loce and G. Wolberg, "Characterization of vibration-induced image defects in input scanners." in *Document Recognition*, 1995, pp. 350–357.

[Fliegel(2004)] K. Fliegel, "Modeling and measurement of image sensor characteristics," *RADIOENGINEERING-PRAGUE-*, vol. 13, no. 4, pp. 27–34, 2004.

[Lin and Li(2004a)] H. Lin and K. Li, "Motion blur removal and its application to vehicle speed detection," *Electrical Engineering*, no. 2, pp. 3407–3410, 2004.

[Bovik(2009)] A. Bovik, *The essential guide to image processing.* Academic Press, 2009.

[Rajagopalan and Chellappa(2014)] A. Rajagopalan and R. Chellappa, *Motion Deblurring: Algorithms and Systems.* Cambridge University Press, 2014.

[Sorel and Flusser(2008)] M. Sorel and J. Flusser, "Space-Variant Restoration of Images Degraded by Camera Motion Blur," *IEEE Transactions on Image Processing*, vol. 17, no. 2, pp. 105–116, 2008.

[Chan and Shen(2005a)] T. F. Chan and J. Shen, *Image processing and analysis: variational, PDE, wavelet, and stochastic methods.* SIAM, 2005.

[Bovik(2010)] A. C. Bovik, *Handbook of image and video processing.* Academic press, 2010.

[Som(1971)] S. Som, "Analysis of the effect of linear smear on photographic images," *JOSA*, vol. 61, no. 7, pp. 859–864, 1971.

[Lin(2005)] H.-Y. Lin, "Vehicle speed detection and identification from a single motion blurred image," in *Application of Computer Vision, 2005. WACV/MOTIONS'05 Volume 1. Seventh IEEE Workshops on*, vol. 1. IEEE, 2005, pp. 461–467.

[Lin and Li(2005)] H.-Y. Lin and K.-J. Li, "Vehicle speed estimation from single still images based on motion blur analysis." in *MVA*, 2005, pp. 128–131.

[Schuon and Diepold(2009)] S. Schuon and K. Diepold, "Comparison of motion de-blur algorithms and real world deployment," *Acta Astronautica*, vol. 64, no. 11, pp. 1050–1065, 2009.

[Deb(2005)] "Motion de-blurring - the nature of blur," 2005. [Online]. Available: http://ai.stanford.edu/~schuon/deblur.htm.

[Celestino and Horikawa(2008)] M. Celestino and O. Horikawa, "Velocity measurement based on image blur," *Computer graphics and image processing*, vol. 3, pp. 633–642, 2008.

[Mohammadi et al.(2010)Mohammadi, Akbari, et al.] J. Mohammadi, R. Akbari *et al.*, "Vehicle speed estimation based on the image motion blur using radon transform," in *Signal Processing Systems (ICSPS), 2010 2nd International Conference on*, vol. 1. IEEE, 2010, pp. V1–243.

[Mohammadi and Taherkhani(2013)] J. Mohammadi and A. Taherkhani, *Object Speed Estimation in Frequency Domain of Single Taken Image*, 2013, vol. 3.

[Olivas et al.(2012)Olivas, Šorel, and Ford] S. J. Olivas, M. Šorel, and J. E. Ford, "Platform motion blur image restoration system," *Applied optics*, vol. 51, no. 34, pp. 8246–8256, 2012.

[Nemeth and Zarandy(2016)] M. Nemeth and A. Zarandy, "Intraframe scene capturing and speed measurement based on superimposed image: New sensor concept for vehicle speed measurement," *Journal of Sensors*, vol. 2016, 2016.

[Lee et al.(2016)Lee, Kim, and Kim] M. Lee, K.-S. Kim, and S. Kim, "Measuring vehicle velocity in real time using modulated motion blur of camera image data," *IEEE Transactions on Vehicular Technology*, vol. 66, no. 5, pp. 3659–3673, 2016.

[Lee(2017)] M. Lee, "A study on measuring vehicle velocity in real time using modulated motion blur of camera image data," Ph.D. dissertation, Korea Advanced Institute of Science and Technology, 2017.

[Lee et al.(2017)Lee, Kim, Cho, and Kim] M. Lee, K.-S. Kim, J. Cho, and S. Kim, "Development of a vehicle body velocity sensor using modulated motion blur," in *2017 IEEE International Conference on Advanced Intelligent Mechatronics (AIM)*. IEEE, 2017, pp. 406–411.

[Jing et al.(2018)Jing, Xiao, Yang, Wang, and Yu] J. Jing, F. Xiao, L. Yang, S. Wang, and B. Yu, "Measurements of velocity field and diameter distribution of particles in multiphase flow based on trajectory imaging," *Flow Measurement and Instrumentation*, vol. 59, pp. 103–113, 2018.

[Matsuo and Yakoh(2018)] K. Matsuo and T. Yakoh, "Position and velocity measurement method from a single image using modulated illumination," in *2018 IEEE 15th International Workshop on Advanced Motion Control (AMC)*. IEEE, 2018, pp. 353–359.

[Dwicahya et al.(2018a)Dwicahya, Ramadijanti, and Basuki] J. A. Dwicahya, N. Ramadijanti, and A. Basuki, "Moving object velocity detection based on motion blur on photos using gray level," in *2018 International Electronics Symposium on Knowledge Creation and Intelligent Computing (IES-KCIC)*. IEEE, 2018, pp. 192–198.

[Zhou et al.(2019)Zhou, Chen, Zhang, Ye, and Tao] H. Zhou, M. Chen, L. Zhang, N. Ye, and C. Tao, "Measuring shape and motion of a high-speed object with designed features from motion blurred images," *Measurement*, vol. 145, pp. 559–567, 2019.

[Liu et al.(2008)Liu, Li, and Jia] R. Liu, Z. Li, and J. Jia, "Image partial blur detection and classification," in *Computer Vision and Pattern Recognition, 2008. CVPR 2008. IEEE Conference on.* IEEE, 2008, pp. 1–8.

[Zhang and Hirakawa(2013a)] Y. Zhang and K. Hirakawa, "Blur processing using double discrete wavelet transform," in *Proceedings of the IEEE Conference on Computer Vision and Pattern Recognition*, 2013, pp. 1091–1098.

[Zhang and Hirakawa(2013b)] ——, "Blur processing using double discrete wavelet transform," in *Proceedings of the IEEE Conference on Computer Vision and Pattern Recognition*, 2013, pp. 1091–1098.

[Guo and Wang(2013)] Y. Guo and P. Wang, "Identification of motion blur parameters based on 2d-dwt and cepstrum," *Journal of Computational Information Systems*, vol. 9, no. 16, pp. 6325–6332, 2013.

[Phansalkar(2010a)] N. Phansalkar, "Determination of linear motion point spread function using hough transform for image restoration," *IEEE*, pp. 1–4, 2010.

[Grou-Szabo and Shibata(2009a)] R. Grou-Szabo and T. Shibata, "Blind motion-blur parameter estimation using edge detectors," in *3rd. International Conference on Signal Processing and Communication Systems*, 2009.

[Aizenberg et al.(2000)Aizenberg, Aizenberg, Butakov, and Farberov] I. Aizenberg, N. Aizenberg, C. Butakov, and E. Farberov, "Image recognition on the neural network based on multi-valued neurons," in *Proc. 15th Int. Conf. Pattern Recognition. ICPR-2000*, vol. 2, 2000, pp. 989–992 vol.2.

[Li et al.(2007)Li, Mersereau, and Simske] D. Li, R. M. Mersereau, and S. Simske, "Blind image deconvolution through support vector regression," *IEEE transactions on neural networks*, vol. 18, no. 3, pp. 931–935, 2007.

[Chen et al.(2010)Chen, Yang, Wu, and Zhao] X. Chen, J. Yang, Q. Wu, and J. Zhao, "Motion blur detection based on lowest directional high-frequency energy," in *Image Processing (ICIP), 2010 17th IEEE International Conference on.* IEEE, 2010, pp. 2533–2536.

[Tiwari et al.(2014)Tiwari, Singh, and Shukla] S. Tiwari, A. K. Singh, and V. Shukla, "Certain investigations on motion blur detection and estimation," in *Proceedings of international conference on signal, image and video processing, IIT Patna*, 2014, pp. 108–114.

[Lokhande et al.(2006)Lokhande, Arya, and Gupta] R. Lokhande, K. Arya, and P. Gupta, "Identification of parameters and restoration of motion blurred images," in *Proceedings of the 2006 ACM symposium on Applied computing.* ACM, 2006, pp. 301–305.

[Su et al.(2012)Su, Lu, and Lim] B. Su, S. Lu, and T. C. Lim, "Restoration of motion blurred document images," in *Proceedings of the 27th Annual ACM Symposium on Applied Computing.* ACM, 2012, pp. 767–770.

[Moghaddam and Jamzad(2007)] M. E. Moghaddam and M. Jamzad, "Linear motion blur parameter estimation in noisy images using fuzzy sets and power spectrum," *EURASIP Journal on Advances in Signal Processing*, vol. 2007, no. 1, pp. 1–8, 2007.

[Jia and Wen(2013)] S. Jia and J. Wen, "Motion blurred image restoration," in *Image and Signal Processing (CISP), 2013 6th International Congress on*, vol. 1. IEEE, 2013, pp. 384–389.

[Krahmer et al.(2006)Krahmer, Lin, McAdoo, Ott, Wang, Widemann, and Wohlberg] F. Krahmer, Y. Lin, B. McAdoo, K. Ott, J. Wang, D. Widemann, and B. Wohlberg, "Blind image deconvolution: Motion blur estimation," Institute for Mathematics and its Applications, University of Minnesota, USA, Tech. Rep., 2006.

[Pazhoumand-Dar et al.(2010)Pazhoumand-Dar, Abolhassani, and Saeedi] H. Pazhoumand-Dar, A. M. T. Abolhassani, and E. Saeedi, "Object speed estimation by using fuzzy set," *World Academy of Science, Engineering and Technology, International Journal of Computer, Electrical, Automation, Control and Information Engineering*, vol. 4, no. 4, pp. 688–691, 2010.

[Ji and Liu(2008)] H. Ji and C. Liu, "Motion blur identification from image gradients," in *Computer Vision and Pattern Recognition, 2008. CVPR 2008. IEEE Conference on*. IEEE, 2008, pp. 1–8.

[Rekleitis(1996)] I. M. Rekleitis, "Steerable filters and cepstral analysis for optical flow calculation from a single blurred image," in *Vision Interface*, vol. 1, 1996, pp. 159–166.

[Tiwari and Shukla(2013)] S. Tiwari and Shukla, "Review of motion blur estimation techniques," *Journal of Image and Graphics*, vol. 1, no. 4, pp. 176–184, 2013.

[Cannon(1976)] M. Cannon, "Blind deconvolution of spatially invariant image blurs with phase," *Acoustics, Speech and Signal Processing, IEEE Transactions on*, vol. 24, no. 1, pp. 58–63, 1976.

[Kundur and Hatzinakos(1996)] D. Kundur and D. Hatzinakos, "Blind image deconvolution," *IEEE Signal Processing Magazine*, vol. 13, no. 3, pp. 43–64, May 1996.

[Dash(2012)] R. Dash, "Parameters estimation for image restoration," Ph.D. dissertation, Department of Computer Science and Engineering, National Institute of Technology Rourkela, Rourkela 769008, India, 2012.

[Yang et al.(2011)Yang, Liu, Liu, and Liao] S. Yang, H. Liu, B. Liu, and X. Liao, "Blurring length estimation using ringing artifacts in a deblurred image," in *Image Analysis and Signal Processing (IASP), 2011 International Conference on*. IEEE, 2011, pp. 84–88.

[Gunturk and Li(2012)] B. Gunturk and X. Li, *Image Restoration: Fundamentals and Advances*. CRC Press, 2012.

[Šorel et al.(2009)Šorel, Šroubek, and Flusser] M. Šorel, F. Šroubek, and J. Flusser, *Unexploded Ordnance Detection and Mitigation*, ser. NATO Sci. Peace Secur. Ser. B Phys. Biophys. The address of the publisher: Springer Netherlands, 2009, ch. Recent advances in space-variant deblurring and image stabilization, pp. 259–272.

[Pretto et al.(2009)Pretto, Menegatti, Bennewitz, Burgard, and Pagello] A. Pretto, E. Menegatti, M. Bennewitz, W. Burgard, and E. Pagello, "A visual odometry framework robust to motion blur," in *Int. Conference on Robotics and Automation ICRA'09*, May 2009, pp. 2250–2257.

[Chan and Shen(2005b)] T. Chan and J. Shen, *Image processing and analysis*, ser. Other titles in applied mathematics. Society for Industrial and Applied Mathematics SIAM, 2005, vol. 94.

[Potmesil and Chakravarty(1983)] M. Potmesil and I. Chakravarty, "Modeling motion blur in computer-generated images," in *ACM SIGGRAPH'83*, vol. 17, no. 3, 1983, pp. 389–399.

[Kawamura et al.(2002)Kawamura, Kondo, Konishi, and Ishlgakl] S. Kawamura, K. Kondo, Y. Konishi, and H. Ishlgakl, "Estimation of motion using motion blur for tracking vision system," *IEEE*, pp. 371–376, 2002.

[Xu and Zhao(2010)] T.-F. Xu and P. Zhao, "Image motion-blur-based object's speed measurement using an interlaced scan image," *Measurement Science and Technology*, vol. 21, no. 7, p. 075502, 2010.

[Rezvankhah et al.(2012)Rezvankhah, Bagherzadeh, Moradi, and Member] S. Rezvankhah, A. A. Bagherzadeh, H. Moradi, and B. N. A. Member, "A Real-time Velocity Estimation using Motion Blur in Air Hockey," *IEEE*, 2012.

[Zhang and Hirakawa(2015)] Y. Zhang and K. Hirakawa, "Fast spatially varying object motion blur estimation," in *Image Processing (ICIP), 2015 IEEE International Conference on.* IEEE, 2015, pp. 646–650.

[Brusius et al.(2011)Brusius, Schwanecke, and Barth] F. Brusius, U. Schwanecke, and P. Barth, "Blind image deconvolution of linear motion blur," *International Conference on Computer Vision, Imaging and Computer*, vol. 274, 2011.

[Lu(2006)] E. Lu, JuweiPoon, "Restoration of motion blurred images," *IEEE International*, pp. 1193–1196, 2006.

[GUO et al.(2013)GUO, WANG, and LIU] Y. GUO, P. WANG, and M. LIU, "Identi cation of motion blur parameters based on 2d-dwt and cepstrum," *Journal of Computational Information Systems 9*, vol. 9, no. 16, pp. 6325–6332, 2013.

[Yitzhaky and Kopeika(1997)] Y. Yitzhaky and N. S. Kopeika, "Identification of blur parameters from motion blurred images," *Graphical models and image processing*, vol. 59, no. 5, pp. 310–320, 1997.

[Grou-Szabo and Shibata(2009b)] R. Grou-Szabo and T. Shibata, "Blind motion-blur parameter estimation using edge detectors," in *Signal Processing and Communication Systems, 2009. ICSPCS 2009. 3rd International Conference on.* IEEE, 2009, pp. 1–6.

[Moghaddam and Jamzad(2004)] M. E. Moghaddam and M. Jamzad, "Finding point spread function of motion blur using radon transform and modeling the motion length," in *Signal Processing and Information Technology, 2004. Proceedings of the Fourth IEEE International Symposium on.* IEEE, 2004, pp. 314–317.

[Qi et al.(2005)Qi, Zhang, and Tan] X. Y. Qi, L. Zhang, and C. L. Tan, "Motion deblurring for optical character recognition," in *Document Analysis and Recognition, 2005. Proceedings. Eighth International Conference on.* IEEE, 2005, pp. 389–393.

[Phansalkar(2010b)] N. Phansalkar, "Determination of linear motion Point Spread Function using Hough transform for image restoration," in *In Proceedings of the IEEE International Coference on Computer Intelligence and Computer Research*, 2010.

[Yoshida et al.(1993)Yoshida, Horiike, and Fujita] Y. Yoshida, K. Horiike, and K. Fujita, "Parameter estimation of uniform image blur using dct," *IEICE TRANSACTIONS on Fundamentals of Electronics, Communications and Computer Sciences*, vol. 76, no. 7, pp. 1154–1157, 1993.

[Sakano et al.(2006)Sakano, Suetake, and Uchino] M. Sakano, N. Suetake, and E. Uchino, "Robust identification of motion blur parameters by using angles of gradient vectors," in *Intelligent Signal Processing and Communications, 2006. ISPACS'06. International Symposium on*. IEEE, 2006, pp. 522–525.

[Levin et al.(2011)Levin, Weiss, Durand, and Freeman] A. Levin, Y. Weiss, F. Durand, and W. T. Freeman, "Understanding blind deconvolution algorithms," *IEEE Transactions on Pattern Analysis and Machine Intelligence*, vol. 33, no. 12, pp. 2354–2367, 2011.

[Perrone and Favaro(2016)] D. Perrone and P. Favaro, "A clearer picture of total variation blind deconvolution," *IEEE Transactions on Pattern Analysis and Machine Intelligence*, vol. 38, no. 6, pp. 1041–1055, 2016.

[Lam and Goodman(2000)] E. Y. Lam and J. W. Goodman, "Iterative statistical approach to blind image deconvolution," *J. Opt. Soc. Am. A*, vol. 17, no. 7, pp. 1177–1184, Jul 2000. [Online]. Available: http://josaa.osa.org/abstract.cfm?URI=josaa-17-7-1177

[Burger et al.(2009)Burger, Burge, Burge, and Burge] W. Burger, M. J. Burge, M. J. Burge, and M. J. Burge, *Principles of digital image processing*. Springer, 2009.

[Benesty et al.(2007)Benesty, Sondhi, and Huang] J. Benesty, M. M. Sondhi, and Y. Huang, *Springer handbook of speech processing*. Salmon Tower Building New York City: Springer, 2007.

[Whittaker and Shives(1983)] G. A. Whittaker and T. R. Shives, *Technology Advances in Engineering and Their Impact on Detection, Diagnosis and Prognosis Methods*, C. U. Press, Ed. Cambridge CB2, NY 10022, USA: CUP Archive, 1983, vol. 36.

[Randall(2013)] R. B. Randall, "A history of cepstrum analysis and its application to mechanical problems," in *International Conference at Institute of Technology of Chartres, France*, 2013, pp. 11–16.

[Bogert(1963)] B. P. Bogert, "The quefrency alanysis of time series for echoes; cepstrum, pseudo-autocovariance, cross-cepstrum and saphe cracking," *Time series analysis*, vol. 15, pp. 209–243, 1963.

[Hassanein and Rudko(1984)] H. Hassanein and M. Rudko, "On the use of discrete cosine transform in cepstral analysis," *IEEE Transactions on acoustics, speech, and signal processing*, vol. 32, no. 4, pp. 922–925, 1984.

[Sung et al.(2002)Sung, Kim, Kim, Kwak, Yoo, and Yoo] M.-M. Sung, H.-J. Kim, E.-K. Kim, J.-Y. Kwak, J.-K. Yoo, and H.-S. Yoo, "Clinical evaluation of jpeg2000 compression for digital mammography," *IEEE Transactions on Nuclear Science*, vol. 49, no. 3, pp. 827–832, 2002.

[sip(2017)] "Sipi image database," 2017. [Online]. Available: http://sipi.usc.edu/database/

[bt6(2017)] "Bt.601 : Studio encoding parameters of digital television for standard 4:3 and wide screen 16:9 aspect ratios," 2017. [Online]. Available: http://www.itu.int/rec/r-rec-bt.601

[Shah et al.(2014)Shah, Dalal, Deshpande, and Patnaik] M. J. Shah, U. D. Dalal, A. M. Deshpande, and S. Patnaik, "Hough transform and cepstrum based estimation of spatial-invariant and variant motion blur parameters," in *Advances in Electronics, Computers and Communications (ICAECC), 2014 International Conference on.* IEEE, 2014, pp. 1–6.

[Deshpande and Patnaik(2012)] A. M. Deshpande and S. Patnaik, "Radon transform based uniform and non-uniform motion blur parameter estimation," in *Communication, Information & Computing Technology (ICCICT), 2012 International Conference on.* IEEE, 2012, pp. 1–6.

[Richardson(1972)] W. H. Richardson, "Bayesian-based iterative method of image restoration," *JoSA*, vol. 62, no. 1, pp. 55–59, 1972.

[Lucy(1974)] L. B. Lucy, "An iterative technique for the rectification of observed distributions," *The astronomical journal*, vol. 79, p. 745, 1974.

[Cortés-Osorio et al.(2018)Cortés-Osorio, López-Robayo, and Hernández-Betancourt] J. A. Cortés-Osorio, C. D. López-Robayo, and N. Hernández-Betancourt, "Evaluación y comparación de técnicas para la reconstrucción de la función de dispersión de punto de imágenes degradadas por difuminación lineal uniforme," *TecnoLógicas*, vol. 21, no. 42, pp. 211–229, 2018.

[Pelegri et al.(2002)Pelegri, Alberola, and Llario] J. Pelegri, J. Alberola, and V. Llario, "Vehicle detection and car speed monitoring system using gmr magnetic sensors," in *IECON 02 [Industrial Electronics Society, IEEE 2002 28th Annual Conference of the]*, vol. 2. IEEE, 2002, pp. 1693–1695.

[Li et al.(2011)Li, Dong, Jia, Xu, and Qin] H. Li, H. Dong, L. Jia, D. Xu, and Y. Qin, "Some practical vehicle speed estimation methods by a single traffic magnetic sensor," in *Intelligent Transportation Systems (ITSC), 2011 14th International IEEE Conference on.* IEEE, 2011, pp. 1566–1573.

[Odat et al.(2017)Odat, Shamma, and Claudel] E. Odat, J. S. Shamma, and C. Claudel, "Vehicle classification and speed estimation using combined passive infrared/ultrasonic sensors," *IEEE Transactions on Intelligent Transportation Systems*, 2017.

[Cheung et al.(2005)Cheung, Ergen, and Varaiya] S. Y. Cheung, S. C. Ergen, and P. Varaiya, "Traffic surveillance with wireless magnetic sensors," in *Proceedings of the 12th ITS world congress*, 2005.

[Luvizon et al.(2017)Luvizon, Nassu, and Minetto] D. C. Luvizon, B. T. Nassu, and R. Minetto, "A video-based system for vehicle speed measurement in urban roadways," *IEEE Transactions on Intelligent Transportation Systems*, vol. 18, no. 6, pp. 1393–1404, 2017.

[Wang(2016)] J.-x. Wang, "Research of vehicle speed detection algorithm in video surveillance," in *Audio, Language and Image Processing (ICALIP), 2016 International Conference on*. IEEE, 2016, pp. 349–352.

[Kruger et al.(1995)Kruger, Enkelmann, and Rossle] W. Kruger, W. Enkelmann, and S. Rossle, "Real-time estimation and tracking of optical flow vectors for obstacle detection," in *Intelligent Vehicles' 95 Symposium., Proceedings of the*. IEEE, 1995, pp. 304–309.

[Litzenberger et al.(2006)Litzenberger, Kohn, Belbachir, Donath, Gritsch, Garn, Posch, and Schraml] M. Litzenberger, B. Kohn, A. Belbachir, N. Donath, G. Gritsch, H. Garn, C. Posch, and S. Schraml, "Estimation of vehicle speed based on asynchronous data from a silicon retina optical sensor," in *Intelligent Transportation Systems Conference, 2006. ITSC'06. IEEE*. IEEE, 2006, pp. 653–658.

[Arashloo and Ahmadyfard(2007)] S. R. Arashloo and A. Ahmadyfard, "Fine estimation of blur parmeters for image restoration," in *Digital Signal Processing, 2007 15th International Conference on*. IEEE, 2007, pp. 427–430.

[Gal et al.(2014)Gal, Kiryati, and Sochen] R. Gal, N. Kiryati, and N. Sochen, "Progress in the restoration of image sequences degraded by atmospheric turbulence," *Pattern Recognition Letters*, vol. 48, pp. 8–14, 2014.

[Joshi et al.(2010)Joshi, Kang, Zitnick, and Szeliski] N. Joshi, S. B. Kang, C. L. Zitnick, and R. Szeliski, "Image deblurring using inertial measurement sensors," in *ACM Transactions on Graphics (TOG)*, vol. 29, no. 4. ACM, 2010, p. 30.

[Li et al.(2012)Li, Zhang, Fu, and Meng] T. Li, D. W. Zhang, Y. Fu, and M. Q.-H. Meng, "Motion blur removal for humanoid robots," in *Automation and Logistics (ICAL), 2012 IEEE International Conference on*. IEEE, 2012, pp. 378–381.

[Rizo et al.(2003)Rizo, Coronado, Campo, Forero, Otalora, Devy, and Parra] J. Rizo, J. Coronado, C. Campo, A. Forero, C. Otalora, M. Devy, and C. Parra, "Ursula: robotic demining system," in *Proceedings of the 11th international conference on advanced robotics*, 2003, pp. 538–43.

[Rajasekharan and Kambhampati(2003)] S. Rajasekharan and C. Kambhampati, "The current opinion on the use of robots for landmine detection," in *Robotics and Automation, 2003. Proceedings. ICRA'03. IEEE International Conference on*, vol. 3. IEEE, 2003, pp. 4252–4257.

[Nagatani et al.(2013)Nagatani, Kiribayashi, Okada, Otake, Yoshida, Tadokoro, Nishimura, Yoshida, Koyana
K. Nagatani, S. Kiribayashi, Y. Okada, K. Otake, K. Yoshida, S. Tadokoro, T. Nishimura, T. Yoshida, E. Koyanagi, M. Fukushima *et al.*, "Emergency response to the nuclear accident at the fukushima daiichi nuclear power plants using mobile rescue robots," *Journal of Field Robotics*, vol. 30, no. 1, pp. 44–63, 2013.

[Yamamoto(1992)] S. Yamamoto, "Development of inspection robot for nuclear power plant," in *Robotics and Automation, 1992. Proceedings., 1992 IEEE International Conference on*. IEEE, 1992, pp. 1559–1566.

[Murphy et al.(2008)Murphy, Tadokoro, Nardi, Jacoff, Fiorini, Choset, and Erkmen] R. R. Murphy, S. Tadokoro, D. Nardi, A. Jacoff, P. Fiorini, H. Choset, and A. M. Erkmen, "Search and rescue robotics," in *Springer Handbook of Robotics*. Berlin Heidelberg: Springer, 2008, pp. 1151–1173.

[Casper and Murphy(2003)] J. Casper and R. R. Murphy, "Human-robot interactions during the robot-assisted urban search and rescue response at the world trade center," *IEEE Transactions on Systems, Man, and Cybernetics, Part B (Cybernetics)*, vol. 33, no. 3, pp. 367–385, 2003.

[Lin and Li(2004b)] H.-Y. Lin and K.-J. Li, "Motion blur removal and its application to vehicle speed detection," in *Image Processing, 2004. ICIP'04. 2004 International Conference on*, vol. 5, no. 2. IEEE, 2004, pp. 3407–3410.

[Song et al.(2009)Song, Peng, Lu, Yang, and Yan] D. Song, L. Peng, G. Lu, S. Yang, and Y. Yan, "Velocity measurement of pneumatically conveyed particles through digital imaging," *Sensors and Actuators A: Physical*, vol. 149, no. 2, pp. 180–188, 2009.

[Zhang(2000)] Z. Zhang, "A flexible new technique for camera calibration," *IEEE Transactions on pattern analysis and machine intelligence*, vol. 22, no. 11, pp. 1330–1334, 2000.

[Strobl et al.(2006)Strobl, Sepp, Fuchs, Paredes, and Arbter] K. Strobl, W. Sepp, S. Fuchs, C. Paredes, and K. Arbter, "Camera calibration toolbox for matlab," 2006. [Online]. Available: http://www.vision.caltech.edu/bouguetj/calib_doc/index.html

[Basler(2017)] Basler, "aca2000-165um - basler ace," https://www.baslerweb.com/en/products/cameras/area-scan-cameras/ace/aca2000-165um/, November 2017, (Accessed on 06/11/2017). [Online]. Available: https://www.baslerweb.com/en/products/cameras/area-scan-cameras/ace/aca2000-165um/

[Ric(2017)] "Ricoh lens fl-cc0814a-2m," November 2017, (Accessed on 06/11/2017). [Online]. Available: https://www.baslerweb.com/en/products/vision-components/lenses/ricoh-lens-fl-cc0814a-2m-f1-4-f8mm-2-3/

[Zanobini et al.(2016)Zanobini, Sereni, Catelani, and Ciani] A. Zanobini, B. Sereni, M. Catelani, and L. Ciani, "Repeatability and reproducibility techniques for the analysis of measurement systems," *Measurement*, vol. 86, pp. 125–132, 2016.

[Cortes-Osorio et al.(2018)Cortes-Osorio, Gomez-Mendoza, and Riano-Rojas] J. A. Cortes-Osorio, J. B. Gomez-Mendoza, and J. C. Riano-Rojas, "Velocity estimation from a single linear motion blurred image using discrete cosine transform," *IEEE Transactions on Instrumentation and Measurement*, pp. 1–13, 2018.

[Shirmohammadi and Ferrero(2014)] S. Shirmohammadi and A. Ferrero, "Camera as the instrument: the rising trend of vision based measurement," *IEEE Instrumentation Measurement Magazine*, vol. 17, no. 3, pp. 41–47, Jun. 2014.

[Beauchemin et al.(2012)Beauchemin, Bauer, Kowsari, and Cho] S. S. Beauchemin, M. A. Bauer, T. Kowsari, and J. Cho, "Portable and scalable vision-based vehicular instrumentation for the analysis of driver intentionality," *IEEE Transactions on Instrumentation and Measurement*, vol. 61, no. 2, pp. 391–401, Feb. 2012.

[Motta et al.(2001)Motta, de Carvalho, and McMaster] J. M. S. Motta, G. C. de Carvalho, and R. McMaster, "Robot calibration using a 3d vision-based measurement system with a single camera," *Robotics and Computer-Integrated Manufacturing*, vol. 17, no. 6, pp. 487–497, dec 2001. [Online]. Available: https://doi.org/10.1016/s0736-5845(01)00024-2

[Wahbeh et al.(2003)Wahbeh, Caffrey, and Masri] A. M. Wahbeh, J. P. Caffrey, and S. F. Masri, "A vision-based approach for the direct measurement of displacements in vibrating systems," *Smart Materials and Structures*, vol. 12, no. 5, p. 785, 2003. [Online]. Available: http://stacks.iop.org/0964-1726/12/i=5/a=016

[Karimirad et al.(2014)Karimirad, Chauhan, and Shirinzadeh] F. Karimirad, S. Chauhan, and B. Shirinzadeh, "Vision-based force measurement using neural networks for biological cell microinjection," *Journal of Biomechanics*, vol. 47, no. 5, pp. 1157–1163, mar 2014. [Online]. Available: https://doi.org/10.1016/j.jbiomech.2013.12.007

[Park et al.(2010)Park, Lee, Jung, and Myung] J.-W. Park, J.-J. Lee, H.-J. Jung, and H. Myung, "Vision-based displacement measurement method for high-rise building structures using partitioning approach," *NDT & E International*, vol. 43, no. 7, pp. 642–647, oct 2010. [Online]. Available: https://doi.org/10.1016/j.ndteint.2010.06.009

[Vijayachitra and Krishnaswamy(2005)] S. Vijayachitra and K. Krishnaswamy, *Industrial Instrumentation*. New Age International, 2005.

[Ovaska and Valiviita(1998)] S. J. Ovaska and S. Valiviita, "Angular acceleration measurement: A review," in *Instrumentation and Measurement Technology Conference, 1998. IMTC/98. Conference Proceedings. IEEE*, vol. 2. IEEE, 1998, pp. 875–880.

[Cannon(1974)] T. M. Cannon, "Digital image deblurring by nonlinear homomorphic filtering," Utah University, Salt Lake City School of Computing, Tech. Rep., 1974.

[Chen et al.(1996)Chen, Nandhakumar, and Martin] W.-G. Chen, N. Nandhakumar, and W. N. Martin, "Image motion estimation from motion smear-a new computational model," *IEEE transactions on pattern analysis and machine intelligence*, vol. 18, no. 4, pp. 412–425, 1996.

[Yitzhaky et al.(1999)Yitzhaky, Milberg, Yohaev, and Kopeika] Y. Yitzhaky, R. Milberg, S. Yohaev, and N. S. Kopeika, "Comparison of direct blind deconvolution methods for motion-blurred images," *Applied optics*, vol. 38, no. 20, pp. 4325–4332, 1999. [Online]. Available: https://doi.org/10.1364/AO.38.004325

[Benameur et al.(2012)Benameur, Mignotte, and Lavoie] S. Benameur, M. Mignotte, and F. Lavoie, "An homomorphic filtering and expectation maximization approach for the point spread function estimation in ultrasound imaging," in *Image Processing: Algorithms and Systems X; and Parallel Processing for Imaging Applications II*, vol. 8295. International Society for Optics and Photonics, 2012, p. 82950T. [Online]. Available: https://doi.org/10.1117/12.903785

[Mattausch and Goksel(2016)] O. Mattausch and O. Goksel, "Image-based psf estimation for ultrasound training simulation," in *International Workshop on Simulation and Synthesis in Medical Imaging*. Springer, 2016, pp. 23–33.

[Janwale and Lomte(2017)] A. P. Janwale and S. S. Lomte, "Enhancement of cotton leaves images using various filtering techniques," in *Data Management, Analytics and Innovation (ICDMAI), 2017 International Conference on*. IEEE, 2017, pp. 303–305.

[Raskar et al.(2006)Raskar, Agrawal, and Tumblin] R. Raskar, A. Agrawal, and J. Tumblin, "Coded exposure photography: motion deblurring using fluttered shutter," *ACM Transactions on Graphics (TOG)*, vol. 25, no. 3, pp. 795–804, 2006.

[Li et al.(2008)Li, Du, Zhang, and Wang] M. Li, H. Du, Q. Zhang, and J. Wang, "Improved particle image velocimetry through cell segmentation and competitive survival," *IEEE Transactions on Instrumentation and Measurement*, vol. 57, no. 6, pp. 1221–1229, Jun. 2008.

[Sederman et al.(2004)Sederman, Mantle, Buckley, and Gladden] A. J. Sederman, M. D. Mantle, C. Buckley, and L. F. Gladden, "Mri technique for measurement of velocity vectors, acceleration, and autocorrelation functions in turbulent flow," *Journal of Magnetic Resonance*, vol. 166, no. 2, pp. 182–189, 2004.

[McCloskey et al.(2012)McCloskey, Ding, and Yu] S. McCloskey, Y. Ding, and J. Yu, "Design and estimation of coded exposure point spread functions," *IEEE transactions on pattern analysis and machine intelligence*, vol. 34, no. 10, p. 2071, 2012.

[Agrawal et al.(2009)Agrawal, Xu, and Raskar] A. Agrawal, Y. Xu, and R. Raskar, "Invertible motion blur in video," in *ACM Transactions on Graphics (TOG)*, vol. 28, no. 3. ACM, 2009, p. 95.

[Leifer et al.(2011)Leifer, Weems, Kienle, and Sims] J. Leifer, B. Weems, S. C. Kienle, and A. M. Sims, "Three-dimensional acceleration measurement using videogrammetry tracking data," *Experimental Mechanics*, vol. 51, no. 2, pp. 199–217, 2011.

[Liu and Katz(2006)] X. Liu and J. Katz, "Instantaneous pressure and material acceleration measurements using a four-exposure piv system," *Experiments in Fluids*, vol. 41, no. 2, p. 227, 2006.

[Chu et al.(2018)Chu, Wolfe, and Wang] P. Chu, B. T. Wolfe, and Z. Wang, "Measurement of incandescent microparticle acceleration using stereoscopic imaging," *Review of Scientific Instruments*, vol. 89, no. 10, 2018. [Online]. Available: http://dx.doi.org/10.1063/1.5034311

[Chen et al.(2016)Chen, Li, Zhao, Huang, and Guo] G. Chen, L. Li, C. Zhao, R. Huang, and F. Guo, "Acceleration characteristics of a rock slide using the particle image velocimetry technique," *Journal of Sensors*, vol. 2016, 2016. [Online]. Available: http://dx.doi.org/10.1155/2016/2650871

[Dong et al.(2010)Dong, Song, Wang, Zeng, and Wu] J. Dong, Y. Song, H. Wang, J. Zeng, and Z. Wu, "Predicting flow velocity affected by seaweed resistance using svm regression," in

Computer Application and System Modeling (ICCASM), 2010 International Conference on, vol. 2. IEEE, 2010, pp. V2–273.

[Genç and Dağ(2016)] O. Genç and A. Dağ, "A machine learning-based approach to predict the velocity profiles in small streams," *Water resources management*, vol. 30, no. 1, pp. 43–61, 2016.

[Izquierdo-Verdiguier et al.(2014)Izquierdo-Verdiguier, Gomez-Chova, Bruzzone, and Camps-Valls] E. Izquierdo-Verdiguier, L. Gomez-Chova, L. Bruzzone, and G. Camps-Valls, "Semisupervised kernel feature extraction for remote sensing image analysis," *IEEE Transactions on Geoscience and Remote Sensing*, vol. 52, no. 9, pp. 5567–5578, Sep. 2014.

[Bouwmans et al.(2018)Bouwmans, Javed, Zhang, Lin, and Otazo] T. Bouwmans, S. Javed, H. Zhang, Z. Lin, and R. Otazo, "On the applications of robust pca in image and video processing," *Proceedings of the IEEE*, vol. 106, no. 8, pp. 1427–1457, Aug 2018.

[GmbH(2018)] P. S. GmbH, "Cobra4 sensor unit 3d acceleration," 2018. [Online]. Available: https://repository.curriculab.net/files/bedanl.pdf/12650.00/1265000e.pdf

[Komiya et al.(2011)Komiya, Kurihara, and Ando] K. Komiya, T. Kurihara, and S. Ando, "3D particle image velocimetry using correlation image sensor," in *Proc. SICE Annual Conf. 2011*, Sep. 2011, pp. 2774–2778.

[Šorel and Flu(2008)] M. Šorel and J. Flu, "Space-variant restoration of images degraded by camera motion blur," *Image Processing, IEEE Transactions on*, vol. 17, no. 2, pp. 105–116, 2008.

[Sengar and Mukhopadhyay(2017)] S. S. Sengar and S. Mukhopadhyay, "Detection of moving objects based on enhancement of optical flow," *Optik-International Journal for Light and Electron Optics*, vol. 145, pp. 130–141, 2017. [Online]. Available: https://doi.org/10.1016/j.ijleo.2017.07.040

[Klyuvak et al.(2018)Klyuvak, Kliuva, and Skrynkovskyy] A. Klyuvak, O. Kliuva, and R. Skrynkovskyy, "Partial motion blur removal," in *2018 IEEE Second International Conference on Data Stream Mining & Processing (DSMP)*. IEEE, 2018, pp. 483–487.

[Zhang et al.(2018)Zhang, Zhu, Sun, Wang, and Zhang] A. Zhang, Y. Zhu, J. Sun, M. Wang, and Y. Zhang, "Parametric model for image blur kernel estimation," in *2018 International Conference on Orange Technologies (ICOT)*. IEEE, 2018, pp. 1–5.

[Moreno et al.(2013)Moreno, Valcárcel, and Hurtado] R. J. Moreno, F. A. E. Valcárcel, and D. A. Hurtado, "Control de movimiento de un robot humanoide por medio de visión de máquina y réplica de movimientos humanos," *INGE CUC*, vol. 9, no. 2, pp. 44–51, 2013.

[Contreras Parada et al.(2014)Contreras Parada, Peña Cortés, and Riaño Jaimes] P. A. Contreras Parada, C. A. Peña Cortés, and C. I. Riaño Jaimes, "Módulo robótico para la clasificación de lulos (solanum quitoense) implementando visión artificial," 2014.

[Gallo Sánchez et al.(2016)Gallo Sánchez, Guerrero Ramírez, Vásquez Salcedo, and Alonso Castro] L. F. Gallo Sánchez, M. A. Guerrero Ramírez, J. D. Vásquez Salcedo, and M. Á. Alonso Castro, "Diseño de un prototipo electromecánico para la emulación de los movimientos de un brazo humano," 2016.

[Londoño et al.(2017)Londoño, Cortes, and Fernández] Y. Londoño, J. A. Cortes, and M. E. Fernández, "Diseño, construcción e implementación de sistema de adquisición y análisis de datos para la enseñanza del movimiento rectilíneo en el laboratoriodiseño, construccion e implementación de sistema de adquisición y análisis de datos para la enseñanza del movimiento rectilíneo en el laboratorio," *Momento*, no. 55, pp. 57–73, 2017.

[Slider(2017.)] R. M. Slider, 2017. [Online]. Available: https://www.revolvecamera.com/products/ram-motorized-dolly-slider-bundle.

[EVO.(2017)] R. R. S. EVO., "Learn the system, rhino," 2017. [Online]. Available: https://rhinocameragear.com/pages/new-to-rhino-learn-the-system

[Ding et al.(2010)Ding, McCloskey, and Yu] Y. Ding, S. McCloskey, and J. Yu, "Analysis of motion blur with a flutter shutter camera for non-linear motion," in *European Conference on Computer Vision*. Springer, 2010, pp. 15–30.

[Dwicahya et al.(2018b)Dwicahya, Ramadijanti, and Basuki] J. A. Dwicahya, N. Ramadijanti, and A. Basuki, "Moving object velocity detection based on motion blur on photos using gray level," in *2018 International Electronics Symposium on Knowledge Creation and Intelligent Computing (IES-KCIC)*. IEEE, 2018, pp. 192–198.

[Beggs(1983)] J. S. Beggs, *Kinematics*. CRC Press, 1983.

[Schmid et al.(2000)Schmid, Lazos, et al.] W. A. Schmid, R. Lazos *et al.*, "Guía para estimar la incertidumbre de la medición," *Centro nacional de Metrología (Abril 2004)*, 2000.

[Cortes-Osorio et al.(2020)Cortes-Osorio, Muñoz Acosta, and López Robayo] J. A. Cortes-Osorio, D. A. Muñoz Acosta, and C. D. López Robayo, "Diseño y construcción de un riel electromecánico para el estudio de la cinemática de imágenes con difuminación lineal uniforme," *INGE CUC*, vol. 16, no. 1, pp. 1–11, Jan. 2020.